Self-organization of silver nanoparticles with femtosecond laser in TiO2 matrix: Applications to plasmonic colours, multiple hidden images and Colour Image-Multiplexing

Nipun Sharma

To cite this version:

Nipun Sharma. Self-organization of silver nanoparticles with femtosecond laser in TiO2 matrix: Applications to plasmonic colours, multiple hidden images and Colour Image-Multiplexing. Optics / Photonic. Université de Lyon, 2020. English. NNT : 2020LYSES032 . tel-03117138v1

HAL Id: tel-03117138
https://hal.science/tel-03117138v1

Submitted on 21 Jan 2021 (v1), last revised 3 May 2021 (v2)

N° d'ordre NNT : 2020LYSES032

THESE de DOCTORAT DE L'UNIVERSITE DE LYON
opérée au sein de
Laboratoire Hubert Curien

Ecole Doctorale N° 488
Science Ingénierie Santé

Spécialité de doctorat : **Optique, Photonique**
Discipline : Matériaux pour l'optique

Soutenue publiquement 21/10/2020 par :
Nipun SHARMA

Self-organization of silver nanoparticles with femtosecond laser in TiO_2 matrix:

Applications to plasmonic colours, multiple hidden images and Colour Image-Multiplexing

---

Devant le jury composé de :

TREGUER-DELAPIERRE Mona	Professeur des Universités, Université de Bordeaux	Rapporteure
SOPPERA Olivier	Directeur de recherche CNRS, IS2M, Mulhouse	Rapporteur
GROSSO David	Professeur des Universités, Université Aix-Marseille	Président
SIEGEL Jan	Faculty Research Scientist, Instituto de Óptica, CSIC	Examinateur
OUERDANE Youcef	Professeur des Universités, Université Jean Monnet	Examinateur
DESTOUCHES Nathalie	Professeur des Universités, Université Jean Monnet	Directrice de thèse
VITRANT Guy	Directeur de recherche CNRS, Grenoble INP – Minatec	Co-directeur de thèse

ACKNOWLEDGEMENT

As I pen down the acknowledgement of my thesis, I would first and foremost thank my thesis supervisor Professor Nathalie Destouches, who accepted me in her Ph.D. Program at Laboratoire Hubert Curien (LabHC) five years back. She has been one of the amazing research supervisors I have worked under till now and her quest for research, makes you learn and exploit new things. I would also like to thank my co-supervisor Professor Guy Vitrant, who hired me for this thesis. Although, interactions with him were less during this time due to different field of research, his suggestions have always been useful.

Secondly, I would like to acknowledge ANR Region Auvergne Rhone-Alpes for funding the three years of my thesis from September 2015 up to September 2018. Further, the experiments, conferences related to this thesis for the three years were funded by LABEX MANUTECH-SISE (ANR-10-LABX-0075) of Université de Lyon, within the program Investissements d'Avenir (ANR-11-IDEX-0007). The prolongation of the thesis for four months were funded by HID Global CID, France from October 2018 up to January 2019.

Further, I would like to acknowledge Professor Youcef Ouerdane, for his immense support on this thesis at most of the times and ofcourse at coffee breaks. Then, I would also thank Professor Francis Vocanson who supported me in the chemistry part of the thesis.

Moving on, chronological order of the thesis chapters, I am thankful to Dr. Hongfeng Mark for his support on the theoretical coding in the chapter II, Dr. Thomas Bottein and Professor David Grosso for the ellipsometric measurements, followed by Dr. Matthieu Bugnet for all the TEM measurements performed in this thesis. Further thanks to Dr. Camilo Florian and Scientist Jan Siegel for an amazing collaborative work and laser processing at their Institute. Thanks to Dr.

Marie Vangheluwe for her support in the first half of my thesis and her collaborative work in the thesis related to laser processing in chapter IV.

Thanks to Stéphanie Reynaud, Yaya Lefkir, and Jean-Yves Michalon for their support in the characterization trainings and thesis related assistance. I would also like to thank all the researchers, engineers, technicians and support staff of the LabHC who helped me directly, indirectly through the period of the thesis.

A warm thanks to the group Nanoparticules, including Christophe, Zeming, Nicolas, Balint, for their support in the thesis and discussions in coffee and lunch breaks.

A big thank to HID Global CID and my manager Stéphane Ayala and ex-colleague Alice Vermeulin for hiring me before my thesis and having a belief that I can fit to the current role in the company while giving me space to complete the thesis parallel with the job.

At last, I would like to thank my parents, my wife Ambika and brother who supported me in tough times. This would not have been possible without you guys.

.

ABSTRACT

Self-organization of metallic nanoparticles in a medium is an efficient and a low-cost way to produce plasmonic systems that can be used for applications to active colour display, image encoding, and security. Such nanocomposite systems must be synthesized in form of stable films which could be coated on any kind of surface for laser processing. This doctoral thesis focuses on laser-induced self-organization of nanocomposite thin films of silver and mesoporous titania.

In this work, we first investigate synthesizing mesoporous TiO_2 thin films using hydrolytic process, which is easy to implement, to provide crystallized films starting at 100°C. First activation energies in mesoporous TiO_2 films using Raman spectroscopy in combination with the phonon quantum confinement model are reported in this work. Further, growth mechanisms of nanocrystals in mesoporous TiO_2 films are investigated in form of ellipsometric measurements highlighting its effect on film porosity and crystallinity with annealing temperature.

The second study demonstrates fabrication of different nanocomposite structures using femtosecond laser scanning technique, triggering growth and self-organization of silver nanoparticles inside porous amorphous titania matrix giving rise to plasmonic dichroic colours. Further investigation on the parametric study of such nanocomposites gives rise to different nanostructures at two different scan speed regimes, which are formed at the surface and are embedded below due to excitation of surface and the guided modes. The flexibility of this laser-based marking technology also allows to fabricate hybrid nanostructures composed of different adjacent nanostructure types, interlaced to cover large areas. An extension of this study is concluded on plastic/flexible substrates to encode diffractive printed images. Here surface nanostructures (LIPSS) are formed by using the control of laser polarization and thus grating orientation, which is used to encode grey-level images that can be observed in diffraction modes.

Further, this study is concluded by producing three image multiplexing which can be observed in three selected modes of observation under white light in reflection with non-polarized light and transmission between polarizers for two different polarization angles. This is due to the fact that the film birefringence and dichroism can be controlled to produce unprecedented colour gamuts for multiplexing. Such smart laser processing on nanocomposite thin films gives rise to artistic and security applications by encoding different images up to three under same area.

TABLE OF CONTENT

Chapter I: INTRODUCTION

Chapter II: MATERIAL SYNTHESIS

Chapter III: TAILORING NANOCOMPOSITES OF Ag:TiO$_2$ WITH FS LASERS

Chapter IV: DIFFRACTIVE MULTIPLE IMAGES HIDING USING FS LASERS ON NANOCOMPOSITE FILMS

Chapter V: IMAGE MULTIPLEXING

LIST OF SYMBOLS AND ACRONYMS

A	constant
a_0	lattice parameter
AcAc	acetyl acetone
AFM	atomic Fore Microscopy
Ag	silver
Ag:TiO_2	silver:titania nanocomposite
Al	aluminum
Au	gold
B_{1g}, E_g, A_{1g}	Raman band for crystal titania
BBO	barium borate
$\|C(0,q)\|^2$	phonon confinement function
CIE	Commission Internationale de l'éclairage
CLI	changeable laser image
CVD	chemical vapor deposition
cw	continuous-wave
D	crystallite size
d	laser beam diameter
D_0	crystallite size obtained at the lowest temperature
DI	deionized water
DSSCs	dye synthesized solar cell
dy	distance between two laser lines
$d^3q \propto q^2 dq$	three-dimensional confinement
E_a	activation energy
EBL	electron beam lithography
EELS	electron energy-loss spectroscopy
EEP	environmental ellipsometric porosimetry
EG	embedded grating
EtOH	ethanol
eV	electron volts

F	laser fluence
f or f_{rep}	repetition rate of laser
FFT	fast Fourier transform
FIB	focused ion beam
fs	femtosecond
HAADF	high angle annular dark field
HCl	hydrochloric acid
HNO_3	nitric acid
HRTEM	high resolution transmission electron microscopy
HS	high speed
HSt	hybrid structure
hv	photon energy
$I(\omega)$	Raman scattering intensity
$I(\alpha,\beta,\lambda)$	intensity transmitted under normal incidence through the dichroic sample placed between two polarizers whose axes are at α and α+β from x
IUPAC	International Union of Pure and Applied Chemistry
k	constant
kHz	kilo Hertz
kJ	kilo joules
k_{SPP}^{0}	SPP wave vector
LIPSS	laser induced periodic surface structures
LS	low speed
LSPR	localized surface plasmon resonance
M	molar
mJ	millijoules
mL	milliliter
MLI	multiple laser image
mW	milliwatt
n	grain growth exponent
η	refractive index
N_{eff}	number of effective pulse of laser
NH_3	ammonium hydroxide
η_{gm}	refractive index of the grating mode
nm	nanometer
ns	nanosecond

P	distance of the particles, periodically spaced
P123	poly(ethylene glycol)-block-poly(propylene glycol)-block-poly(ethylene glycol)
PET	polyethylene terephthalate
pH	potential of hydrogen
PMMA	poly(methyl methacrylate)
ps	picoseconds
PVD	physical vapor deposition
θ_{π}	angle formed at plane of incidence for which diffraction occurs
θ_i	incidence angle
$R^{'}$	molar gas constant
R	calculated reflectance
Re(η)	real part for the complex of the effective refractive index of the plasmon mode
Rh%	humidity percentage
Rpm	rotations per minute
SEM	scanning electron microscopy
SERS	surface enhanced Raman scattering
SG	surface grating
SPP	surface plasmon polariton
sRGB	standard Red Green Blue
T	calculated transmittance
τ	film thickness
T (K)	annealing temperature in Kelvins
TE	transverse electric
TEM	transmission electron microscopy
$TiCl_4$	titanium tetrachloride
TiO_2	titanium dioxide
TM	transverse magnetic
TTIP	titanium isopropoxide
$t_x\, e^{i\varphi_x(\lambda)}$ and $t_y\, e^{i\varphi_y(\lambda)}$	components of the complex transmittance of the film
UV	ultraviolet
v	laser scan speed
W	watt

x	integer
1-R-T	losses, including absorption and diffraction
Λ	grating period
Λ_{EG}	period of embedded grating
Λ_{SG}	period of surface grating
α'	absorption coefficient
α	sample rotation angle
$\alpha(\lambda)$	polarizability
λ	wavelength
λ_{Tmin}	wavelength at which transmission shows minimum
ϵ_{air}	dielectric function of air
ϵ_d	relative permittivity of the surrounding dielectric
ϵ_m	relative permittivity of the metal
ω_0	zone center phonon frequency
$\omega(\boldsymbol{q})$	dispersion relation of the phonon with the integral being performed over the entire Brillion zone
µm	micrometer
Γ_0	Raman linewidth at room temperature
δ	width of phonon dispersion curve
β_m	propagation constant
β	angle between two polarizers

LIST OF FIGURES

LIST OF TABLES

CHAPTER I
INTRODUCTION

Since many years now there has been quest for exploiting nanomaterials for different applications. The properties of nanomaterials such as high surface energy, higher fraction of surface atoms, reduce defects, vary from the bulk materials that make them unique.[1,2,3] One of the examples of such nanomaterials include mesoporous materials i.e. the class of nanomaterials having pores ranging from 2 to 50 nm. Such materials have lower density and high surface areas. Their properties are not just governed by the arrangement of the atoms within the crystal but also by the pore size and its surface area. Further, investigations for exploiting the pore size, phase, synthesis temperature and the structure has been carried out for applications to solar cells, sensors, membranes, optoelectronics and others, but still a need of exploring the world of such mesoporous nanostructures is present. Research of new mesostructured and mesoporous materials has become important over the last 25 years.[4,5,6]

Such mesoporous materials also act as host matrices to grow metallic nanoparticles within them. They are emerging as a new class of optical materials. These nanocomposite materials are characterized by the localized surface plasmon resonance (LSPR) phenomenon exhibiting absorption in the ultraviolet/visible region. LSPR is a collective oscillation of electrons in the conduction band of metallic nanoparticles, which is excited by the incoming electric field of the incident light. This behavior is directly related to the shape of the nanoparticles, their size, nature, inter-particle distance and the dielectric permittivity of the host environment.[7,8,9] Metallic nanoparticles have been used in for different applications, the oldest being used as a colourizing agent when dispersed inside a host matrix. A famous example of such response from the past, is the well-known Lycurgus Cup which exhibits dichroic colours due to the presence of gold (Au) and silver (Ag) nanoparticles.[10] Metallic nanoparticles exhibit colours due to light absorption and scattering in the visible region due to their plasmon resonances. Two of the most studied plasmonic metals for such behavior are Ag and Au as they exhibit the LSPR in the visible thus being used in many applications including colours, biosensors, surface enhanced Raman scattering (SERS) applications, and others.[11,12,13]

Metallic nanoparticles are important in fabricating nanocomposite materials with different optical properties when high intensity light is interacted with them. In the past, lasers have been used to alter the optical response of the nanocomposites either by tuning the individual characteristics of the nanoparticle or by producing nanoparticles gratings. While inducing the deformation of Ag in glass, Kaempfe et al. were able to produce permanent dichroic colour changes inside the glass.[14] Seifert et al. showed that Au/Ag nanoparticles in glass can be transformed to anisotropic shapes along the laser polarization direction to design optical properties of metal glass nanocomposites.[15] While for latter cases, where the optical response of nanocomposite materials can also be tuned both by varying features of the periodic structure and changing the morphology of the individual nanoparticle, Loeschner et al. showed femtosecond (fs) induced laser grating like structure and nanoparticle anisotropy inside polymer films giving rise to optical dichroism.[16] Other ways of altering the optical response of the composite systems can be using lasers to grow or self-organize nanoparticles inside dielectric titanium dioxide (TiO_2) thin films with embedded nanoparticles. A recent example of which was shown by our group 'Nanoparticules' using continuous-wave (cw) and fs laser on nanocomposites of Ag:TiO_2. Here while nucleation, growth and self-organization was observed using cw laser, a double self-organization was observed while using fs laser system giving rise to permanent dichroic colours.[17,18] Such laser induced nanocomposites can be used to encode colour pattern by taking advantage of its dichroic nature. This motivates us in studying the nanostructures that can be fabricated combining nanocomposite mesoporous thin films of Ag:TiO_2 and fs lasers and further explore the applications that these nanostructures can pave for applications towards encoding information. Further, structuring of metallic nanoparticles inside the crystallized and amorphous thin films of TiO_2 starting from low temperatures can potentially improve the photocatalytic performance of potentially fabricated laser induced nanocomposites on such films due to field trapping in the self-organized gratings.

The thesis completely revolves around mesoporous TiO_2 that is the principal matrix used in the thesis. In the first part, we explore the chemistry of mesoporous crystalized TiO_2 thin films while working at lower synthesis temperatures followed by studying light interaction of a fs laser system with nanoparticle composite films made of Ag:TiO_2 to control and self-organize nanoparticles within the oxidize films in the second part of the thesis. Further investigations show the practical applications of such nanostructures fabricated for multiple image hiding on plastic substrates and image multiplexing with fs laser systems.

1. Overview of TiO_2 Synthesis Methods and Applications

Since the commercial production of TiO_2 after 1920, it is one of the most exploited semiconductor. In 1972, Fujishima and Honda first discovered the photocatalytic splitting of water on electrodes of TiO_2 under ultraviolet (UV) light.[19] Since then enormous efforts have been put to research on TiO_2 material, leading to many practical applications including photovoltaics, photocatalysis, pigments, waveguides and sensors.[20,21,22,23,24] TiO_2 exists in three different polymorphs apart from its amorphous phase known as anatase, rutile and brookite where, the formation of the amorphous TiO_2 starts at room temperature until 350°C . All the three polymorphs are built from the TiO_6 octahedra where, the anatase structure is built from the edge sharing TiO_6 octahedra, and the other two polymorphs are built from both edge and corning sharing of the TiO_6 octahedra.[25,26] Moreover from various synthesis procedures of TiO_2 including sol-gel, physical vapor deposition (PVD), chemical vapor deposition (CVD) and hydrothermal, the transformation of amorphous to anatase phase usually occurs first at 350-400°C, due to ease of arrangement of short range TiO_6 octahedral into long range order anatase structure, this can be due to less constrained molecular construction of anatase as compared to rutile.[27] A pure anatase is considered to be transformed to the rutile phase at around 600°C in the air. Although, the transition temperature can vary up to 1200°C depending upon the type of synthesis precursors and route chosen.[27] Usually anatase and rutile are the two common polymorphs of TiO_2 and its third polymorph, i.e its brookite phase is usually obtained at around 500-600°C as a bi-product along with its other two polymorphs when synthesized under an ambient synthesis condition.[26]

The vast applications of amorphous and different polymorphs of TiO_2 being used as pigments in paints, cosmetics, polymers is due to their high refractive index in the visible range and its strong absorption in the ultraviolet range, especially in its anatase and rutile forms which also result in high reflectivity at its surface.[27] It has been studied that while the refractive index of amorphous TiO_2 is around 2.4, the refractive index values for the anatase varies from 2.5 ~ 2.6 and further rutile phase possesses a higher refractive index values of around 2.6 ~ 3 (wavelength (λ) corresponding to 546 -550 nm).[28,29] Further, due to its high dielectric constant, high transparency in the visible region TiO_2 has also been used in different optical applications. It has been used as micro ring resonators and waveguides.[30] Other works have showed that TiO_2 can be used as anti-reflector on infrared detectors, thanks to the low refractive index values of TiO_2 nanorods at wavelengths greater than 2 µm.[31] Further, the other applications of TiO_2 has been in the area of photocatalysis due to its deep valence band and the tendency of the photon-generated holes to locate at the surface of the material, thus making it as an oxidant agent. Also, the oxygen vacancy of TiO_2 and its n-type semiconductor behavior makes it good candidate for sensors including gas, optical, electric, and biosensor.[32] Thus, when the gases are absorbed on the surface of TiO_2 they lead to a change in its resistance. All these applications and the ease of fabrication of TiO_2 makes it an interesting material to investigate for further applications too.

1.1 Mesoporous TiO_2 and Thin Films: First Achievements

According to the definition of 'The International Union of Pure and Applied Chemistry' (IUPAC), porous solids are classified into three categories according to the diameter size of the pores: micropores (< 2 nm), mesopores (2-50 nm), and macropores (> 50 nm). Porous materials are of great interest due to their capacity of interacting with ions, molecules, atoms and nanoparticles not just on the surface but throughout the bulk of the porous material as a result of which the porous materials enhance their physical, and chemical properties and hence their potential applications. In early 90's scientists first reported a new family of mesoporous silicate denoted as M 41, before which such porous features were not recognizable due to lack of analysis techniques.[33] After this work, a quest of investigating new porous materials began, especially metal oxides, due to their tunable pore size, shape, volume, and composition. The first ever synthesis of hexagonal packed mesoporous TiO_2 was in print in the year 1995 by Antonelli et al. using sol-gel route.[34]. When compared to bulk TiO_2, the mesoporous TiO_2 is advantageous due to a higher surface area, and the possibility of diffusion of reactants over the surface, and further an increase in the density of the active sites hence making it interesting candidate over bulk TiO_2.[35] Such mesoporous materials are usually synthesized by two approaches, i.e. hard or soft templating routes (Figure I.1).[36] In hard templating synthesis routes the nanostructures are formed on the surface of the template. The templates are then removed via different physical and chemical methods thus generating pores. The other method used vastly, due to ease of fabrication is the soft templating route. It involves use of organic or polymeric surfactant which assembles into supermolecular structures, which involve co-assembly of the precursors (metal oxides, polymers, silica, etc). Such assemblies are then used as soft templates to tune pores.[37]

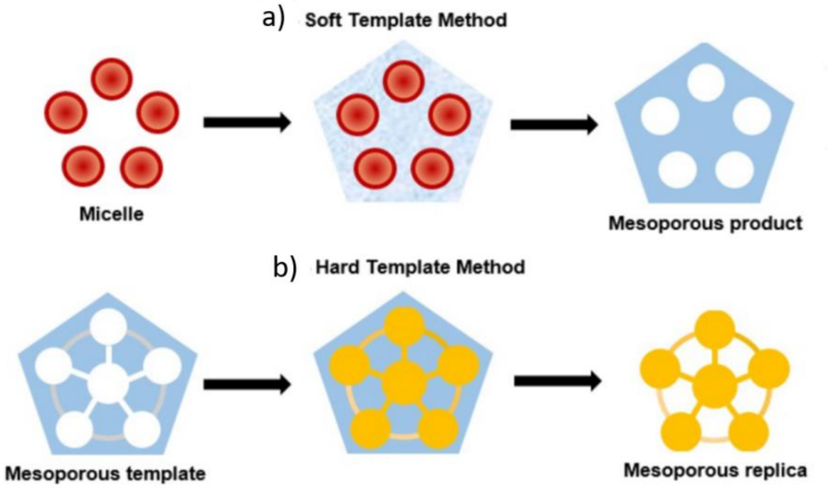

Figure I.1: Scheme representing the methods of a) Soft templating and b) hard templating to produce mesoporous films. (Image adapted from Machado et al.)[36]

Besides these templating methods, other methods can also produce mesoporous TiO_2, but with disordered structures. A perspective of synthesizing mesoporous TiO_2 thin films is by combining sol-gel along with soft templating technique or self-assembly process. A sol-gel is generated by two terms: sol, which consists of the liquid, and gel, which consists of a three dimensional network. The sol-gel process consists of an inorganic precursor or organic metal precursor along with an amphiphilic organic template. After this, the precursor and the organic template are mixed in a solvent in presence of an acid. The complete reactions take place under water. The final solution is then deposited with the help of different coating techniques such as spin-coating, dip-coating or slot die. The different coating techniques can offer different homogeneity and the choice for the coating technique generally depends upon the final application of the films. After the coating process, a thermal treatment is usually required to eliminate the organic template and release the porosity to obtain mesoporous TiO_2 thin films. In order to maximize the utility of such TiO_2 mesoporous materials, it is essential to synthesize them in form of thin films.

In 2001, three different research groups published back-to-back works on mesoporous TiO_2 thin films. Grosso et al. produced optical thin films of mesoporous TiO_2, synthesized using titanium tetrachloride ($TiCl_4$) as the inorganic precursor and F 127 and Brij 58 as the structuring template. The films were obtained at temperature of 350°C, with porosity ranging from 20 to 45%.[38] Further, Hwang at al. used a different four step synthesis process to obtain mesoporous TiO_2 films using nanoparticles of TiO_2.[39] Their four-step process comprises the synthesis of TiO_2 nanoparticles using $TiCl_4$ as a precursor and then blending these synthesized nanoparticles with template molecules of Brij di-block copolymer into the film followed by ageing and calcination process. The third published research in the same year used different synthesis precursors and templates. Yun et al. synthesized hexagonally packed TiO_2 mesoporous films under acidic conditions using titanium isopropoxide (TTIP) as the precursor and poly(ethylene glycol)-block-poly(propylene glycol)-block-poly(ethylene glycol), i.e. P123, as pore generating agent.[40] The mesoporous films were obtained after heating at 300°C. After this year, research on synthesizing mesoporous films began. Such mesoporous thin films of TiO_2 have proven their worth in the applicative research areas when compared to the bulk mesoporous TiO_2 as discussed above, due to instability of the nanopowders, and agglomeration over time for practical applications.

1.2 Coating Techniques for Thin Film Deposition

Two main types of coating techniques namely spin and dip coating techniques have been used in this thesis to deposit thin films of mesoporous TiO_2, before the post heat treatment as explained in the above section. Although such techniques are well-known a small introduction will give users a background of these two important techniques for thin film deposition. Spin coating requires a flat substrate (dimensions up to centimeter in length or diameter) for coating a solution. The substrate is stacked over the spinner with the help of vacuum and the coating solution is put homogenously over the substrate. The spinner is rotated at a specific angular speed, thus allowing the coating solution to spread homogeneously over the top surface due to centrifugal force acting due to the rotation (Figure I.2).[41] Generally the film thickness can be controlled by the speed of the spinner (in rotations per minute (rpm)), viscosity of the liquid used and the evaporation rate of the liquid which in turn depends upon the vapor pressure, local humidity, and temperature of the surrounding.[42] Generally, thickness of around 1 µm or less can be achieved with such coating technique.

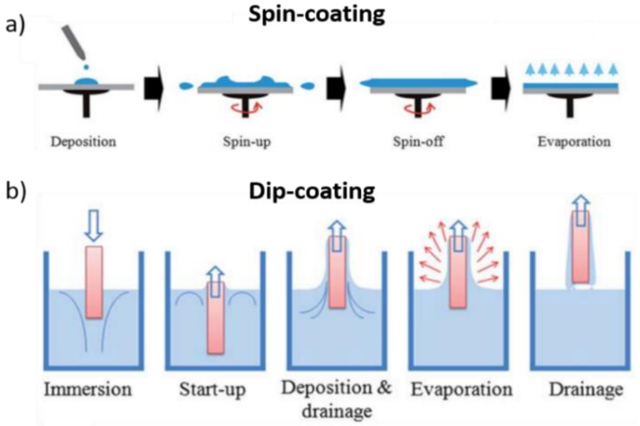

Figure I.2: Steps involved in a) Spin and b) Dip coating techniques, generally used to coat mesoporous thin films (Image adapted from Raut et al.)[41]

On the other hand, dip coating requires a flat and cylindrical substrate which is immersed in a coating solution vertically or with an angle and then is withdrawn upwards with a constant speed, thus resulting in thin film coating which is deposited on both sides of the substrate. The formation of the thin film occurs at the time of withdrawal where the substrate is retracted. It is when the evaporation of the coating solution takes place and part of the coating solution is stuck to the substrate. The thickness in this case is also dependent on the viscosity of the coating solution. The other factors which play a role on the film thickness are the withdrawal speed, fluid density and fluid surface tension as predicted by model proposed by Landau and Levich. Although, improvement in this model proposed by Faustini et al. showed that the film thickness also depends upon the evaporation rate of the sol used and the substrate width.[43] When comparing the two techniques, dip coating is developed for large-scale film production and has an advantage for incorporation to roll to roll processing and also for small batch experiments.

1.3 Applications to Mesoporous TiO_2 Thin Films

This section gives an overview and the advantages of the porous TiO_2 in different applications. TiO_2 thin films with larger surface areas, and controllable pore sizes have been studied for applications to solar-cells, photocatalysis, sensors, lithium ion batteries, waveguides and for micro inscription using lasers due to their stability over time.[44,45,46,47,48,49] A typical dye synthesized solar cell (DSSCs) contains a dye-adsorbed TiO_2 layer deposited on conductive oxide glass. A porous TiO_2 permits the dye specific concentration to be high for the absorption of the incident light and also provides accessibility to hole transporter, a thumb rule for efficient solar energy conversion in case of a typical DSSCs. Tuning the pore volume, Granados et al. synthesized mesoporous TiO_2 films with varying thickness and demonstrated that a combination of higher porosity and higher thickness gave the largest photocurrent density and hence the best photovoltaic performance when compared to the films with lower porosity and thicknesses.[50] Further, TiO_2 has been a great candidate for applications to photocatalysis. For a photocatalytic reaction, light with greater energy than the band gap of semiconductor should be absorbed on the surface of the semiconductor, thus creating electron-hole pairs, and simulating oxidation and reduction reactions. For this purpose, mesoporous TiO_2 becomes an interesting candidate, with higher surface areas. However, since TiO_2 alone shows a poor absorption in the visible range, efforts have been made to dope it with noble metals, non-metal anions and metal cations, thus enhancing absorption in the visible region and hence promoting the photocatalytic activity.[37] Further, such TiO_2 mesoporous thin films have also shown their worth as sensors due to higher surface areas, pore volumes and carrier diffusion length. When the TiO_2 mesoporous films are exposed to gases, the gas molecules are bound onto the surface of the pores, resulting in a chemical reaction and generating electrical signals.[51] Such mesoporous films also possess advantage over bulk TiO_2 acting as potential electrodes for lithium ion batteries, used in day-to-day life. The pores in the TiO_2 give a higher surface area to the material and a shorter diffusion pathway for electrons and lithium ions.[47] Further, one of the interesting properties of such mesoporous TiO_2 thin films in terms of this thesis is that, such films can also be used as reservoir for metallic ions, which results in high ionic mobility for such metallic ions. As the thesis, is principally based on nanocomposite of $Ag:TiO_2$, it is now important to give an overview of the optical phenomena happening around when laser are used with such nanocomposites.

2. Metallic Nanoparticles and Photochromic Behavior

Particles within the range of 1-100 nm, known as nanoparticles, show some fascinating properties. When an electromagnetic wave is trapped at a metal-dielectric interface on a metal surface, it is termed as surface plasmon polariton (SPP). Surface plasmons possess specific characteristic due to the oscillation of conduction electrons upon excitation of the incident light. Surface plasmon confined on the surface of metallic nanoparticles exhibit what is named LSPR as describe above. This collective oscillation of the free electrons (Figure I.3) causes a large resonant enhancement of the local field around the nanoparticle. This phenomenon, is widely used in SERS,[52] optical tweezers,[53] and optical devices.[54]

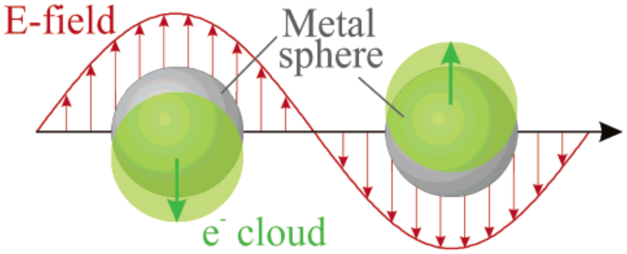

Figure I.3: A schematic diagram of electron charge displacement in the metallic nanoparticle interacting with an incident plane wave.

The resonance frequency of the oscillations as discussed in the introduction depends upon the dielectric properties of the metal, surrounding medium and other factors like the shape and size of the nanoparticles. Faraday showed that metal particles with different sizes and shapes exhibit different colours. Further in 1908, Mie theory suggested a general solution for single sphere interacting with electromagnetic radiation by solving the Maxwell equations.[55] The other important developments or models in this field included that of the effective medium theory and dipole approximations.[56,57]

2.1 Factors Influencing Localized Surface Plasmon Resonance (LSPR)

The surface plasmon resonance is not only influenced by the nature of the nanoparticle, but also by the environment of the host matrix. Once the effective polarizability of the free electrons is affected, the plasmon resonance is also affected. When the particle is smaller than the wavelength of light, the polarizability *α(λ)* can be simplified as:[7,58]

$$\alpha(\lambda) = 4\pi r^3 \frac{\varepsilon_m - \varepsilon_d}{\varepsilon_m + 2\varepsilon_d} \qquad \text{(Eq. I.1)}$$

where ε_m is the relative permittivity of the metal, ε_d is the relative permittivity of the surrounding dielectric. Further, it is known that the ε_m of the metal depends on the wavelength and the LSPR occurs when $\varepsilon_m = -2\varepsilon_d$. Thus the response of the plasmon is sensitive to the local environment, i.e. a change in the value of ε_d alters the value of ε_m for which resonance occurs ($\varepsilon_m = -2\varepsilon_d$). For bulk glass, the refractive index (η) is generally around 1.5 and hence the $\varepsilon_d = \eta^2 = 2.25$. As a result, in case of glass, the resonance condition is satisfied when, $\varepsilon_m = -2\varepsilon_d = -4.45$. For Ag nanoparticles, this occurs at 420 nm; whereas, for other noble metals like Au it occurs at 520 nm.[7] Other works from Rivera et al. also showed that the resonance frequency for Au and Ag nanoparticles differed when the η of host matrix was changed from η=1 to η=2. The shift in the LSPR corresponded to 78.5 nm for Ag nanoparticles, whereas a shift of 54.1 nm was observed for the Au nanoparticles for the two different host matrices.[59]

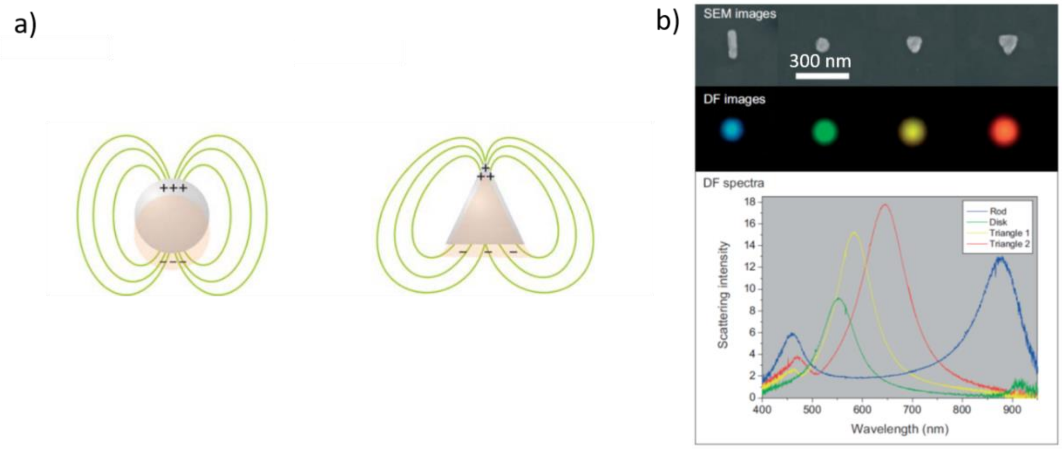

Figure I.4: Schematic diagram of LSPR of nanoparticles with two different shapes of a) sphere and triangle nanoparticles, with their corresponding charges distribution. Figure b) shows the LSPR shift, broadening and splitting for different nanoparticle shape. (Images adapted from Coronado et al.[60] and Murray et al.[7])

While the surrounding matrix is dominant for LSPR shift for smaller nanoparticles, for larger particles above 10 nm, the effects due to the amplitude and phase of the electromagnetic field around the particles become important thus resulting in size and shape dependency of the plasmon resonance. As the nanoparticle size is increased, there is an increase in the absorption and scattering, thus affecting the optical extinction of the nanoparticles. Further, the size-increase scattering dominates the absorption in the optical extinction thus shifting the plasmon resonance response.[7] Moreover, a change in the shape produces different surface charge (Figure I.4). While for the sphere or rods, the distribution of the surface charges is homogeneous, it becomes complex when the nanoparticle shape changes. An example of such particle is triangular nanoparticle where the charges are localized on one tip and one base of the prism. In such cases the resonances can be described in terms of hybridization between the plasmon modes of different structural components of the nanoparticles. While different shapes of the nanoparticles from rod, sphere to triangle fabricated using electron beam lithography (EBL) has showed a huge shift and splitting in the LSPR.[7,60] Further works from Mock et al. showed the effect of both the shape and size on the respective LSPR of the nanoparticles.[8] Here the authors investigated that they were able to shift the LSPR of the spherical silver nanoparticles from 400 nm, to 550 nm for pentagon silver nanoparticles and up to 700 nm for triangular silver nanoparticles. Such tuning of the LSPR with shape, size and medium as discussed firstly gives rise to various applications including near-field optical microscopy, nanosensors, and others.[61,62]

2.2 Photochromic Behavior

Photochromic behavior is defined as light induced reversible change of colour. The word photochromic is derived from Greek, where 'Phos' depicts the light and 'Chroma' means colour. In 1867, photochromism, first came into print when Fritzsche found that the colour of a tetracene solution from initial orange faded when kept in sunlight. Further, when the solution was again kept in dark it regained its orange colour.[63] This research expanded applications to photochromic glasses and photochromic micro-images where a book consisting of 1245 pages was reduced to 6 cm^2, but photodegrading of the organic photochromes limited the practical applications then.

As this work also deals with photochromic $Ag:TiO_2$ thin films in some parts, this section discusses the mechanism behind the photochromic behavior of the $Ag:TiO_2$ nanocomposites, giving users a background. It is known that when a metallic nanoparticle integrated with a host semiconductor is photo-excited due to plasmon resonance, then charge separation occurs by the transfer of the photo-excited electrons from the metallic nanoparticle to the conduction band of the semiconductor, passing through the Schottky junction formed at the metal/semiconductor interface (Figure I.5a).[64,65]

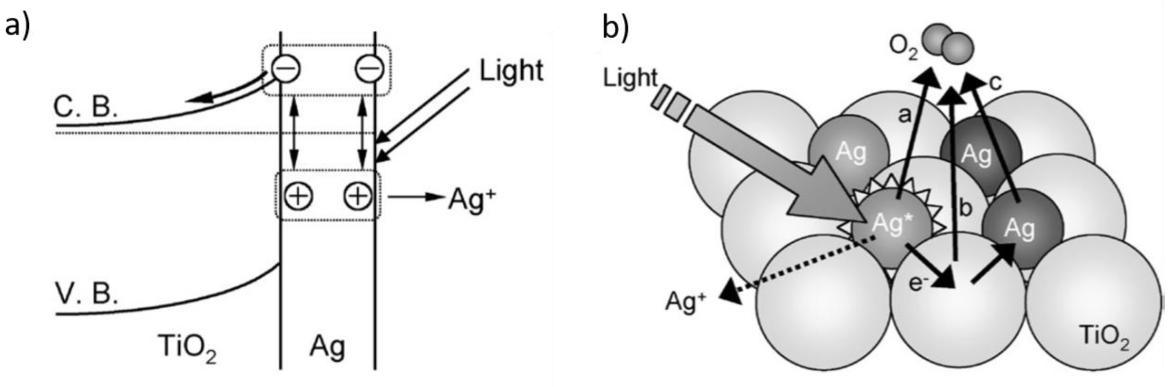

Figure I.5: a) Mechanism proposed by Kawahara et al. for a) charge separation at Ag:TiO_2 interface and b) electron pathway from excited silver nanoparticle to the oxygen molecule (Images adapted from Kawahara et al.[65]).

In case of Ag:TiO_2 nanocomposites, under UV light irradiation the Ag ions are converted into Ag nanoparticles, due to the photocatalytic activity of the TiO_2 matrix; the Ag nanoparticle grows due to the LSPR of the nanoparticle. The film at this point is brownish in colour. Now if the same film is irradiated by a monochromatic white light, the excited electrons at the silver surface absorb the white light, thus the electrons which are excited are transferred to the oxygen and hence the Ag nanoparticle oxidizes to Ag ions. Now due to the oxidation, only light of incoming wavelength is reflected or transmitted, and the rest is absorbed by the remaining particles thus showing the colour on the nanocomposite films of the respective excited wavelength.[66] Further, the UV light reduces the Ag ions to nanoparticles, due to the photocatalytic activity of TiO_2.

Such Ag nanocomposites can be synthesized using different protocols inside and with TiO_2 porous or nonporous matrix in its different phase of amorphous, anatase and rutile. Ohko et al. investigated reduction of Ag ions into Ag nanoparticles using UV light irradiation inside TiO_2 anatase films synthesized using sintering techniques.[67]. Such nanocomposites of Ag:TiO_2 were also prepared by Crespo-Monteiro et al. where the authors synthesized amorphous TiO_2 matrix using sol-gel and then reduction of Ag ions into nanoparticles inside such matrix was performed using a continuous UV laser.[68] Although, such growth of nanoparticles inside the pores is reduced when using lasers. The authors overcame this issue by thermally growing silver nanoparticles in such TiO_2 amorphous mesoporous matrix using heating of TiO_2 matrix with Ag ions at 200°C in air.[49] Further, Bois et al. also showed how Ag nanoparticles can be grown in TiO_2 mesoporous template using ammonical silver solution and its chemical reduction using ammonium hydroxide (NH_3), followed by a thermal treatment at 100°C.[69]

Due to photochromic behavior of Ag:TiO_2 nanocomposite films, the nanocomposites are unstable over time and may change the nanoparticle content (size, density) inside the film over time or in other words the colour stability for the films. To have reproducible results on such films, it is vital to make such films stable over time. Our group showed the stability of such films by demonstrating the repeatable ability of photochromic behavior of such nanocomposites coated on glass by exposing them to laser induced reduction (244 nm) followed by laser induced oxidation (488 nm), six times. The bleached films, regain their brown colour under UV exposure and absorption was similarly restored to its original value even after six cycles of UV-visible depicting colour stability of the films under ambient light.[70] Further, Fanny et al. showed the photochromic stability of the Ag:TiO_2 nanocomposites coated on plastic substrates using UV-visible light exposure. The photochromic properties were showed to be in good contrast for coloured and colourless state for five different cycles, demonstrating a good reproducibility.[71]

3. Self-Organization Using Continuous (cw) and Femtosecond (fs) Lasers on Nanocomposites of Ag:TiO_2

The change in behavior of the nanoparticles dispersed in a host matrix after laser exposure is known since few years now. The nanoparticles after laser irradiation can grow, oxidize or self-organize themselves inside a host matrix. Such fundamentals become vital to understand before discussing the experimental results and applications discussed in this thesis work. This section will mainly revolve around the work carried out by our group in recent years.

3.1 Continuous (cw) Laser

The first self-organized arrays of nanoparticles with a cw laser was reported in the year 2014 by our group.[72] Here, a thin mesoporous film of TiO_2 acting as a waveguide of around 200 nm was produced via a sol-gel chemistry on a glass substrate. The film acts as a waveguide, and high refractive index of TiO_2 becomes essential in such laser processes. The initial films are impregnated with Ag ions, which are converted to small Ag nanoparticles, thanks to the photocatalytic activity of TiO_2. Thus, the initial Ag:TiO_2 films contain Ag ions, atoms and nanoparticles as suggested by Liu et al.[73] For the growth of Ag nanoparticles using cw laser, high atomic and ionic mobility must be reached, which is favored by the low density of the mesoporous films. The laser driven growth of nanoparticles is a two-step process where silver ions are firstly reduced to silver atoms by reduction reaction, and growth mechanisms that increase the size of the nanoparticles either by adsorption of Ag atoms to nanoparticles according to Ostwald ripening or by coalescence of nanoparticles, the whole being controlled by plasmon induced temperature rise.[74] Oxidation occurs whatever the laser intensity, while the nanoparticle growth becomes significant above a certain threshold temperature (Figure I.6).[75] Above an intensity threshold leading to temperature rise, for certain laser parameters including power, speed, and wavelength, the laser writing gives rise to buried self-organized arrays of Ag nanoparticles where the embedded grating are always parallel to the laser polarization.[76]

The optical origin of self-organization arises from the fact that a part of the field scattered by the nanoparticles is trapped inside the waveguide. The particles which are periodically spaced by a distance $P = \frac{2\pi}{\beta_m}$, where β_m is the propagation constant of the guided mode, can then excite the guided mode.[72] These guided waves thus interfere with the incident beam, giving rise to an intensity modulation and further nanoparticle evolution. Thus, embedded self-organization with a cw laser occurs with grating lines parallel to the incident laser polarization.

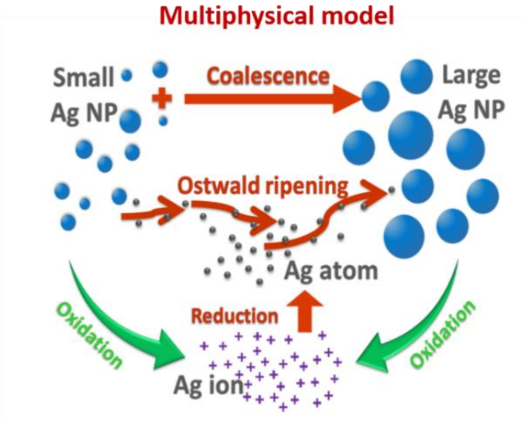

Figure I.6: Physio-chemical mechanisms leading to the growth or the shrinkage of Ag nanoparticles with a cw laser system. (Image adapted from Liu et al.)[75]

Further studies by Baraldi et al. with cw lasers showed a polarization driven 1-D and 2-D self-organization.[76] Here, a 2-D organization was obtained via two different methods. The first method involves a two consecutive laser writing process with cross polarizations. As discussed above, the porous structures play an important role; the author takes care that the porosity is not destroyed completely after the first laser writing. The porous structure provides the ionic and atomic mobility for the growth of the nanoparticles for the second consecutive laser writing along with that, the presence of the adsorbed oxygen in this scenario is responsible for oxidation to occur. While the second approach uses a single scan illumination consisting of a circularly polarized light thus giving rise to a 2-D hexagonal structure.

With the self-organization of silver nanoparticles with the cw laser system being discussed now, it is important to give an introduction to the nanoparticle growth and self-organization processes using femtosecond (fs) laser systems, recently developed within the team.

3.2 Femtosecond (fs) Laser

Unlike a cw laser system, a pulsed laser system confines the optical energy into a short span of time (10^{-15} seconds) and leads to a very short interaction of light with matter and transient response of the atoms and molecules.[77] It is also known that the pulsed laser generates less temperature rise than cw lasers. Theoretically, Baffou et al. showed that for nanoparticles of specific size ‘r’, the thermal response with the cw laser systems is much higher than with the pulsed laser system.[78] In the context of this thesis, a high temperature rise with the cw laser systems is considered as a drawback for industrial applications where substrates like plastic and paper are used. The latter actually have a low temperature resistance. To explore the performances of pulsed laser for generating self-organized gratings of nanoparticles, our group collaborated with the laser processing group at Instituto de Optica-CSIC in Madrid, Spain. The work led to 3-D self-organization of Ag nanoparticles with fs laser irradiations on nanocomposites of Ag:TiO_2.[18]

Liu et al. especially demonstrated that two independent self-organization processes can occur, giving rise to a 3-D nanostructuring with a fs laser while exciting a surface wave and a guided wave propagating in perpendicular directions. For a constant laser fluence, and for two different scan speeds two different structures named LS (low speed) and HS (high speed) as shown in Figure I.8 were obtained. Whereas laser induced periodic surface structures (LIPSS) with a period close to 500 nm (laser wavelength) were obtained for HS structure whose orientation was perpendicular to the laser polarization, an embedded periodic nanostructure was obtained for LS structure, where a period of around 300 nm was measured with lines parallel to the laser polarization.

To understand the growth mechanisms of Ag nanoparticles in this case when high fluence (fs laser in this case) is absorbed by the nanoparticles, the following steps must be considered: excited electrons are generated due to the LSPR of the initial Ag nanoparticles inside the nanocomposite. Then in short span of time the electron-electron scattering gives rise to hot electrons. Those hot electrons whose kinetic energy is greater than that of the Schottky Barrier formed at the Ag:TiO_2 (metal:semiconductor) interface are injected into the TiO_2 conduction band (Figure I.7). Due to the strong density of small metallic nanoparticles in the initial state, a large amount of free electrons can populate the TiO_2 and activate a transient metallic-like behavior of the nanocomposite film which is required for the excitation of a surface plasmon polariton (SPP). Meanwhile the electrons which were not able to cross the Schottky Barrier relaxes through electron phonon coupling thus transferring their energies to the nanoparticle lattice. Thus an equilibrium of electron and lattice temperatures gives rise to a temperature rise in the nanoparticle. After typically 100 picoseconds (ps), the heat can be transferred to the surrounding matrix through thermal conduction. A higher temperature rise in the matrix enables the growth mechanisms, thus leading to larger Ag nanoparticles pulse after pulse.[18]

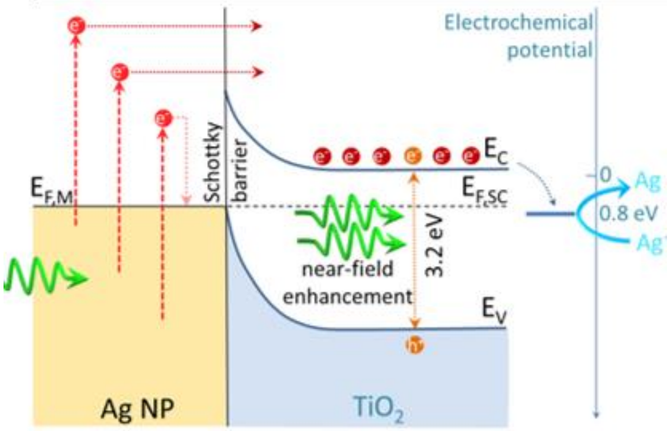

Figure I.7: a) Energetic diagram of the silver metal and semiconductor interface, in this case Ag:TiO_2 (Image adapted from Liu et al.)[18]

From an optical point of view, the transient metal-like behavior of the film surface upon fs laser exposure enables the excitation of a SPP on the film surface. The SPP propagates mainly along the laser polarization and creates an interference pattern with the incident light whose orientation is perpendicular to the laser polarization and whose period is $\frac{\lambda}{Re(\eta)}$, λ being the laser wavelength and *Re*(η) is the real part for the complex of the effective refractive index of the plasmon mode. *Re*(η) is close to 1 as the matrix has a metal-like behavior, which leads to a grating period value around 500 nm thanks to the positive feedback mechanisms that arises pulse after pulse when the progressive appearance of an index grating in the film enhances the excitation of the plasmon mode that creates the grating itself.

Furthermore, while the number of laser pulses is increased, temperature increases within the film promoting the growth of nanoparticles in the film. Higher electromagnetic scattering inside the film can now lead to the excitation of a guided mode in the film, which acts as a waveguide.

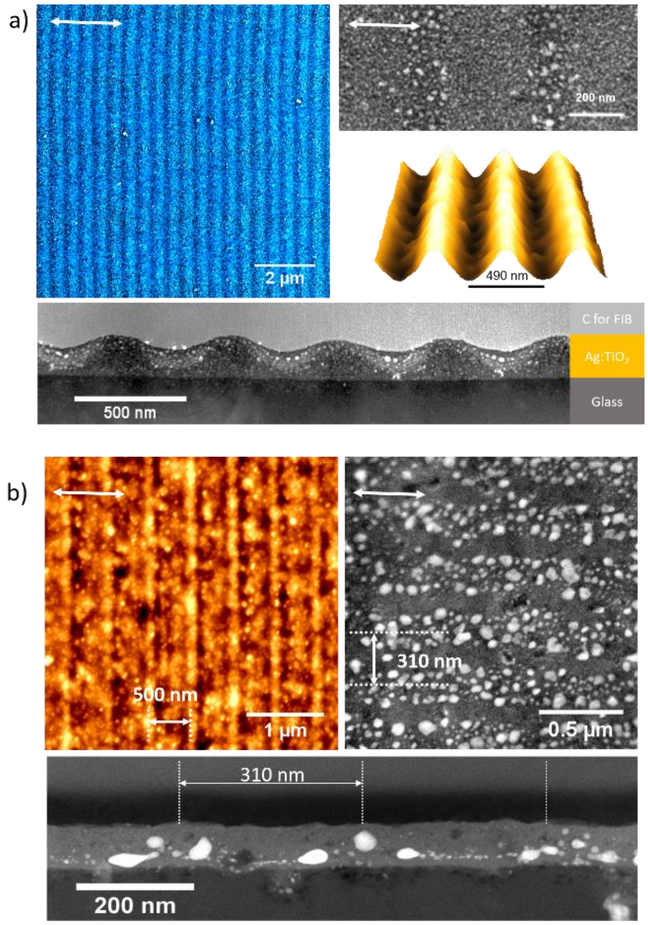

Figure I.8: a) SEM micrograph showing a self-organized periodic surface grating when the surface wave is excited while using high speed of 100mm/s with fs laser. The corresponding images showing the AFM topography for the same followed by HAADF-STEM micrographs from the top view (top right side) and on the cross section for the HS structure. b) LS nanostructures produced while using 10 mm/s laser scan speed. AFM surface topography and HAADF-STEM top view and cross-section. The white double sided arrow in the top corner of each images, depicts the laser polarization.(Image adapted from Liu et al.)[18]

As previously, an interference pattern can fall into place with the incident wave and a positive feedback can enhance the excitation of the guided mode provided that the wave now propagates in the direction perpendicular to the laser polarization. The growth of larger nanoparticles therefore leads to the formation of a self-organized grating whose orientation is parallel to the laser polarization (as for cw laser-induced self-organized gratings[72]) and period, still given by $\frac{\lambda}{\eta_{gm}}$, with η_{gm} the effective refractive index of the guided mode now, is close to 300 nm. The embedded grating is only obtained at lower scan speeds and high repetition rate that favor thermal accumulation, a condition to grow silver nanoparticles. The location of the nanostructures are obtained at different depths in the TiO_2 matrix for both the HS and LS structures as seen in Figure I.8 a-b.

After discussing cw and fs laser mechanism on the nanocomposite films of Ag:TiO_2, the last section for this chapter illustrates the motivation and the organization of the thesis and defines different collaborators who were involved in this thesis work.

4. Motivation and Organization of the Thesis

The thesis is divided into five chapters, including this first chapter of the Introduction giving an overview of the background and the motivation behind the work. Further, at Laboratoire Hubert Curien (LabHC), the group 'Nanoparticles' has developed experience in developing amorphous mesoporous TiO_2 and silica films in the past on glass substrates. Such films of TiO_2 are important if the porosity and crystallinity can be finely tuned at will. Further studying the crystalline growth in such mesoporous films followed by investigating the role of crystal seeds, and pores on the activation energy of crystal growth is motivated by the works of Kohn et al.[79] and Zhang et al.[80], where the authors investigated crystal growth in mesoporous networks of TiO_2, and compared with samples that are purely amorphous, nanocrystalline and a mix of amorphous and nanocrystalline. This work is illustrated in Chapter II, which focuses upon synthesizing crystallized optical mesoporous TiO_2 thin films starting at low temperature. A process is developed, to initiate nucleation of TiO_2 below the boiling point of ethanol using acid-assisted sol-gel process. Further, the role of crystal seeds on the films crystallization is investigated via Raman spectrometry and interpreted in the framework of a phonon quantum confinement model. The modelling in this chapter was performed by Hongfeng Ma, a Ph.D. student at Laboratoire Hubert Curien, supervised by Tatiana Itina. The isothermal crystal growth is investigated to estimate its activation energy as a function of the presence of crystal seeds and is characterized by optical microscopy and ellipsometry. All the transmission electron microscopy (TEM) characterizations of this thesis were performed by Dr. Matthieu Bugnet, CNRS researcher at Laboratoire MATEIS in Lyon, France, at Consortium Lyon Saint-Etienne de Microscopie (CLYM), Lyon. The Ellipsometry measurements depict the changes in porosity and the evolution of the film refractive index arising due to chemical changes in the sol with the temperature. The ellipsometric and ellipsoporosimetry characterizations were performed by Dr. Thomas Bottein, formerly Ph.D. student of Professor David Grosso, at IMP2NP, Aix-Marseille University, France.

Further as discussed above, the group has been successful in investigating several growth processes of silver nanoparticles inside TiO_2 matrix using UV assisted and chemical reduction processes. As the nanocomposite films of $Ag:TiO_2$ (amorphous TiO_2) are photochromic in nature, which means that they change their colour when exposed to visible light, a defined protocol was adopted to ensure the reproducibility of the films before laser processing. This is what the second part of Chapter II deals with.

Chapter three is motivated by the work on 3D self-organization processes performed by the Dr. Zeming Liu, former PhD student of the group[18] and extends the study to a larger parameter range. All laser irradiations of this chapter were performed in Madrid by Post-doctorant Dr. Camilo Florian and Research Scientist Jan Siegel at Laser Processing Group of Instituto de Optica, of Consejo Superior de Investigaciones Científicas (CSIC), Spain. We provided the samples and performed all the characterizations on the processed films. The work focuses upon nanoparticle growth and self-organization processes that are controlled by a careful adjustment of laser irradiation parameters between the ranges of two self-organization regimes obtained before, giving rise to different structures with tuneable particle size, shape and arrangement. The wide range of produced structures obtained between the two regimes, offers unparalleled control over the optical response of the system, including spectral control in reflection and transmission, as well as diffraction configurations and dichroic plasmonic colours.

The fourth and the fifth chapters investigate the potential applications of fs laser processing on flexible plastic and glass substrates for applications to multiple image hiding and image multiplexing as a consequence of laser induced self-organization processes and shape anisotropy of metallic nanoparticles for producing dichroic colours in reflection, and transmission. While, the above processes with lasers were always investigated on the nanocomposite films deposited on glass substrates, there was a need to investigate the probability of expanding such self-organization processes leading to colours and diffraction gratings on flexible substrates including plastics. Due to the very poor thermal inertness of plastic flexible substrates, the group developed new protocols for the synthesis of photochromic Ag:TiO_2 films deposited on polyethylene terephthalate (PET) substrates[71,81] and the production of micro-patterns using cw laser printing on such substrates.[82] The film elaboration process was used for coating polycarbonate (PC) sheets and fs laser printing was implemented to limit thermal effects and lead to the formation of LIPSS on Ag:TiO_2 films deposited on PC. A part of this work, deals with printing multiple images on such flexible plastic substrate. The laser processes of this chapter were carried out by Dr. Marie Vangheluwe, a post-doc at Laboratoire Hubert Curien who also developed the fs laser experimental setup at LabHC. The work further enlightens the issue of laser-induced thermal effects that are serious limitations for plastics processing and provides conditions optimizing the nanoparticle growth and self-organization in the nanocomposite film while preventing the film spallation and the substrate damage. The work then deals with an innovative technology of printing multiple hidden diffractive images on plastic substrate that can be revealed to the eye under specific observation conditions only. The present work demonstrates a simple and facile technology for industrialization.

Hiding several images on the same area, which are recognizable under different angles of observation have become useful for applications concerning security, optical storage and identification. The last part was of this work in chapter fifth was motivated by the development of a laser printing technology for HID global CID, France which allows to demonstrate the principle of three image multiplexing of images with fs laser technology on Ag:TiO_2 nanocomposite thin films on flexible glass substrates.

All the characterization techniques, experimental setup used in the context of the thesis have been acknowledged; unless specified, the characterization techniques or experiments were performed at LabHC.

The thesis is concluded in chapter sixth, where a complete conclusion of the thesis is presented along with the perspectives of the work, which can be carried out in future.

.

CHAPTER II

MATERIAL SYNTHESIS

1. Introduction

As discussed in the previous chapter, TiO_2 is a widely used material for applications to waveguide,[72] photocatalysis,[83] pollution control,[83] colour marking,[17] photovoltaics,[84] self-cleaning windows,[85] and sensors,[24] owing to its specific optical and electronic properties like high refractive index[30] and high band gap[86]. In recent years, synthesizing crystallized TiO_2 starting at low temperatures has been of great importance for several of these applications, however most of the synthesis processes are long, tedious and lead to crystallized TiO_2 in powder form, which is not convenient for optical applications.[87,88.89] Synthesizing films at low temperature, whose porosity is controlled in the nanometer range to reach high specific surfaces, whose thickness and refractive index are tunable and for which the crystallinity affords good charge transport properties may widen the use of TiO_2 as a functional coating on many kinds of surfaces, including plastic surfaces that do not withstand high temperatures.

While most of the reported studies consider non-hydrolytic chemistry approaches, only few discuss about hydrolytic chemistry. Hydrolytic methods provide foremost reaction and heat control for synthesizing a material as compared to the non-hydrolytic methods which requires a long reaction duration to reach a thermodynamically stable state.[90] Until now, different hydrolytic and non-hydrolytic sol-gel routes were proposed to synthesize TiO_2 nanocrystals at room temperature, however with more than a week long ageing time of the sol. When considering hydrolytic chemistry, Qi et al.[89] synthesized anatase TiO_2 powders at low temperatures in a week for applications to self-cleaning properties. Gopal et al.[91] synthesized crystalized TiO_2 precipitates in the sol at low temperatures in a time close to what will be discussed in this chapter, however such precipitates cannot be used to form optical thin films. Using non-hydrolytic processes, Zhang et al. synthesized TiO_2 dry-gel films with an ageing time of two weeks followed by an UV assisted fabrication process.[92] Few of the published works discuss about obtaining crystallized TiO_2 films at low temperature by introducing commercial anatase TiO_2 nanoparticles in their synthesis process.[46] While such processes are not cost-effective, there is a risk of forming agglomeration when using sol-gel synthesis or wet-chemical processes with an external physical parameter like pH.

Kohn et al. investigated the role of as-synthesized crystalline seeds in lowering the crystallization temperature for non-mesoporous and mesoporous TiO_2 network with a synthesis process combining both hydrolytic and non-hydrolytic chemistries.[79] They further investigated the role of crystal seeds on the activation energies of crystalized non-mesoporous films. A non-hydrolytic process was used by Angelomé et al. to get nanocrystals in mesoporous TiO_2 films from 100°C after 24 hours heat treatment under humidity for application to photocatalysis.[93] Compared to the aggregate crystalized TiO_2, a mesoporous network eases atomic diffusion in pores and acts as a reservoir that can be filled with an electrolyte forming a heterojunction with large contact areas in some applications[20] or with metallic ions to create nanostructured multi-colour plasmonic films by laser in others, which is important for the next part of the thesis.[18] It thus becomes vital to investigate and understand the crystal evolution of mesoporous optical films with tunable porosity and crystallinity with annealing temperature.

In this chapter, the conditions to obtain mesoporous crystallized films via rapid and facile hydrolytic sol-gel route, were optimized with significant modifications in our previously published synthesis process to initiate the nucleation of TiO_2 nanocrystals near the boiling point of ethanol.[94] The effect of crystal seeds in as-deposited films on the phase transitions of TiO_2 at increasing temperature is then investigated using Raman spectroscopy interpreted in the framework of a phonon quantum confinement model, scanning electron microscopy (SEM) and transmission electron microscopy (TEM). The isothermal crystal growth is investigated in a temperature range between 100°C and 1000°C to estimate its activation energy as a function of the presence of crystal seeds in the as-deposited films. Ellipsometry manifests how chemical changes in the sol affect the porosity and the evolution of the film refractive index for increasing annealing temperatures. Absorption spectra are measured to determine the band gap of all these TiO_2 films.

2. Experimental Details

2.1 Materials

TiO_2 sol was prepared after doing some modifications in the synthesis process of amorphous mesoporous TiO_2 described in one of our previously published article.[95] This amorphous sol will be defined as normal sol for this chapter as a reference. The new sol discussed here, involves chemicals such as titanium-tetraisopropoxide (TTIP-97%), Acetylacetone (AcAc-99%), nitric acid (HNO_3), poly(ethylene oxide) – poly(propylene oxide) – poly(ethylene oxide) block copolymer (pluronic P123, molecular weight: 5000), all purchased from Sigma Aldrich and ethanol (absolute EtOH) from Carlo Erba. The chemical reactions were carried out using deionized water (DI) in all the cases where material synthesis is involved in the thesis. Whereas, all the chemical synthesis and coating processes were performed in a clean-room (class 100 and class 1000; Rh%= 45±5 % and Temperature= 20°C±2 °C) to maintain the reproducibility in the synthesis process and prevent any impurities in the system. Although, the coating methods may vary with chapter of the thesis (dip or spin-coating).

2.2 Initial Sol

The chemicals were used in a defined molar ratios fixed at: TTIP:P123:EtOH:HNO_3:DI:AcAc :: 1:0.025:28.5:0.015:29.97:0.5. In flask one, TTIP (5g) was mixed with AcAc (0.88g) under a constant stirring for 15 minutes. In a second flask, P123 (2.55g) was dissolved in EtOH (23.08g) under a stirring for 15 minutes, before adding two drops of HNO_3. The mixture is allowed to stir for 30 minutes. Then, at room temperature the content of flask one was added dropwise to flask two with a constant stirring at 350 rpm followed by an addition of DI (9.5g) to the mixture, the pH of the final mixture being 4.5. The solution was stirred for the next 2 hours. The sol synthesized at this step was transparent yellow in colour. It's to be noted that, the only difference between the 'normal sol' and the sol mentioned in our previous works, is the used of acid in the process. While, hydrochloric acid (HCl) was used in the normal sol as mentioned in our previous work, HNO_3 is used in the present synthesis process. The only reason for the change is the inert nature of flexible substrates (PETs, polycarbonates, plastic) towards HNO_3 when compared to HCl, for applications to low temperature uses. When a high amount of HCl is added, the flexible substrates (polycarbonates, plastic) initiate a surface damage which is not the case while using HNO_3. As the synthesis process in this study involves a lower pH, HCl is replaced with HNO_3.

2.3 Modifications in the Sol

The as-prepared sol was divided into four vials and pH of three vials were adjusted to 3, 2 and 1 with HNO_3 acid along with the original synthesized sol having a pH of 4.5. For studying the effect of the synthesis temperature on the crystal seed formation, these sols were stirred at 50, 60, 70 or 75°C for 4 hours. The reactional temperature was restrained to 75°C that is near the boiling point of EtOH, a solvent used in our synthesis process. Above this temperature the solution will turn into a gel.

2.4 TiO_2 Films

Block copolymer-templated mesostructured titanium dioxide films were obtained by dip-coating the different sols on silica (NEGS2 from Neyco) substrates at a rate of 7 cm/min. Before dip-coating, the TiO_2 sol was filtered using a 0.2 µm syringe filter. Just after titania deposition, films were baked at 100°C for 30 minutes in a pre-heated oven. Prior to any experiment, the substrates were cleaned with a defined protocol of sonication in EtOH, acetone and DI for 15 minutes each under a sonication bench, followed by drying the slides with nitrogen. To investigate the influence of the presence of crystal seeds in the initial sol on phase changes and activation energy of the crystal growth, films deposited on silica were independently calcined for

30 minutes at temperatures from 100°C to 1000°C with a step of 100°C. To get mesoporous titania films below the degrading temperature of P123, the mesoporosity can be released by chemical extraction or infrared annealing, as described in details in one of our previous papers and also in Chapter IV.[71] However, such further treatments were not used in the present chapter to investigate only the effect of annealing temperature on the crystallization process and haven't been discussed here in the chapter.

3. Results and Discussion

3.1 Influence of pH and Synthesis Temperature on the Generation of Crystal Seeds

Raman spectroscopy have been used as a basic tool to study the phase of TiO_2 for this study. A LabRAM ARAMIS-Horiba Raman confocal spectrometer was used with an excitation laser wavelength of 633 nm to measure all Raman spectra. At this raman laser wavelength, not only the titania and the substrate are transparent but the laser power on the sample was decreased to 7 mW to minimize the potential heating. This allows us to eliminate Raman response due to the local laser-induced temperature rise even on the samples synthesized at lower annealing temperatures. Under such conditions, measurements were fully reproducible on all samples. Raman spectroscopy is a non-destructive powerful tool to characterize the vibrational and rotational frequencies of specimens and serves as a tool for the material identification that absorbs laser photons.[96] It can accurately depict the crystallized phase of any material. Bulk anatase TiO_2 consists of three E_g bands at 144, 197 and 633 cm^{-1} and B_{1g} and A_{1g} bands at 409 and 515 cm^{-1} respectively, whereas four bands exist for the rutile phase consisting of B_{1g}, E_g, A_{1g} bands at 143, 447, 612 cm^{-1} respectively, and a band at 235 cm^{-1} corresponding to a combination of modes.[97,98,99,100] Such bands get broader and are shifted when the crystal size decreases due to the phonon confinement effect.[100] Studying the germination of anatase nanocrystals for the films annealed at only 100°C, we mainly focus on the emergence of the strongest E_g anatase band coming from external vibrations of the structure. In this study, this band starts developing at around 155 cm^{-1} rather than at 144 cm^{-1} owing to the small size of crystal seeds.

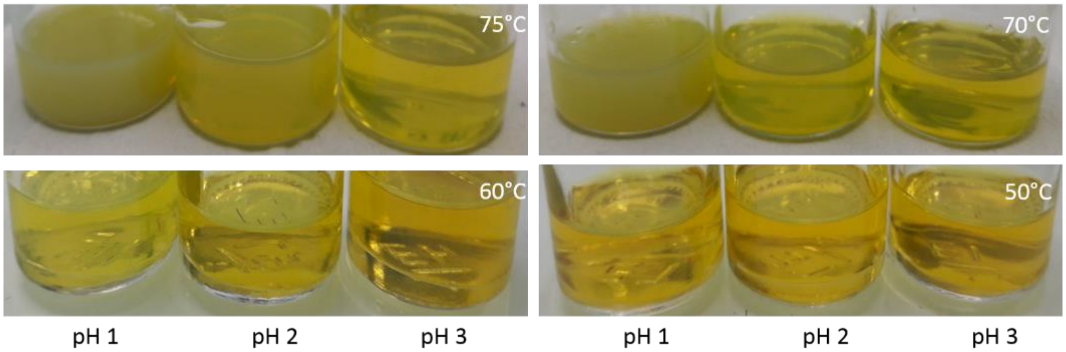

Figure II.1: An image showing the colour change in sols when synthesized at different pH and temperatures.

The modifications in the sol described in the experimental section were done in order to start the nucleation of TiO_2 nanocrystals within the sol itself and to study the effect of pH and synthesis temperature on this nucleation process. A change in the yellow colour of the sol to milky yellow was observed (Figure II.1) when increasing the synthesis temperature and decreasing the pH, especially for pH 1 at 70°C and 75°C and for pH 2 at 75°. The sol was stable for one week without precipitation. The initial sol which had a pH of 4.5 gave rise to amorphous TiO_2 films.

When stirred at 50°C or above, this sol (pH 4.5) became a gel and could not be deposited in a film form. For all the other pH and synthesis temperature values, films were deposited on a silica substrate, baked at 100°C for 30 minutes and analyzed by Raman micro-spectroscopy. The results are reported in Figure II.2a-c. At pH 1, crystal seeds appear (Raman E_g band of anatase TiO_2, Figure II.2) when increasing the synthesis temperature above 60°C, with a higher amount at the maximum synthesis temperature of 75°C. At 75°C, the three pH values lead to the emergence of nanocrystals, but lowering the pH clearly increases the amount of crystal seeds according to the increase in the relative amplitude of the band at 155 cm^{-1}. The results are summarized in Table II.1 below.

No nucleation was observed for 50°C synthesis temperature whatever the pH. At pH 3, a slight crystallization occurs from 70°C. At pH 2, the Raman band at 155 cm^{-1} emerges from 60°C but its amplitude is less than at pH 1. The best conditions to germinate anatase seeds in the sol itself are therefore for pH 1 at 75°C synthesis temperature; these conditions are used in the next sections when dealing with "sol with seeds".

Table II.1: Summary of films synthesized with sols having different pH and synthesis temperature. ✓ indicates nucleation of nanocrystals, × indicates amorphous phase of TiO_2 and • means no sample characterization due to gelification of the sol.

Synthesis T / **pH**	**50 °C**	**60 °C**	**70 °C**	**75 °C**
1	×	✓	✓	✓
2	×	✓	✓	✓
3	×	×	✓	✓
4.5	•	•	•	•

Further, the crystallization was not enhanced when the baking time was increased to several hours, clearly showing that the annealing time above 30 min had no influence on such samples for enhancing the crystallization inside the matrix (not shown here). To check if the crystal seeds were formed in the sol itself, Raman spectra were measured for the as-deposited film as-well and were found to be close to the ones measured after 100°C baking, as shown in Figure II.2d.

In our formulations, AcAc is added to complex inorganic titania precursors. This diminishes the hydrolysis and condensation of inorganic species, keeping the particle size to only a few nanometer. When the acid content is increased inside the sol, AcAc molecules are protonated (under their acidic form) and do not complex Ti oxo-clusters anymore. Without complexant, larger particles are able to form through hydrolysis, condensation and peptisation of the Ti precursors. In the right conditions, those particles grow big enough to trigger the nucleation of nanocrystals of several nanometers in size.[97] In our case, a higher acid content lower than pH 1 can lead to a higher crystallization, but hundreds of nanometers sized nanocrystals wouldn't be favorable to develop films for optical applications where light scattering is prohibited. Further, the synthesis temperature acts as an activation parameter along with pH in the sol thus accelerating the peptisation and crystallization process.[88]

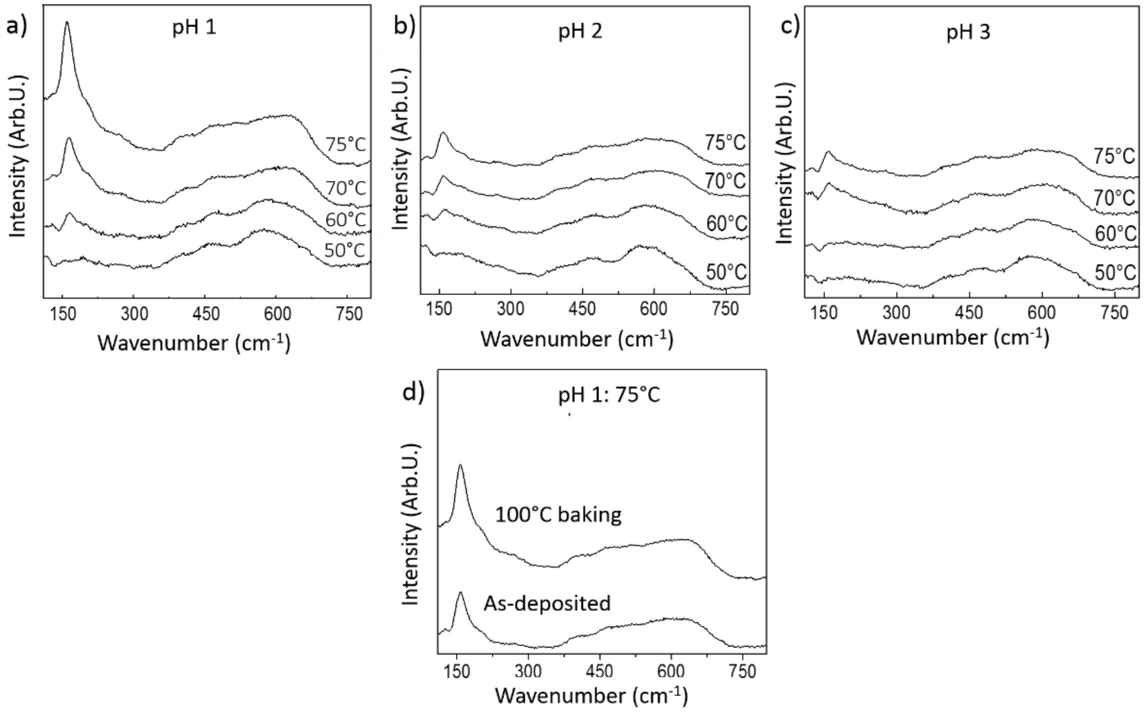

Figure II.2: The presence of crystal seeds is followed by the growth of E_g band of anatase TiO_2 at 155 cm^{-1}. Influence of the synthesis temperature for sol synthesized at a) pH 1. b) pH 2 and c) pH 3 respectively. A comparison of the E_g anatase band of TiO_2 for the as-deposited film and the film baked at 100°C/30 minutes for the sol at pH 1 and 75°C synthesis temperature.

3.2 Role of Crystal Seeds on the Temperature-Induced Crystal Growth and Phase Transition

We now investigate how the presence of seeds in the initial film influences the phase transitions and the isothermal crystal growth when the samples are subjected to temperatures ranging from 100°C to 1000°C. For this study we considered a sol without crystal seeds (initial sol at pH 4.5) and a sol with crystal seeds (pH 1-75°C). Silica substrates, which is known to be inert at such temperatures were dip coated using both the sols after the filtration using a 0.2 µm syringe filter and films were annealed at the above mentioned temperatures for 30 minutes each in a pre-heated oven as mentioned above.

Raman spectra of all samples are gathered in Figure II.3. For samples with seeds, the amplitude of the strongest E_g band of the anatase structure increases with the annealing temperature up to 700°C as well as the amplitude of the four other bands of anatase that only appear from 400°C, meaning that the amount of anatase in the amorphous titania phase increases with the annealing temperature and reaches a maximum at 700°C where traces of rutile band at 447 cm^{-1} starts developing. At 800°C and 900°C, anatase and rutile phases co-exist and anatase band disappears to the benefit of rutile at 1000°C. Considering the samples without crystal seeds, we observe that germination starts at 350°C and, regardless the considered temperature, the amplitude of all bands is always smaller than the one measured on a film with crystal seeds annealed at the same temperature. The content of nanocrystals in a film with seeds is therefore always higher than the one in a film without initial seeds after annealing at any temperature. Interestingly, the films without seeds exhibit a faster transition from the anatase to the rutile phase between 700°C and 800°C with a small amount of residual anatase at 800°C and 900°C respectively, and no anatase at 1000°C. The minute traces of anatase at 800°C and 900°C are characterized by the low band at about 144 cm^{-1} that is more likely for the anatase than for the rutile phase and that does not exist at the highest temperature when only rutile is present. It is to be noted that the bands mentioned for anatase at 197 cm^{-1} and for rutile at 235 and 447 cm^{-1} respectively for some temperatures, not clearly visible in the Figure II.3 are better observed in Figure II.5, later with a different scale. With, an increase in the annealing temperature, there is a shift in the lowest Raman frequency of the E_g anatase band along with the reduction in the Raman linewidth that can be seen in the Figure II.4a, which is attributed to the crystal growth as explained in the next paragraph.

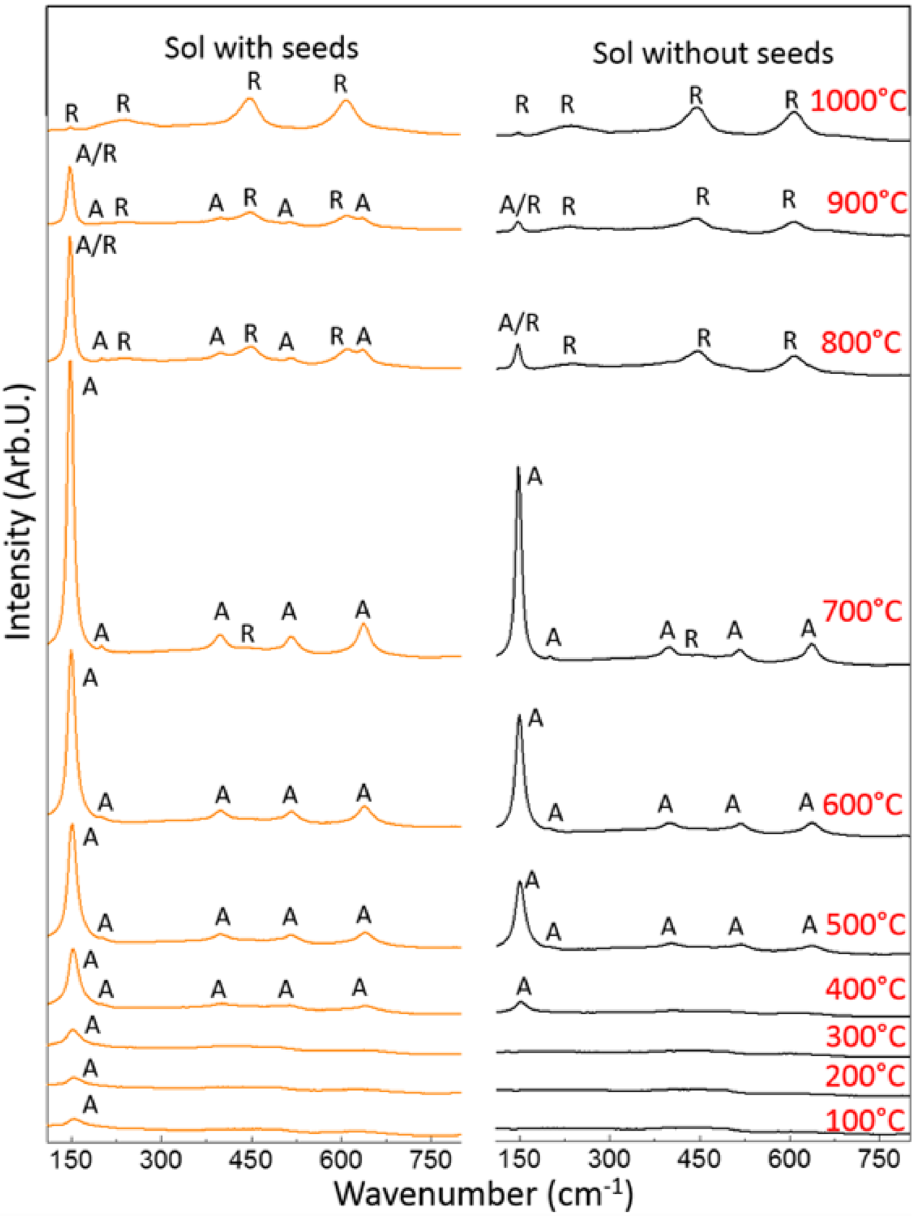

Figure II.3: Raman spectra of films with and without seeds after calcination at various temperatures. Spectra were measured in the same conditions and are plotted using the same intensity scale. A and R locate the different bands of the anatase and rutile phases, respectively

Further exploitation of such spectra can be performed in the framework of a phonon confinement model. When crystals are smaller than 100 nm, the description of atomic vibrations in terms of phonons with a well-defined wave vector is no longer valid because of the lack of translational invariance in a finite domain [98]. Raman scattering intensity can then be approximated at the first-order and for spherical nanoparticles by the following equation:[100,101]

$$I\ (\omega) \propto \int_{BZ} \frac{|C(0,\boldsymbol{q})|^2}{\{(\omega-\omega(\boldsymbol{q}))^2+(\Gamma_0\ /2)^2\}} d^3\boldsymbol{q} \qquad \text{(Eq. II.1)}$$

where Γ_0 is the Raman linewidth at room temperature (we consider the constant value of 7 cm^{-1} corresponding to bulk anatase), $\omega(\boldsymbol{q})$ is the dispersion relation of the phonon with the integral being performed over the entire Brillouin zone, taking account three-dimensional confinement ($d^3\boldsymbol{q} \propto q^2\boldsymbol{dq}$), and $|C(0,\boldsymbol{q})|^2$ is the phonon confinement function usually defined as:[100,102]

$$|C(0,\boldsymbol{q})|^2 = \exp\left(-\frac{q^2D^2}{16\pi^2}\right) \qquad \text{(Eq. II.2)}$$

where *D* is the crystallite size. Further, the phonon frequency $\omega(\boldsymbol{q})$ can be approximated by:[100]

$$\omega(\boldsymbol{q}) = \delta * [1-\cos(\mathrm{q}a_0)] + \omega_0 \qquad \text{(Eq. II.3)}$$

where a_0 = 0.3768 nm is the lattice parameter, $\omega_0 = 144\ \mathrm{cm}^{-1}$ is the zone center phonon frequency and $\delta = 20\ \mathrm{cm}^{-1}$ is the width of the phonon dispersion curve. By fitting the phonon confinement's model with the experimental values of the first E_g band of the anatase structure between 100°C and 700°C, we calculated the average crystallite size *D* for the different films. Figure II.4a zooms in the 110-200 cm^{-1} Raman frequency range used for fitting and shows bands of the sample with seeds normalized for an easier comparison of linewidths and positions. The higher the temperature, the narrower the linewidth and the lower the shift compared to the bulk frequency at 144 cm^{-1}.

The fitting results in the Figure II.4b show that such a spectral behavior corresponds to an increase in the nanocrystal size with the annealing temperature from 4.3 nm at 100°C to 13.7 nm at 700°C for sol with seeds. Calculations carried out for the sample without seeds yield nearly the same size values in the range where they are measurable, which starts at 350°C with an average crystal size of 5.6 nm. Thus, between 350°C and 700°C the presence of crystal seeds in the initial film increases the crystal content after annealing. These seeds, however do not significantly influence the crystal size, which mainly depends on the annealing temperature.

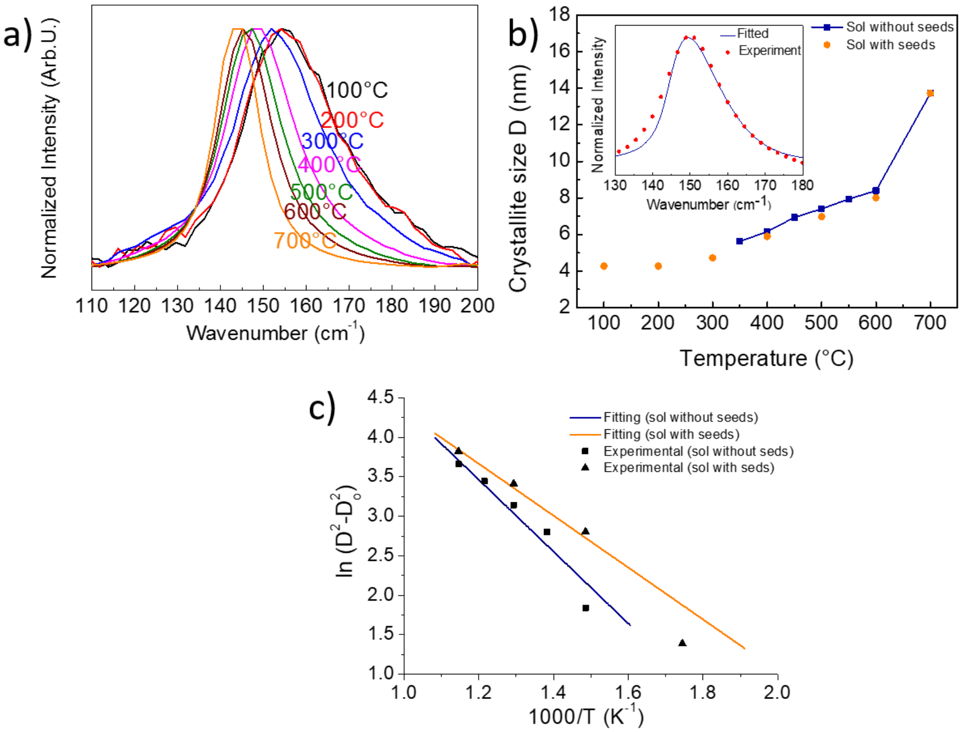

Figure II.4: a) Normalized first E_g band of the anatase phase measured on films with seeds as a function of annealing temperature. b) Average anatase nanocrystal size D versus annealing temperature for the two kinds of films calculated using a phonon-confinement model. An inset figure illustrates the accuracy of the model by showing the experimental and fitted curves of the film with seeds annealed at 400°C. c) Fits used for determining the activation energy of the crystal growth in both sample in the temperature range from 300°C to 600°C, as derived by the theoretical model relating the isothermal grain size D (nm) to the annealing temperature T (K).It's to be noted that units of kelvin have been used for depicting activation energy here.

It should be mentioned that other parameters could affect the position and linewidth of the first E_g band. The band can be shifted by an increase in temperature during the Raman measurements.[103] To neglect this effect all Raman measurements were carried out under the same configuration using a very low laser power that had no effect on the samples, even when baked at 100°C. A change in the oxygen stoichiometry of the crystal phase can also shift the band, as reported by Bassi et al., but the probability that the stoichiometry evolves significantly with the annealing temperature here is low.[100] We can thus consider that the selected model is the most suitable for estimating crystal sizes from our experimental data. However, it is useful to remind the conclusions drawn by Bassi et al. after assessing such a model for anatase TiO_2 nanoparticles produced by flame pyrolysis.[100] Discrepancies between calculated and experimental sizes may exist, resulting from the factors like the uncertainty on the dispersion relation of the anatase structure that has not been measured yet, the assumption of isotropic dispersion relations that is implicit in the model, the absence of consideration of surface effects for very small nanocrystals and the fact that the dispersion relation does not change with the crystal size.

The process of anatase crystal growth in the titania amorphous phase during isothermal annealing can be analyzed using a general equation for grain growth and the Arrhenius law as follows:[104]

$$D^n - D_0^n = kt\ exp\left(-\frac{E_a}{R'T}\right) \qquad \text{(Eq. II.4)}$$

where D is the crystallite size obtained after annealing at temperature T (K) for time t, which in this case is 30 minutes. D_0 is the crystallite size obtained at the lowest temperature leading to crystallization, n is the grain growth exponent, R' is the molar gas constant, k is a constant and E_a is the activation energy of the isothermal crystal growth. Terms k and E_a are assumed to be temperature independent. Otherwise the model is invalid and the fitted parameters do not represent any physical value. We used the value $n = 2$, which allows to make a comparison with related papers and corresponds to the standard model of normal grain growth and grain boundary migration.[105] However, better fits of experimental data can be obtained with other values of n (3, 4 and 5) for both seeded and unseeded samples (not shown here), emphasizing different grain growth mechanisms for the two kinds of samples. The calculated activation energies is tabulated in Table II.2 for different values of n. In all calculations, D_0 = 4.3 nm (first detectable crystal size at T= 100°C) or 5.6 nm (first detectable crystal size at T= 350°C) for the films with or without seeds, respectively. Figure II.4c shows the experimental values calculated from equations (II.1-II.4) for films with and without seeds for temperatures below 700°C, and straight lines that fit the data according to equation (II.4) showing activation energies of 27.3 kJ/mol (Ea≈0.29 eV) and 37.8 kJ/mol (Ea≈0.40 eV), respectively. One can note that the activation energy is slightly decreased when seeds are present. This is obtained whatever the value of n used for fitting, see the table below.

Table II.2: Activation energies as calculated with the different values of n. The activation energy for the sol with seeds is however lower each time with respect to the activation energy for the sol without seeds, whatever the value of n is.

n	**Sol with seeds** **E_a (kJ/mol)**	**Sol without seeds** **E_a (kJ/mol)**
2	27.3	37.8
3	32	40.9
4	36.9	44.4
5	42.4	48.3

For non-mesoporous TiO_2 films, Zhang et al reported the activation energy of 78 kJ/mol (Ea≈0.81 eV) for TiO_2 which corresponded to anatase re-crystallization by Ostwald ripening.[80] In their study, close activation energies were obtained for seeded and unseeded amorphous TiO_2 films, letting conclude that the growth was governed by atomic diffusion. In the previous work of Kohn et al., the activation energies were found to be 84.2 kJ/mol and 29.3 kJ/mol for temperatures above and below 400°C respectively.[79] The high temperature growth was attributed to the non-seeded crystallization, whereas the lower one was due to differing surface chemistries of the nanocrystal seeds, which is decisive for seed-induced growth from a surrounding amorphous phase. In our case, the lower activation energy obtained for seeded films can be related to the change in surface chemistry of TiO_2 nanocrystals that occurs when decreasing the pH. At pH 4.5, in the sol that leads to unseeded films, AcAc molecules complex with the titania precursor thus, limiting the size of amorphous TiO_2 nanoparticles and their crystallization. At pH 1, AcAc molecules are strongly protonated and do not complex with the precursor, which is expected to reduce their content in the film and to make the growth easier. This is coherent with the lower activation energy measured for seeded films and highlights the role of surface chemistry in the temperature range 400-600°C shown in Figure II.4c.

Comparing the values of activation energies we obtain for both mesoporous TiO_2 films with those reported in the above literature for non-mesoporous films, shows a significant difference at temperatures greater than 400°C. The presence of pores is known to limit the crystalline growth.[79] Here, we can infer, from comparison with previous works that porosity may be a factor that lowers the activation energy of crystal growth in amorphous TiO_2, and this may result from a higher mobility of atoms and the absence of ligands on surfaces.

3.3 Structural and Optical Properties of the Elaborated Films

To investigate the structural properties of the films synthesized by the two sols, electron microscopy techniques were employed. A SEM, using a FEI Nova nanoSEM 200 microscope was used in a low vacuum mode using a helix detector to measure the surface morphology of samples without conductive coating and high resolution TEM-HRTEM (high resolution TEM) experiments were carried out with a FEI Titan ETEM G2 80-300, operated at 300 kV to attest the presence of the crystal phase that were identified by Raman spectroscopy as illustrated in the Figure II.3, previously. Figures II.5a show the high density of anatase nanocrystals found in a film with seeds annealed at 400°C and confirms that the crystal size is well below 10 nm. At lower magnification at the cross-section, Figure II.5b shows the mesoporosity of film without seeds, annealed at 400°C. SEM micrographs systematically recorded on all films shows that the mesostructure on the film surface is very similar for both types of films (sol with and without seeds) upto 500°C, where some pores started to merge giving rise to larger pores and grains.

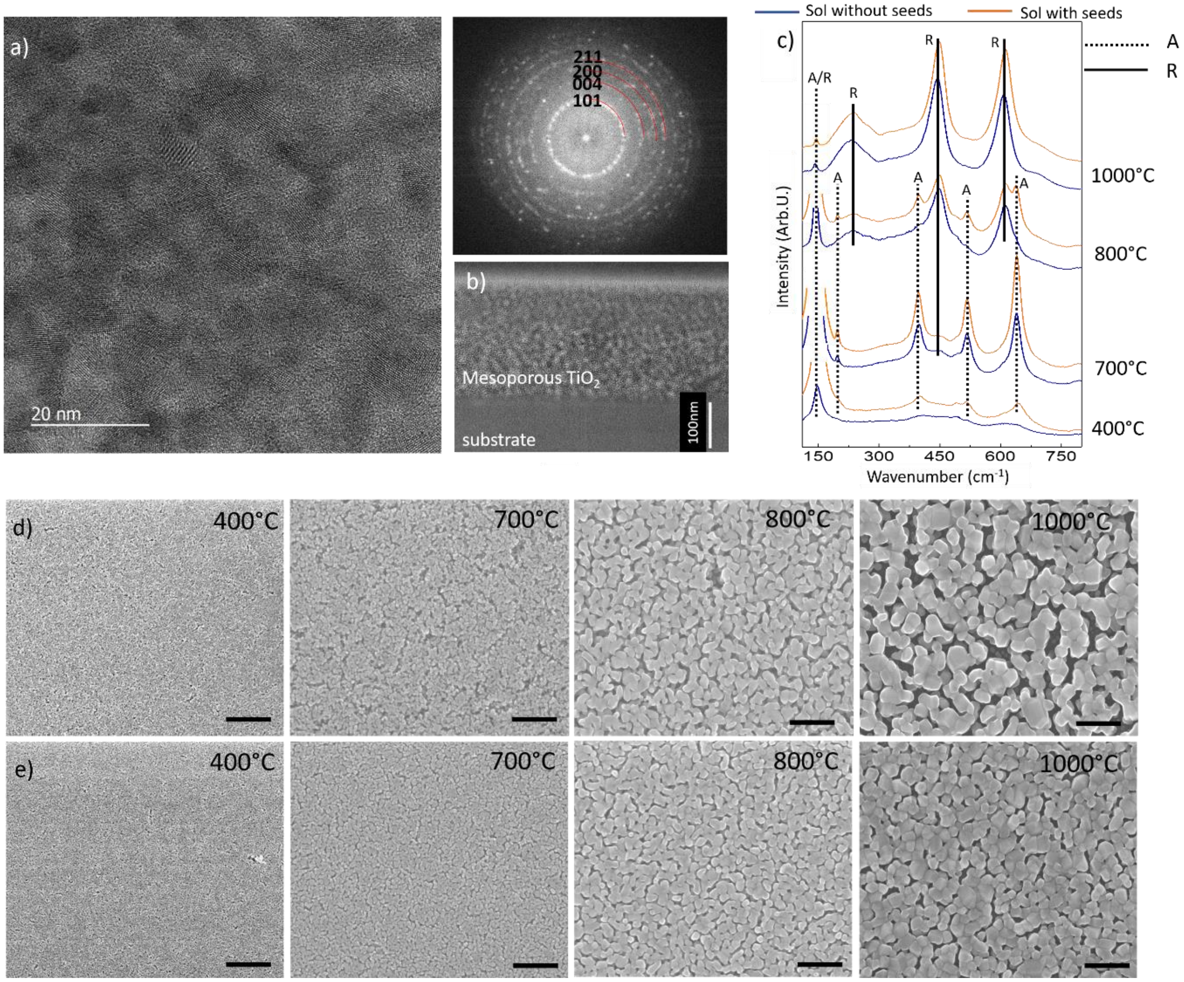

Figure II.5: a) HRTEM image of a film with seeds annealed at 400°C showing a large amount of small anatase nanocrystals. Adjacent Image:FFT of image (a) and identification of diffraction lines of anatase TiO_2. b) Cross-section of the mesoporous films without seeds. c) Selection of Raman spectra from seeded and unseeded films after annealing at 400°C, 700°C, 800°C and 1000°C and corresponding SEM images for seeded (d) and unseeded (e) film surfaces. The scale bars for all the SEM micrographs corresponds to 400 nm.

From 700°C, a clear difference occurs between seeded and unseeded films with larger pores and grains for sol with seeds (Figure II.5d-e). In this case, we observe increasing pore and grain sizes with annealing temperature, with larger sizes (up to about 200 nm) for samples with seeds (Figure II.5d). Whereas, the Figure II.5c shows the same Raman spectra as in Figure II.3 with a different scale to highlight the smaller bands of anatase at 197 cm^{-1} and anatase-rutile phases that co-exist in the unseeded film at 800 and 900°C for a clearer view.

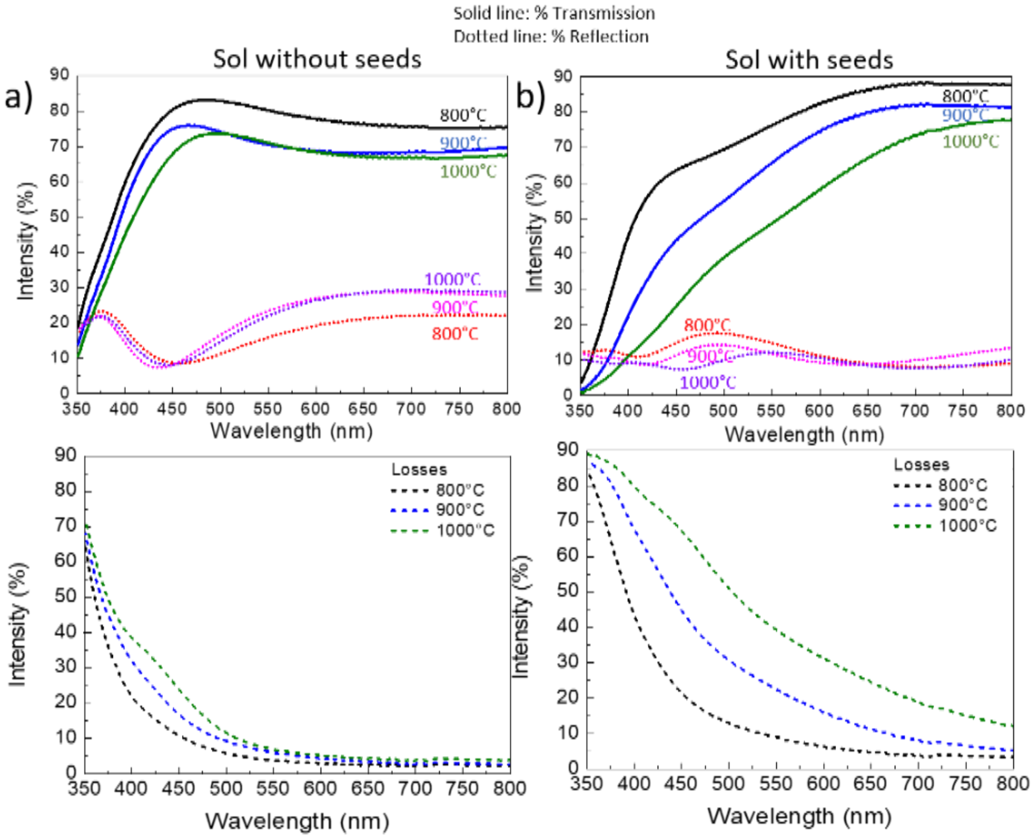

Figure II.6: The change in the spectral response for the films synthesized with two sols showing the possibility for the scattering effect in the films annealed above 700°C. The solid line depicts the % transmission along with the dotted line depicting % reflection for the temperatures above 700°C for a) sol without seeds and b) sol with seeds, where large opening of porosity is observed in the surface morphology of the samples. The corresponding graphs shows losses (scattering and absorption) for the seeded and unseeded films

From 800°C, samples were observed to scatter visible light exhibiting a milky blueish appearance in scattering reflection and a yellowish colour in transmission, in agreement with the large nanostructures observed on SEM pictures. This scattering behavior affects the transmission spectra (Figure II.6a-b) (measured using a Cary 5000 spectrophotometer from Agilent) where losses appear in the visible range with a typical $1/\lambda^x$ attenuation, where λ is the wavelength of light and x is an integer, the characteristic of scattering. We were not able to measure the amount of scattered light and thus could not precisely determine the contribution of scattering and potential absorption to the losses in the visible spectral range. Such samples may therefore, also exhibit absorption in the visible range.

Among the films annealed at temperature below 700°C, in which scattering can be neglected, the ones annealed below 300°C are not fully stabilized and can swell or shrink by nearly a factor two upon variations in the humidity range from 10 to 80% according to Bottein et al..[106] Their optical response can thus change significantly and are not reported here. In the range 300-600°C, the TiO_2 bandgap was estimated from transmittance and reflectance spectra (Figure II.6a-b) using the following equation:[107,108]

$$(\alpha' h\nu)^{1/n} = A(h\nu - E_g) \quad \text{(Eq. II.5)}$$

where, $h\nu$ is the photon energy, A is a constant and α' is the absorption coefficient given by:[109]

$$\alpha' = \frac{1}{\tau} ln(\frac{1-R}{T}) \quad \text{(Eq. II.6)}$$

where T and R are the transmittance and reflectance of the films (Figure II.7a-b), respectively, and τ the film thickness calculated with ellipsometry (Figure II.8b). The value of n depends upon the type of transition; n=2 for indirect and n=1/2 for direct transitions.[110] Anatase TiO_2 exhibits an indirect bandgap transition, so in this study we only considered the indirect transitions of TiO_2.[111] The energy band gap can be determined by extrapolating the absorption edge with the photon energy. Figure II.7d shows variations of band gap energy with the temperature in the range 300°C-600°C for the stable films with and without seeds. Figure II.7c shows the extrapolation method to determine the band gap values for film annealed at 600°C for sol with seeds.

The result shows that seeded films have a lower bandgap as compared to the films without seeds for all the mentioned temperature values, which is coherent with the higher content in anatase phase reported previously.[112] With an increase in annealing temperature from 300°C to 600°C, the band gap energy decreases from 3.33 to 3.25 and from 3.38 to 3.3 eV for the films with and without seeds, respectively, the value reported for bulk anatase TiO_2 being 3.2 eV.[113] Variations of the band gap with annealing temperature of our partly crystallized TiO_2 films are similar to the work of Lin et al., where a variation of 0.06 eV was reported between 300°C and 500°C.[114] Further, work by Mathews et al. showed a variation in the bandgap of TiO_2 films from 3.4 eV for the amorphous films (as-deposited) to 3.32 eV for crystallized anatase films (600°C).[112]

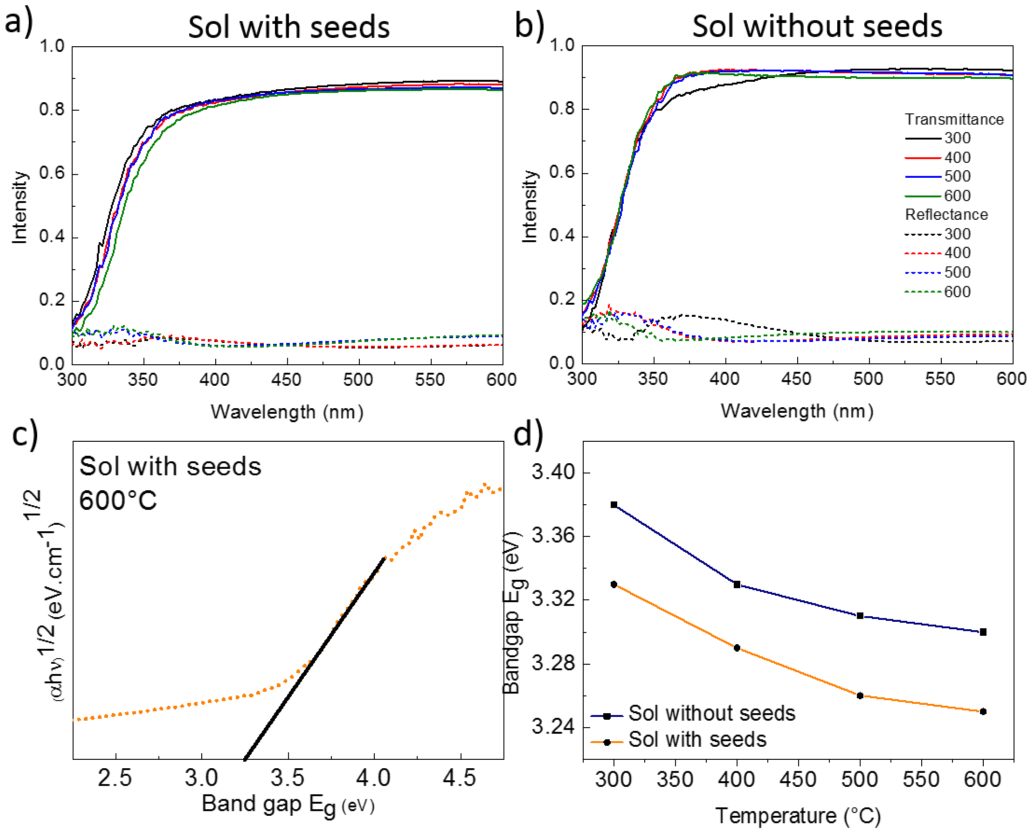

Figure II.7: The change in the spectral response for the films synthesized with a) sol with seeds and b) sol without seeds for the films annealed at 300, 400, 500 and 600°C. The solid line depicts the transmittance along with the dotted line depicting the measured reflectance. c) The band gap calculated while extrapolating the absorption edge; calculated from the transmittance and the reflectance values for the film made with sol with seeds annealed at 600°C. d) Changes in the band gap with temperature for films with and without seeds annealed between 300 and 600°C.

To further exploit the optical properties of such non-scattered and stable films, the refractive index dispersion and thickness of films were characterized using a spectroscopic Ellipsometry (Woollam M2000V) system equipped with micro-focused probes. Refractive index was measured using a Cauchy Model with a mean deviation ranging from 0.003 - 0.005 for the measurements. The Environmental Ellipsometric Porosimetry (EEP) measurements were carried out with the same equipment combined with an atmospheric control chamber. Water was selected as the adsorbate. The volume of adsorbed (and capillary condensed) water into the pores was followed through a time resolved measurement of the refractive index variation as a function of P/P_0. The volume of adsorbed water was then deduced from the refractive index using the Cauchy models and the Bruggeman Effective Medium Approximation (J A Woollam CompleteEASE software). The pore size distribution was then plotted using the Kelvin's equation and using a model for cylindrical pores.[115]

The evolution of the refractive index and thickness for films with and without seeds is displayed in Figure II.8a-b between 300 and 700°C, which are stable and non-scattering. For the seeded layer, larger particles were deposited with a lower organic to inorganic ratio due to the low complexant effect of protonated AcAc molecules. In those conditions, a steady increase of the refractive index with temperature is observed, originating from the densification and further crystallization of the layer. On the contrary, without seeds, the film contains a high organic to inorganic content (high concentration of complexant AcAc molecules at the surface of each titania cluster and high surface to volume ratio of small nanoparticles). During annealing, the organic compounds are first degraded, decreasing the refractive index of the film. At 500°C, the refractive index increases again due to the densification of the layer. The film thickness steadily diminish with temperature due to condensation and sintering regardless the formulation.

Further, environmental ellipsometric porosimetry was used to probe the porosity of the films. The results (Figure II.8c-d) show that the porosity of stabilized and non-scattering films is highly accessible (very low hysteresis between adsorption and desorption curves) thanks to the worm-like shape of the porous network and this whatever the annealing temperature. For the layer with seeds, the porous volume remains constant and only slightly diminishes at 700 °C from 57 to 54% due to the layer densification. For the layer without seeds, the porous volume first strongly increases between 300 and 400 °C (from 45 to $60\%_{vol}$) due to organic degradation. Above 400°C, the porous volume is mostly stable and decreases from 60% at 400°C to 55% at 700 °C due to the layer densification. The average pore diameter, extracted from the curves previously mentioned, steadily increases with temperature from 4 ± 1 nm and 3 ± 1 nm at 300 °C for the layer with and without seeds, respectively, to 11 ± 2 nm at 700 °C due to the network sintering, degradation of the organic compounds and elimination of areas of higher curvature (*i.e.* small pores).

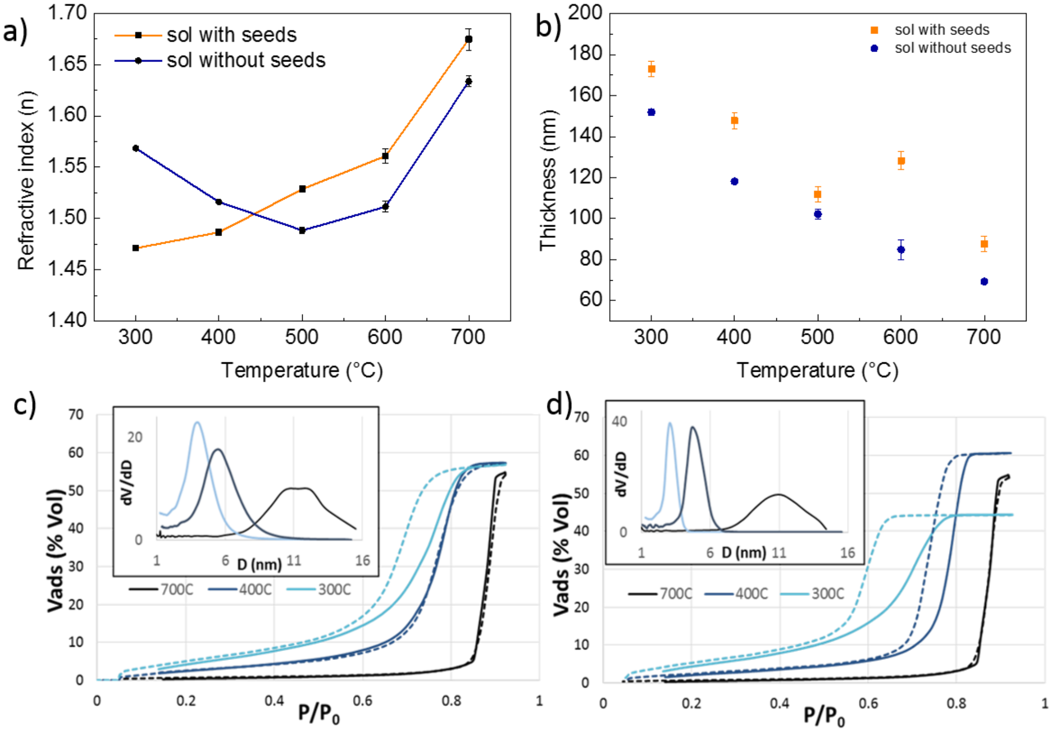

Figure II.8: Evolution of a) refractive index and b) thickness of films with and without seeds annealed between 300 and 600°C. c-d) Adsorption (full lines) and desorption (dotted lines) curves of films with (c) or without (d) seeds at 300, 400 and 700°C. Figures in inset show the pore size distribution extracted from the adsorption curve.

Such mesoporous crystallized films can be used for various applications including photocatalysis, laser-induced colour marking and photovoltaics with controlled proportions of crystalline phases and porosity. Partially crystallized TiO_2 films can also be deposited on substrates that do not withstand high temperature like plastic or paper for other industrial applications.

Next section of this chapter will discuss about the photochromic behavior of the films produced on the amorphous TiO_2 sol (published in our previous studies) as mentioned at the starting of this chapter. Such films are amorphous in nature and photochromic. Later, Chapter III is devoted to investigating the growth of Ag metallic nanoparticles with fs laser in such photochromic nanocomposite films. Further, such nanocomposite films can also be used for colour markings that are important for pplications to security for industries; a topic which is also focused in the following chapters. Thus, it becomes important to introduce steps where we can obtain photochromic transparent films after the introduction of metallic nanoparticles into the mesoporous amorphous TiO_2 films. Such nanocomposite films must be reproducible on a large scale when the applications to industries are concerned. The next section, will deal with the photochromic behavior of Ag:TiO_2 films along with the steps to produce such nanocomposite in a reproducible manner.

4. Optical Properties of Amorphous Mesoporous Ag:TiO_2 Films

4.1 Synthesizing Ag:TiO_2 Films

Even though, the process of Ag impregnation has been reported by our group in previous publications as discussed in the Introduction chapter I, a defined protocol needs to be reported when working for applications related to industries for mass production.[72] After obtaining mesoporous amorphous TiO_2 films from the normal sol at 340 °C annealing temperature, as reported before, or the amorphous TiO_2 films that will be discussed in Chapter III, IV and V, the films are heated at 140°C for an hour to remove any excess of water molecules that may have entered in the porous system due to adsorption of ambient humidity prior to the impregnation with Ag metallic ions solution. For a 1.5 M of Ag ionic solution, 5.09 g of $AgNO_3$ salt is taken in a beaker followed by an addition of 2.5 mL of DI and 17.5 mL of ethanol. The solution is then stirred at 300 rpm, after which liquid NH_3 is added to the above solution dropwise. At, this point the solution colour starts changing from transparent to brown. After an addition of approximately 12.12 g of NH_3 dropwise, the final solution again turns into transparent indicating the completion of reaction for the formation of $[Ag(NH_3)_2]^+$ solution. The dried films are then soaked in this solution by using a 0.2 µm syringe filter avoiding any micrometer size particles in the system. The films are then soaked in the dark for an hour after which the films are rinsed with DI carefully to remove excess of solution from the surface, followed by drying with nitrogen. The samples are then dried overnight for 12 hours before the next step of photochromic effect, discussed in the next sub-section.

4.2 Photochromic Behavior of Ag:TiO_2 Films

The Ag:TiO_2 film after drying overnight is exposed to UV light (two lamps of 15 W giving an intensity of 50 mW/cm^2 on the sample) at 254 nm for 5 minutes after which the initially transparent film turns brown. After this step, the film is exposed to white light source (LCS-100, Newport solar simulator) for 3 hours with a long-pass filter at 495 nm to cut the UV-blue domain. The film at this step, looks transparent and is bleached completely (Figure II.9c). A continuous exposure to UV and white light is termed as one cycle here. The sample is exposed to two cycles more to completely stabilize the films at the end, where a bleached film is obtained whose colour remains stable for at least one day when used under ambient conditions. To investigate the reproducibility of films, six different films of mesoporous amorphous TiO_2 were taken and impregnated with the Ag ionic solution with the protocol mentioned above. Followed by three UV-bleaching cycles, the absorption spectra were measured. It was observed that for the six films produced, there was a difference of 2% in the absorption spectra (Figure II.9a-b) after the last bleaching cycle, showing the reproducibility of such films if the right protocol is followed. Figure II.9c shows the image of the six Ag:TiO_2 nanocomposite films after the first UV irradiation showing the brownish colour obtained and the bleached samples after the last cycle of bleaching.

After this defined protocol, the bleached films can be used for colour processing as they do not evolve over time when kept under a cover of aluminum foil to avoid any outer light and do not significantly evolve under ambient light during a day of experiment. Such stabilized films give much more reproducible results on various samples when compared to TiO_2 films impregnated with Ag solution and then exposed to just UV light to grow nanoparticles without any stabilization process; The latter evolve over time. Figure II.9b shows the absorption taken at 515 nm, which is the laser wavelength used with femtosecond laser for the generation of plasmonic colours, illustrating the photochromic behavior on such samples (reversible changes of colour upon UV and visible light exposure).

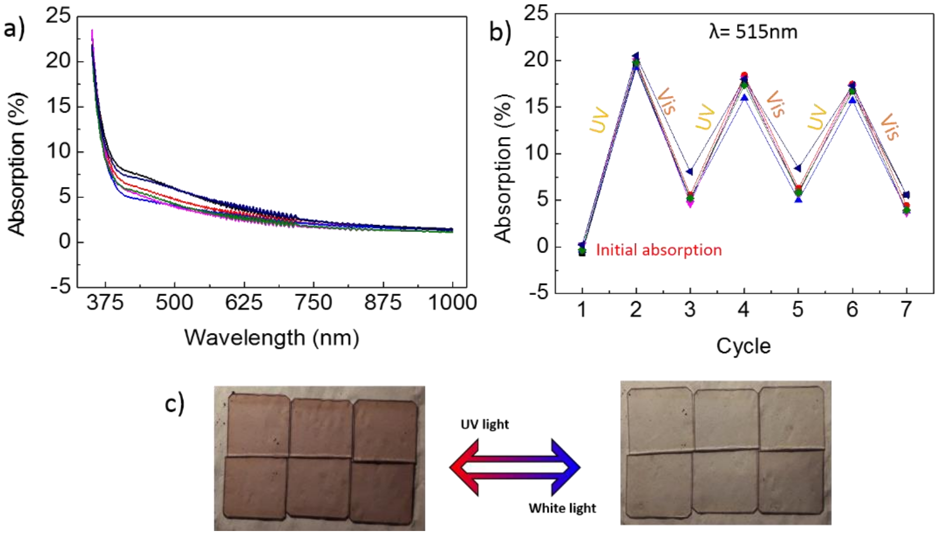

Figure II.9: a) Absorption spectra for the six different films after the third cycle bleaching. b) Absorption for the three-cycle UV/bleaching for six different films measured at 515nm (laser wavelength for applications). c) Colour change of films from brown to transparent, showing the photochromic behavior of the nanocomposite films.

5. Conclusions

In this chapter an easy and rapid synthesis sol-gel route is shown to produce mesoporous semi-crystalized TiO_2 optical thin films starting at 75°C via a hydrolytic process. Initiation of crystallization in the sol is a result of an acid assisted sol-gel method, which is facilitated by the temperature increase during the sol formation. Limiting complexation of AcAc with the titania precursor by lowering the pH to 1 allows the formation of crystal seeds near the boiling point of ethanol. The comparison of seeded and unseeded films during isothermal annealing allows to draw conclusions about their different thermal behaviors. The activation energy of the crystal growth is lowered by the presence of seeds in the film and by a high atomic diffusion in the porous structure. The anatase nanocrystals content is always higher in seeded films as compared to unseeded films after isothermal annealing and the band gap is decreased with the increase in the anatase content. In seeded films, the anatase crystal phase coexists with the rutile phase from 700°C until 900°C, while the rutile phase strongly predominates from 800°C in the unseeded film. Due to the presence of a larger organic content in the unseeded films, changes in the pore volumes and refractive index exhibit a non-monotonous behavior at increasing temperature from 300°C to 700°C, while the seeded films only exhibit temperature induced densification. Partially crystallized TiO_2 films can be deposited on different substrates that do not sustain high temperature, like plastic or paper for applications to photocatalysis and other industrial use.

In the end, the photochromic behavior of the $Ag:TiO_2$ nanocomposite films were discussed, prepared using amorphous TiO_2. The reproducibility of such films could be obtained when following a defined protocol for the inclusion of the metallic ions. Such films show photochromic behavior and are used after bleaching. The next chapter focuses on the growth and self-organization of Ag nanoparticles inside amorphous TiO_2 films using femtosecond systems. A deep investigation is carried out to synthesize different nanocomposite structures resulting in dichroic plasmonic colours which is followed by the applications in the followed chapters.

CHAPTER III

TAILORING NANOCOMPOSITES OF Ag:TiO_2 WITH FS LASERS

After the previous chapter of the thesis that focuses on crystallization of the TiO_2 matrix starting from low temperatures and understanding the crystal growth mechanisms in seeded and non-seeded TiO_2 films , we now discuss how tailoring the colour and dichroism of nanocomposites of Ag:TiO_2 using fs laser. As discussed in the previous chapter, photochromic Ag:TiO_2 films are developed using a defined protocol to stabilize the films for laser processing. Such bleached films provide repetitive results over different samples, as the initial nanoparticles inside the films does not alter much with time, which becomes important especially when considering industrial applications. Further, not to confuse the users with the crystallized films discussed in the previous chapter, in the upcoming chapters, when Ag:TiO_2 films are considered, these are the samples with amorphous TiO_2 matrix and not the crystallized TiO_2. The chapter III, was possible after collaborating with the Research Scientist "Jan Siegel" at CSIC and post-doc Camelio Florian, Madrid Spain

1. Introduction

Metal nanoparticles are key players in modern strategies to fabricate nanocomposite materials with exceptional properties, not offered by nature. Interaction with light triggers collective oscillations of electrons at the nanoparticle surface, also known as LSPR, which determines the optical response of the system. The LSPR is related to the size, shape, separation and orientation of the nanoparticles, along with the refractive index of the surrounding matrix. Although this dependence provides an opportunity for tailoring the spectral response of the system to match specific applications,[116,117,118] the interrelation of all parameters complicates this problem enormously. Thus, most fabrication techniques fail to produce nanoparticles with a high degree of symmetry, featuring broad distributions in size, shape, orientation, and consequently only weak LSPRs.

Another possibility for shaping the optical response of a material is by arranging nanoparticles with moderate symmetry and size distribution into gratings or lattices with medium or long-range order. The optical response of such “superstructures” can be tuned conveniently by changing the grating or lattice period, which is simpler than tuning individual nanoparticle characteristics. Fabricating such structures with top-down approaches such as lithography, in which a pattern is imprinted by photons, electrons or ions, would be prohibitive in terms of time and cost. A superior methodology is to exploit self-organization processes, a bottom-up technique which is capable of arranging micro- and nanometer size objects to form extended periodic structures.[119,120]

One strategy to fabricate such nanoparticle structures is based on the use of nanostructured substrates in order to achieve controlled growth of regular arrays of Ag nanoparticle chains[121] or stripes.[122] Another approach, not requiring the use of patterned substrates, is based on physical vapor deposition at glancing angle combined with subsequent laser treatment, leading to preferential melting and merging of certain nanoparticles.[123] Both techniques, though, are limited to obtain non-protected nanoparticle structures located at the substrate surface, which is troublesome in case of silver, which degrades through oxidation, accompanied by a corresponding change in its LSPR.[124]

Although the above techniques can be complemented by an additional step of cover layer deposition to protect the nanoparticles, single-step techniques would be desirable as they result in lower fabrication costs of devices. Such techniques can be grouped in two approaches, based either on re-shaping and re-ordering, or growth and self-organization of nanoparticles. The first strategy exploits the high peak intensity of low repetition rate fs laser pulses to change the nanoparticle shape and even rearrange them, overcoming the large forces exerted by the dielectric matrix.[14,125,126] The second approach relies on the use of porous dielectric titania films loaded with Ag nanoparticles, in which nucleation, growth and self-organization can be triggered by irradiation with cw laser light, as shown by our group.[72] Recently, the beneficial influence of thermal accumulation using fs laser pulses has been reported for such systems, enabling the growth of Ag nanoparticle structures in mesoporous amorphous TiO_2 films.[18] In that work, only two specific types of nanocomposites were fabricated as discussed in first chapter by using two different laser scan speeds at a constant laser fluence.

In the present chapter, a wide range of scan speeds is systematically explored, which allows to considerably extend the type of structures that can be fabricated from the previous work. Moreover, we demonstrate how the choice of laser polarization allows us either to generate or to prevent polarization anisotropy in the spectral response of the samples. In addition, a fabrication strategy based on interlacing two different nanocomposite structures produced with two different scan speeds is used, yielding hybrid nanostructures. The broad spectral range covered by the different structures illustrates their potential for smart visual effects and other photonics – based applications.

1.1 Thin Film Fabrication

The films are elaborated by sol-gel process, exactly similar to that for the normal sol discussed in the last chapter but with just a change of acid used, from HNO_3 to HCl. A change in the acid for the sol used to study crystallization, as discussed previously, was made as HNO_3 acid is less reactive for substrates such as polycarbonates and PET's when compared to HCl. A change in acid is not supposed to make a difference while the interactions with lasers is concerned. So for applications of such films to lasers, the previously elaboration process was not changed. Although, in some cases the films are dip-coated or spin-coated according to the substrate dimensions and the applications.

From this chapter and following until the chapter concerning applications to image multiplexing (Chapter V) where fs is considered, the films with the following precursor will be used; although the elaboration process for coating may vary. Here, TTIP, Aldrich; 97%, AcAc, Aldrich; 99%, HCl, Roth; 37%, EtOH, Carlo Erba; absolute, Pluronic P123 ($(PEO)_{20}(PPO)_{70}(PEO)_{20}$ (Aldrich; MW: 5000), and DI were taken with similar molar ratios at: TTIP:P123:EtOH:HCl:DI:AcAc :: 1:0.025:28.5:0.015:29.97:0.5, as previously discussed in the chapter II while discussing normal sol. The sol was stirred for 7 hours for stabilization here. The glass slides were cleaned with a defined protocol of sonication with acetone, EtOH and DI for 30 minutes each and drying with nitrogen. The films were dip coated at 7 cm/min rate while, staying for 1 minute in the sol after which the films were annealed at 340°C with 1°C/min temperature rise, to obtain mesoporous amorphous titania thin films. The films are impregnated with Ag by soaking the film in a silver nitrate solution (1.5 M). The ions are partly converted into silver atoms and small silver nanoparticles under UV light (254 nm, 6 mW/cm², 10 min). After which, a process of bleaching with solar lamp is followed. Such cycles (detailed in chapter II) are repeated to have nearly transparent and stable films at the end. The transparent films allows to have repetitive results with lasers for different films. Figure III.1, shows the spectra of the bleached films, for transmission, reflection and 1-R-T (absorption and losses). It is observed that, after bleaching the films absorbs very slightly in the visible and are nearly transparent.

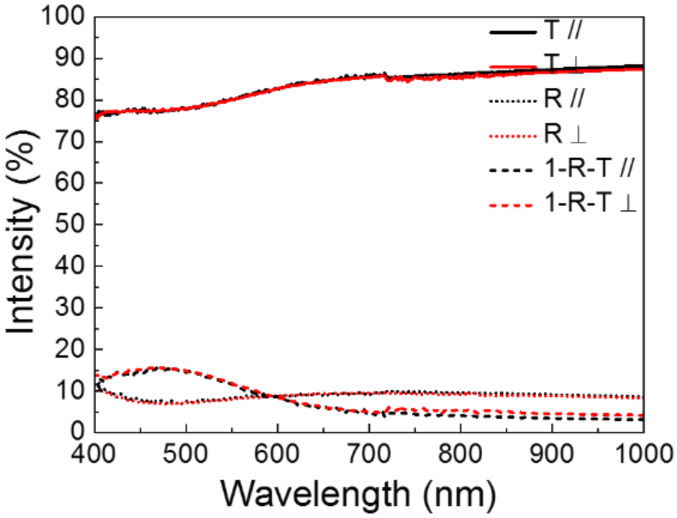

Figure III.1: a) Transmittance (T) and reflectance (R) spectra taken at 6° incidence angle for the initial Ag:TiO_2 nanocomposite films. Losses including absorption and scattering were calculated as (1-R-T). ⊥ and ∥ refers to the probe polarization, respective to the laser polarization

1.2 Laser Setup

The laser system used at CSIC was a fiber-amplified fs laser system with a pulse duration of 340 fs and a fundamental wavelength of 1030 nm, working at a repetition rate f_{rep} = 500 kHz. In order to excite the LSPR of the Ag nanoparticles, the fundamental wavelength was frequency doubled to 515 nm, using a BBO crystal. This assures the non-absorption of this wavelength by the titania matrix or the glass substrate, the laser fluence being low enough not to allow two-photon absorption by the latter. The incidence pulse fluence was adjusted using a half-wave plate combined with a thin film polarizer, which was followed by another half-wave plate or quarter-wave plate for controlling the laser polarization. The beam is delivered by a galvanometric scanning system (Figure III.2) combined with an f-theta lens of focal length 10 cm, focusing the laser beam on the sample surface with a beam diameter d = 33 µm ($1/e^2$ intensity). The advantage of using a galvanometric head is that, one can reach rapid scan speeds. The corresponding effective number of pulses (N_{eff}) in each case can be calculated for overlapping scan lines as $N_{eff,2D} = (\pi \cdot (d/2)^2 \cdot f_{rep}) / (v \cdot dy)$, and for single scan lines as $N_{eff,1D} = d \cdot f_{rep} / v$, where v is the scan speed in mm/s, dy is the distance between two successive laser lines, and d corresponding to beam diameter.

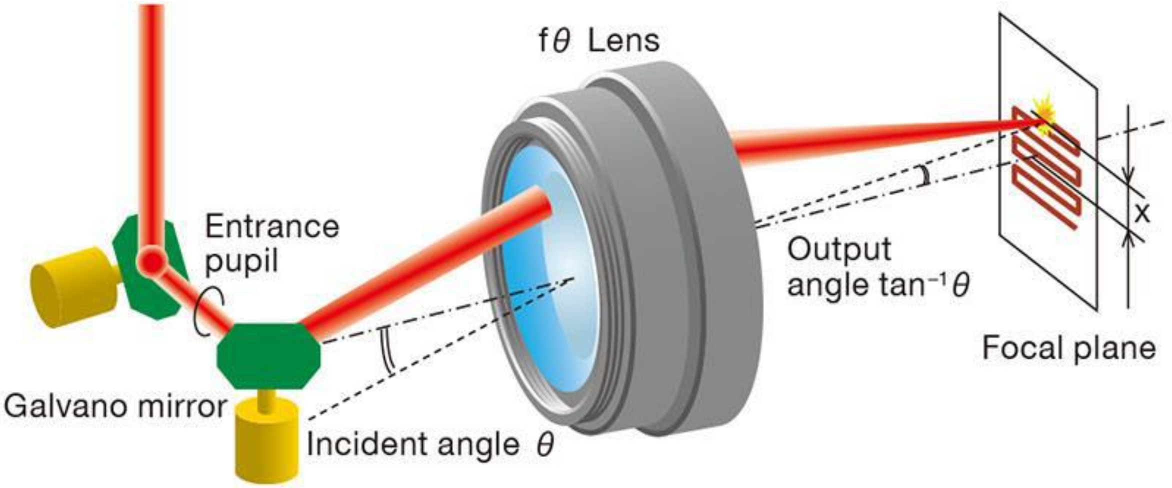

Figure III.2: a) Schematic of a galvanometer scanner completed by a F-theta lens to perform laser scans over a large area. Image source: OptoSigma.

2. Femtosecond (fs) Irradiations on Ag:TiO$_2$ Nanocomposite Thin Films

2.1 Scan Speed Study

The laser parameters of this study were chosen to investigate the formation of the nanocomposite structures as a function of scan speed, ranging from 1 mm/s to 200 mm/s at a constant laser fluence (F = 47 mJ/cm^2). Each structure was laser-written with a 2 µm spacing between scan lines and covered an area of 9 mm^2. The homogeneity of the structures achievable with the fabrication method can be best appreciated by optical inspection of the colour change for speeds ranging from 1 to 170 mm/s. Above 170 mm/s, the colour starts fading. Figure III.3 shows images of different laser written areas recorded with a smartphone camera, illustrating smart visual effects of the dichroic colours produced using a change of the scan speed.

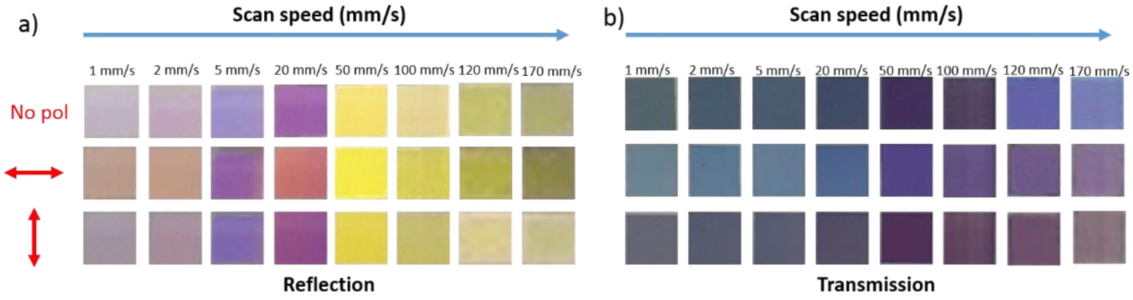

Figure III.3: a) Illustration of the colour changes induced by scanning high repetition rate femtosecond laser pulses over the sample surface at different speeds and constant fluence. Each square is imprinted over an area of 9 mm^2. Illumination was provided by a white light source for unpolarized (No pol) and horizontally/vertically polarized light (denoted by double sided arrows) and the image was recorded with a smartphone camera (a) in reflection and (b) in transmission.

The different nanostructures responsible for these optical responses were investigated using SEM and Atomic Fore Microscopy (AFM). The details for SEM have been provided in chapter II. While for AFM, an Agilent 5500 is used in this work to quantitatively characterize the surface topography of samples with nanometer resolution in tapping mode. In this study, AFM is a useful tool to characterize the LIPSS on the nanocomposites.

Figure III.4 shows the respective SEM and AFM images of four different nanocomposite structures obtained at speeds of 1, 20, 100 and 170 mm/s. The speeds were explicitly chosen, where a change in the nanostructure was observed. In all cases, the size of initially very small nanoparticles (< 3 nm) increased considerably and is resolved by SEM, yielding sizes in the range of 20 nm – 80 nm. While differences in nanoparticle size between the four structures can be appreciated, the most striking difference is the nanoparticle arrangement, caused by different self-organization processes.

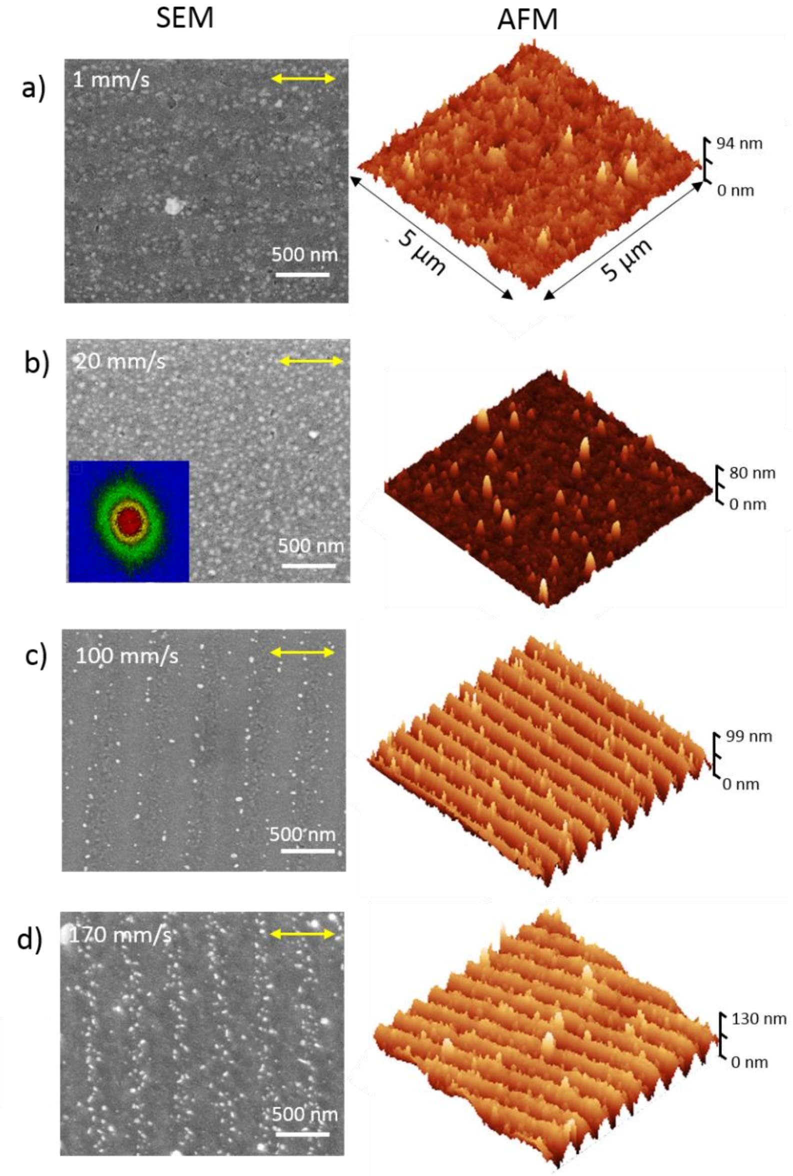

Figure III.4: Illustration of the evolution of the nanocomposite structure with the scan speed, characterized by their respective SEM and AFM images for a) 1 mm/s b) 20 mm/s c) 100 mm/s and d) 170 mm/s scan speeds. The embedded grating (EG) for speed v = 1 mm/s is formed parallel to the laser polarization (depicted by double side yellow arrows), whereas the surface grating (SG) at v = 100 mm/s and 170 mm/s is oriented perpendicular to the laser polarization.

At a high speed of v = 170 mm/s (Fig. III.4d), a surface grating is formed with an amplitude of 60 nm and a period of $\Lambda_{170mm/s}$ = 498 ± 20 nm, calculated using Gwyddion software. The nanoparticles mainly grow along the grating ridges on the top surface and their top view shape is either spherical or elongated but with no particular orientation. A decrease in the scan speed to v = 100 mm/s (Fig. III.4c) leads to a surface grating whose amplitude and period are smaller, at 40 nm and 474 ± 20 nm respectively, and in which nanoparticles start getting buried. This structure is similar to one of the structures reported by the former PhD of the nanoparticle group Zeming Liu [18] obtained at this speed and belongs to the class of LIPSS, which can be induced in metals, semiconductors and dielectrics upon irradiation with multiple laser pulses.[127,128,129,130] With a decrease in speed to v = 20 mm/s (Fig. III.4b), the nanoparticles distribute randomly beneath the TiO_2 surface. An inset in Figure III.4b shows a fast Fourier transform (FFT) of the SEM image, illustrating a slight anisotropy related to the laser polarization. The shape of the FFT pattern might indicate a nanoparticle shape slightly elongated along the laser polarization.

An influence of the laser polarization on the shape of Ag nanoparticles was reported previously in different systems and resulted from a series of processes; following the excitation of hot electrons through plasmonic absorption, metallic nanoparticles ionize after releasing electrons in the surrounding matrix mainly along the laser polarization, where the field enhancement is higher. The ionization is followed by an isotropic Ag^+ ion ejection. The latter can reduce on the nanoparticles again, along the axis where electrons are concentrated, leading to nanoparticles that tend to elongate along the laser polarization.[125,126,131] Further, at the lowest scan speed of v = 1 mm/s (Fig. III.4a), the nanoparticles self-arrange into horizontal stripes, parallel to the laser polarization, with a period $\Lambda_{1mm/s}$ = 344 ± 20 nm. This nanoparticle structure is embedded inside the titania matrix, which can be seen by the low contrast of the white embedded Ag nanoparticles compared to the random single nanoparticles that can be seen at the sample surface. The fact, that the nanoparticle grating is embedded can also be appreciated by the AFM map displayed in Fig. III.4a, featuring no visible periodic surface structure. This structure is similar to one of the structures reported in the former work of Liu et al. obtained at 10 mm/s,[18] but shows no residual periodic surface modulation perpendicular to the grating. It is worth emphasizing that this grating structure is fundamentally different from the surface grating observed at v = 100 mm/s and 170 mm/s, since it is aligned parallel to the laser polarization, rather than perpendicular, has a significantly smaller period and is embedded inside the film. The grating period and the errors, were calculated using ImageJ on different magnified SEM images for respective scan speeds.

The results shown in Fig. III.4 clearly demonstrate the existence of two different grating types, along with the transition from one type to the other. For simplicity, the two types are referred as, embedded grating 'EG' (formed at low speed) and, surface grating 'SG' (formed at high speed). The underlying reason, why a change of the scan speed leads to this strong change in the nanostructure, is related to the different number of effective pulses incident on a given area, as explained in the Introduction.

2.2 Two Different Self-Organization Processes

Depending on the pulse number, the relative weight of the numerous laser-induced processes (hot electron generation, silver ion ejection and reduction, heating, Oswald ripening, coalescence, and nanoparticle growth) is changed. The starting point – and underlying reason for grating formation – is the excitation of directional modes by the linearly polarized ultrashort laser pulse; a guided mode inside the TiO_2 film,[72] which leads to embedded gratings, and a surface mode in form of a surface plasmon polariton, which leads to surface gratings.[18,132] Both modes can be excited by the heterogeneities of the randomly distributed silver nanoparticles in the initial nanocomposite film. These modes propagate in orthogonal directions and interfere with the incident wave, giving rise to orthogonal intensity modulations with different periodicities. The surface grating always occurs first when increasing the number of pulses. The initial sample contains a high density of small nanoparticles mainly located in the top part of the film. Charge transfers from the excited nanoparticles to the TiO_2 occurring during each fs laser pulse are likely to transiently turn the film into a metal-like film and to allow the excitation of a surface plasmon polariton for which a positive feedback may occur when the grating starts forming, but only for the transverse magnetic (TM) polarization, i.e. for a grating perpendicular to the incident laser polarization. As shown in the previous article of Liu et al.[18] and chapter I, the very smooth surface grating that forms in such conditions mainly results from a local densification of the mesoporous film rather than matter ablation. When increasing the pulse number, nanoparticles grow more while their density decreases, leading to less charge transfers from the nanoparticle surface to the surrounding matrix (decrease of the surface/volume ratio), to more optical scattering in the film (larger size) and to larger heating (increased absorption). The reduced number of hot electrons transferred to the titania matrix is expected to affect the metal-like behaviour and the excitation of the surface mode. At the same time, the increased heating in the film tends to crystallize the titania matrix and collapse the film mesostructure, independently of the surface grating thus, leading to a flattening of the surface profile. Simultaneously, the increased scattering of embedded nanoparticles favours the excitation of guided modes, which is enhanced by the embedded grating formation, provided that its orientation is parallel to the incident polarization (only the transverse electric (TE) polarization allows efficient diffraction into a guided mode). This condition therefore creates a positive feedback, leading to the generation of an embedded nanoparticle grating parallel to the laser polarization. Experimentally, after the surface grating generation (v = 170 mm/s), an increase in the pulse number leads to the growth of embedded nanoparticles (v = 20 mm/s) with a surface flattening, followed by the formation of the embedded grating (v = 1 mm/s), confirming the successive appearance of the described mechanisms. Depending on the scan speed (effective pulse number) it is possible to enhance or supress certain processes and effectively imprint an embedded grating corresponding to the guided mode, a surface grating corresponding to the surface plasmon polariton, or no grating.

For both, the guided and surface modes, the grating period is calculated by:

$$\Lambda_{EG,SG} = \frac{\lambda}{Re(\eta)} \qquad \text{(Eq. III.1)}$$

where λ is the laser wavelength (515 nm) and Re(η) is the real part of the complex effective index experienced by the propagating mode.[133,134] For the guided mode:

$$\mathrm{Re}(\eta) = n_{gm} \qquad \text{(Eq. III.2)}$$

which corresponds to the effective refractive index of the guided mode when the embedded grating starts forming. The grating period values of the different structures (determined from SEM images) are plotted as a function of the scan speed in Figure III.5. For v = 5 mm/s, where embedded nanogratings (EG) are formed with parallel orientation to the laser polarization, the grating period was measured as $\Lambda_{5mm/s}$ = 329 ± 20 nm. The period increases slightly towards lower speeds, yielding a maximum value of $\Lambda_{1mm/s}$ = 344 ± 20 nm. Both values are consistent with the mechanism of embedded grating formation via a guided mode with n_{gm} ranging between 1.50 and 1.57. The latter should be larger than the refractive index of the substrate, 1.46, and lower than the refractive index of the mesoporous titania film loaded with silver nanoparticles. Interestingly, the measured periods are also consistent with the one obtained for embedded nanogratings obtained using cw laser on the same nanocomposites ($\Lambda_{cw-laser}$= 318 nm, with λ = 530 nm and v = 0.6 mm/s).[72] The similarity of the structures formed upon ultrashort or cw laser irradiation, in particular the very similar scan speed values used, suggests that the underlying mechanisms are comparable. This hypothesis is supported by the fact that the ultrashort laser pulses are delivered with a very high repetition rate (f = 500 kHz), which leads to a strong heat accumulation effect and therefore generating similar thermal conditions as for cw laser irradiation when accumulating a large number of pulses per unit area.

For surface mode excitation, the physics is different. Due to the high initial density of small Ag nanoparticles in the titania film, combined with the large peak intensity of the fs laser that leads to an increase of the free electron density, the material develops a metal-like state and plasmonic behaviour. This allows coupling of the laser light into a surface plasmon polariton (SPP), which propagates along the direction of the electric field vector. In this case, the relevant effective refractive index for the grating period can be obtained from:

$$\eta = k_{SPP}^{0} \cdot \lambda/(2\pi) = [(\epsilon_{air} \cdot \epsilon_{metal})/(\epsilon_{air} + \epsilon_{metal})]^{1/2} \quad \text{(Eq. III.3)}$$

with k_{SPP}^{0} being the SPP wavevector on a planar air-metal interface with ϵ_{air} and $\epsilon_{\mathrm{metal}}$ being the dielectric functions of air and metal. Typically, for metals Re$(\eta) \approx 1$, which yields a grating period that is close to the laser wavelength used, $\Lambda_{SG} \approx 515$ nm.[135]

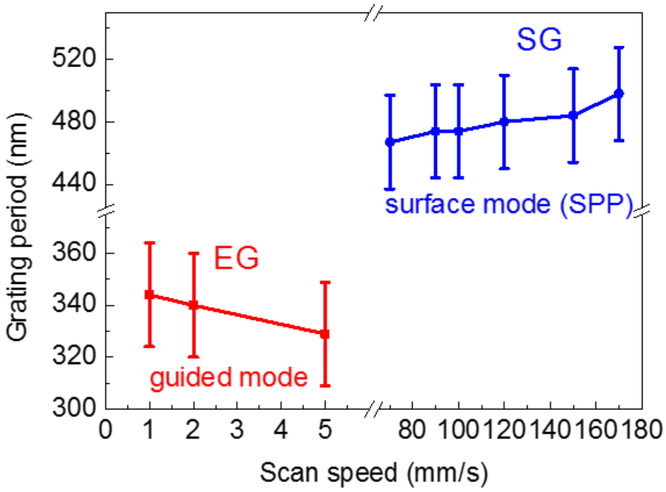

Figure III.5: Evolution of the period of the nanostructures that feature gratings with the scan speed. For speeds in the range v = 1 - 5 mm/s, an embedded grating (EG) is formed inside the film and its orientation is parallel to the laser polarization. For the range v = 70 – 170 mm/s, a surface grating (SG) is formed, whose orientation is perpendicular to the laser polarization.

For the speed range where surface gratings (SG) are formed, the evolution of the period is different from that of EG, as seen in Fig. III.6. At the lowest speed within this range, surface ripples with a period of $\Lambda_{70mm/s}$ = 467 ± 30 nm are formed. The period gradually increases with speed up to $\Lambda_{170mm/s}$ = 498 ± 30 nm. As discussed above, the grating is formed by interference of SPPs with the incident pulse, and the period is thus expected to depend on the effective dielectric constant of the film surface. Using the above relation, values in the range of $1.0 < \mathrm{Re}(\eta) < 1.1$ are obtained. The implication of η being a function of the scan speed is actually reasonable, since the effective pulse number per unit area is expected to change the size of the nanoparticles and therefore affect the effective dielectric constant. For speed values outside the two regimes of grating formation, at speeds between 5 and 70 mm/s, randomly distributed nanoparticles beneath the titania surface with a small shape anisotropy (as shown in the inset FFT of Fig. III.4b) were obtained. For speeds of 200 mm/s or higher, randomly distributed nanoparticles were formed at the surface. As shown below in Figure III.6, for 200 mm/s scan speed, the nanoparticles grow and distribute randomly on the TiO_2 surface.

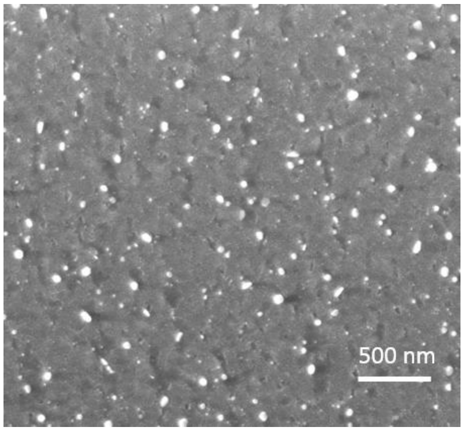

Figure III.6: Randomly distributed of Ag nanoparticles at scan speed of 200 mm/s

2.3 Temperature Rise in the Nanocomposite

The results in section 2.2, indicate that a change in the scan speed, and thus the effective number of pulses, leads to a temperature change inside the nanocomposite, thus, altering the final nanostructure. In order to study the maximum temperature increase experienced by the film during laser processing, the fabricated nanostructures were examined with a low power Raman spectrometer, in order to detect the possible formation of the crystalline phase in the TiO_2 matrix with a change in the scan speed. This allows an approximate estimation of the experienced temperature increase, since the formation of the anatase phase in TiO_2 is known to occur at a temperature of 350-400°C as also indicated in first chapter.[136,137]

The presence of the anatase phase can be identified in the Raman spectra by its characteristic E_g bands at 144 and 633 cm^{-1} and B_{1g} and A_{1g} bands at 409 and 515 cm^{-1}, respectively, also discussed in the chapter II.[87,100] Figure III.7 shows a series of spectra recorded in areas fabricated at different scan speeds. All bands were detected in the study, with an increasing amplitude for a decreasing scan speed. The low peak amplitude observed at higher speeds is characteristic of a low density of nanocrystals in the amorphous titania matrix. At the lowest scan speed of v = 1 mm/s, the Raman spectrum has the highest amplitude of the anatase phase peaks, revealing the presence of a higher density of the crystalline phase. The latter are actually mainly located in the grating grooves when the surface grating is formed, as reported in the previous article of Liu et al.[18] and are nearly inexistent at the highest speed (200 mm/s) where no grating occurs.

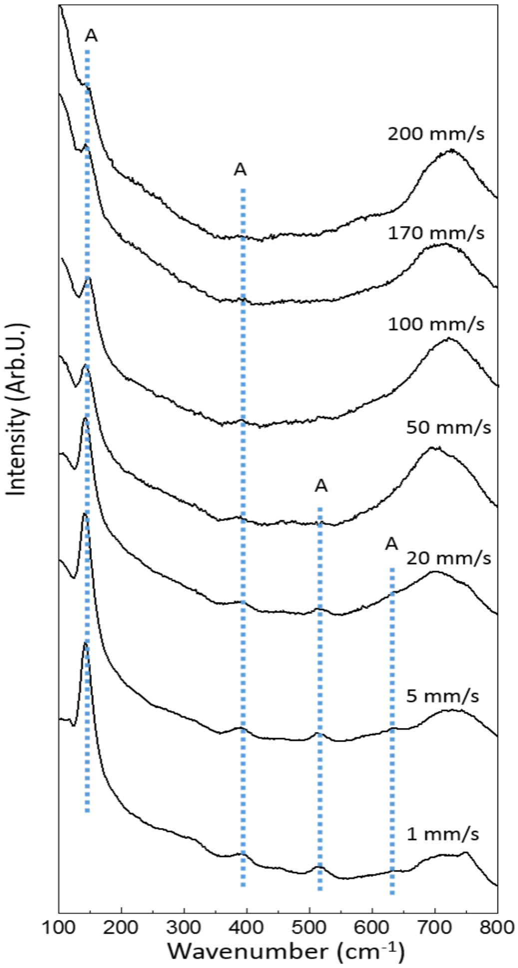

Figure III.7: Raman spectra for the different nanostructures obtained using different scan speeds, as indicated. 'A' denotes the bands corresponding to the crystalline anatase phase of titania.

As different phases have different dielectric functions, the partial crystallization and densification of the film (collapse of pores) may be a reason for the observed period changes with the scan speed, in both speed regimes. It is to be noted that while with fs lasers we just reach the temperature where we crystallized the matrix in its anatase phase, with cw lasers the temperature was high enough to get the rutile phase in the speed ranges of 1-30 mm/s at 488 nm laser wavelength for a fixed laser power as indicated in Liu's thesis.[74]

2.4 Optical Response in the Nanocomposite

In order to assess the optical response of the nanocomposites with the scan speed, the nanostructures were characterized using a Cary spectrophotometer. Figure III.8 shows the measured reflectance and transmittance spectra of the four different nanostructures shown in Fig. III.4. For each structure, spectra for both light polarizations were recorded, parallel and perpendicular to the laser polarization, in order to investigate the possible presence of anisotropic optical response. As a reference, the corresponding spectra of an infiltrated nanocomposite film before laser exposure is shown in Figure III.1, which shows a very weak absorption in the visible range.

At lowest speed (v = 1 mm/s), the features of all spectra are broad and little pronounced, with a maximum absorption of about 50 %. The most striking observation is the existence of a strong polarization anisotropy in R (reflectance), T (transmittance) and 1-R-T (losses, i.e. mainly absorption and some scattering), for instance the spectral shift in the loss peak amounts to almost 200 nm. As the scan speed is increased, the spectral features become more pronounced, while the anisotropy is reduced. At v = 20 mm/s, strong loss bands are observed in the visible spectral region, reaching a maximum of almost 75 %. In this case, the still present strong polarization anisotropy is most likely caused by the shape anisotropy of the silver nanoparticles (see FFT inset in Fig. III.4b), since there is no evidence of a nanoparticle grating. Such a strong dichroism due to a nanoparticle shape anisotropy with preferential orientation was also reported in other works on femtosecond laser irradiation of silver nanoparticles embedded in different dielectric matrices.[125,126,138,139] In the work of Stalmashonak et. al., the initial shape of the spherical silver nanoparticles were altered using low repetition rate (1 kHz) fs laser irradiation to lengthen or shorten the nanoparticles along the laser polarization direction (depending on the irradiation conditions), yielding optical dichroism in the material.[131] Similarly, Baraldi et. al.

showed polarization anisotropy of a near-coalescence single layer of Ag nanoparticles using fs laser irradiation, altering the shape, alignment and organization of the nanoparticles.[126]

At v = 100 mm/s and 170 mm/s, the peaks in absorption and reflectance, as well as the minimum in transmission, are further sharpened and the polarisation anisotropy is reduced. Moreover, additional spectral bands appear in the infrared region near 800 nm. These bands correspond to the probe light that is coupled into the film acting as a waveguide, leading to a lower reflection and transmission and to a higher absorption. Coupling is mediated by the surface grating. The fact that no such band is observed at 1 mm/s, although the structure also features a grating, suggests that the coupling efficiency of a surface grating is higher than that of an embedded grating. This additional band can be conveniently used to estimate the effective refractive index of the nanostructured film using the grating equation:

$$\eta = \sin(\theta_i) + \frac{\lambda_{Tmin}}{\Lambda} \qquad \text{(Eq. III.4)}$$

where θ_i is the incidence angle and λ_{Tmin} the wavelength at which transmission shows a minimum, which is close to the resonance wavelength, even though not exactly the same.

For v = 100 mm/s the grating structure has a period of 474 nm, and from the spectrum we obtain λ_{Tmin} = 760 nm, for θ_i = 6°. The calculation yields η = 1.71, which is an approximation of the effective index value for the guided mode in the nanostructured film. At 760 nm wavelength, the 474 nm period grating does not diffract light in free space, since

$$\left|\sin(\theta_i) \pm \frac{\lambda}{\Lambda}\right| > 1 \qquad \text{(Eq. III.5)}$$

for incidence angles smaller than -37°, depicting that the increased losses are mainly due to absorption. The dichroism observed in all structures is directly related to the laser polarization, either by determining a preferential direction of surface or guided mode coupling or by lengthening the nanoparticles along a certain direction. This strong dichroism observed in the processed samples (Fig. III.3 and III.8) can be exploited in a variety of applications for example for encoding and counterfeiting materials, as well as for smart decorative purposes.

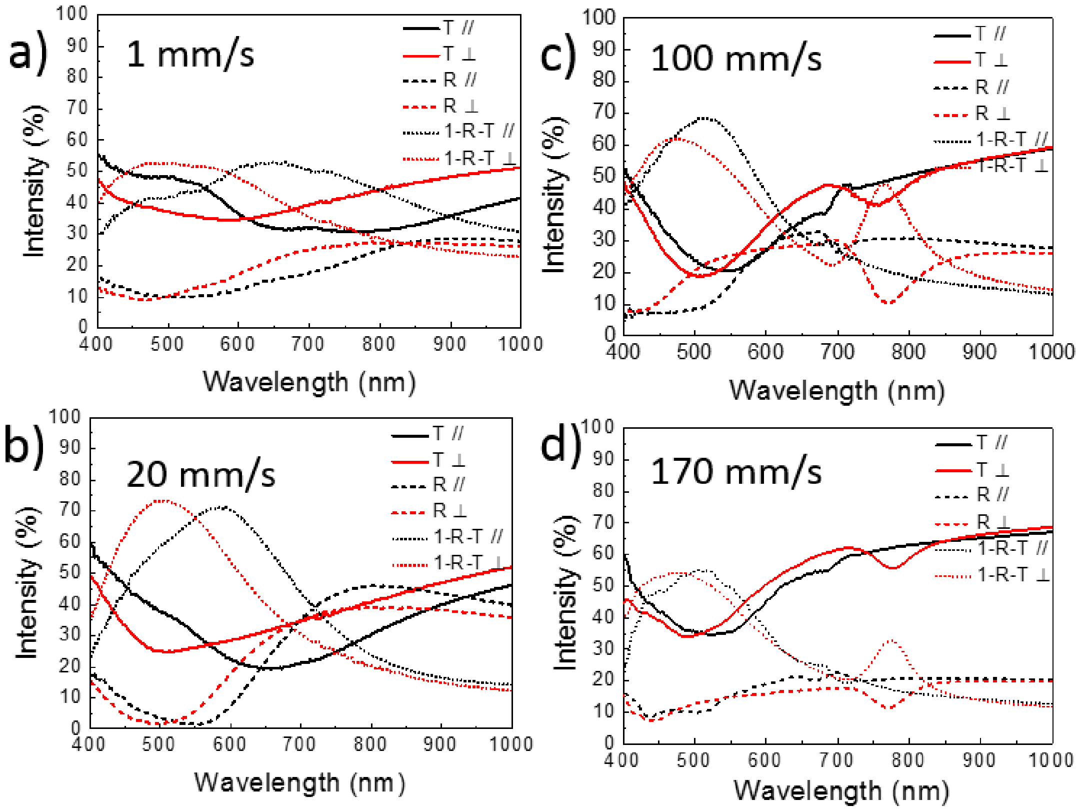

Figure III.8: Transmittance (T) and reflectance (R) spectra taken at 6° incidence angle for a) the initial Ag:TiO_2 nanocomposite films before laser irradiation and different scan speeds of b) 1 mm/s, c) 20 mm/s, d) 100 mm/s, and e) 170 mm/s. Losses including absorption and scattering were calculated as (1-R-T). ⊥ and ∥ refers to the probe polarization, respective to the laser polarization.

2.5 Elimination of Spectral Anisotropy by Structuring with Circular Polarized Laser Light

In the following section, it is demonstrated how fs-laser processing also allows the fabrication of nanostructures yielding an angle-insensitive colour perception. This can be easily performed by using circular instead of linear polarized light. Fig. III.9 displays the R, T and loss spectra of two representative nanocomposite films that were irradiated with a circular polarized laser beam, using scan speeds of 1 and 100 mm/s. It can be seen immediately that any signs of anisotropy disappeared when using circular polarized light, while comparing the spectra to those of the structures written with linear polarized light. Their shape seems to be similar to the mean value of the two spectra corresponding to the two polarization states of the anisotropic structures. To confirm this, the average of the experimental spectra for the two linear probe polarizations (Figure III.8a and III.8c) were calculated and displayed in Figure III.9c and III.9d for comparison.

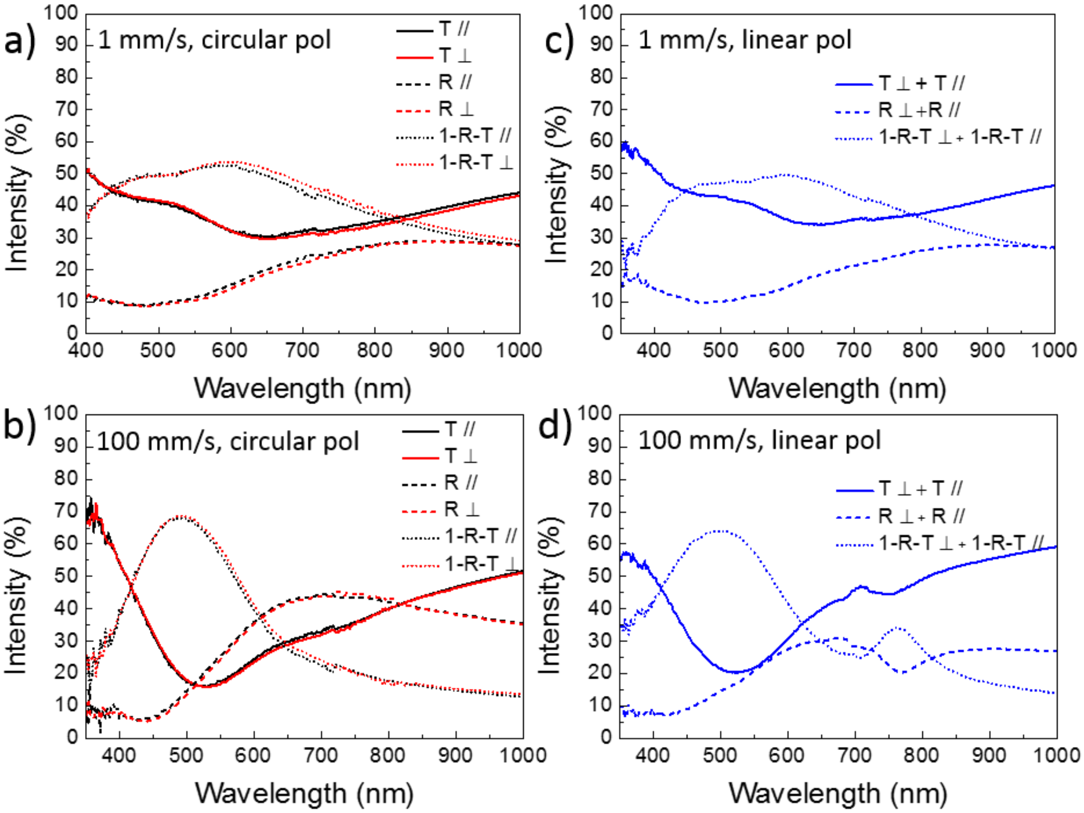

Figure III.9: Transmittance (T), reflectance (R) and loss (1-R-T) spectra for nanostructures fabricated with circular polarized laser light for two different scan speeds. a) 1 mm/s and b) 100 mm/s. For comparison, c) and d) show curves for linear polarized laser light, obtained by calculating the average value of the experimental ⊥ and ∥ curves from Fig. III.8a and III.8c. ⊥ and ∥ refers to the probe beam polarization, respective to the laser polarization. The spectra were taken at 6° incidence angle.

For v = 1 mm/s, the results are indeed equivalent, while for v = 100 mm/s, the resulting average curves are similar but show a significant deviation in the infrared region due to the existence of grating coupling and mode propagation for the structures fabricated with linear polarized laser light, and the absence of this behaviour for circular laser light. The general similarity of the spectral response for the two laser polarizations underlines its importance for applications and the usefulness of this approach, which allows to fabricate nanostructures with a similar spectral response and optional polarization anisotropy.

2.6 Imprinting Hybrid Structures

While the above results exploit a change of the scan speed to achieve spectral tuning of the laser-fabricated samples, a complementary strategy is applied to combine different nanostructures placed close together. New spectra can be synthesized in this way via linear combination of the spectra of the two individual nanostructures. The idea is implemented by means of interlacing nanostructures of two different types, each produced within single scan lines with an approximate width of about 23 μm. The particular hybrid nanostructure shown in Figure III.10 was fabricated by first writing a large array with a line spacing of 46 µm at a laser scan speed of 100 mm/s and subsequently writing a second array at 1 mm/s, which was laterally displaced by 23 μm in order to fill the gaps of the first array. This led to the formation of interlaced lines, as shown in Fig. III.10a, each with a different grating period (Λ_{EG} = 330 nm and Λ_{SG} = 480 nm) and orthogonal orientations.

The linear laser polarization was kept the same in both cases, aligned along the scan direction, as shown in the optical micrographs (Fig. III.10a). The fact, that the used line spacing was more than 20 times larger than for the homogeneous structures using a line separation of 2 μm, led to a strong decrease of the effective pulse number within a line. Thus, it was necessary to compensate for this effect by rescanning each line 20 times in order to accumulate an equivalent pulse number as for the homogenous areas. This method enabled the formation of adjacent embedded gratings (EG) and surface gratings (SG). Figs. III.10b-c shows the transmission spectra of the hybrid structure to light polarized perpendicular and parallel to the laser polarization direction, respectively. Since the adjacent gratings are narrow-spaced, the perceived transmission spectra of the hybrid structure are essentially the sum of the individual spectra of the two gratings obtained at 1 and 100 mm/s.

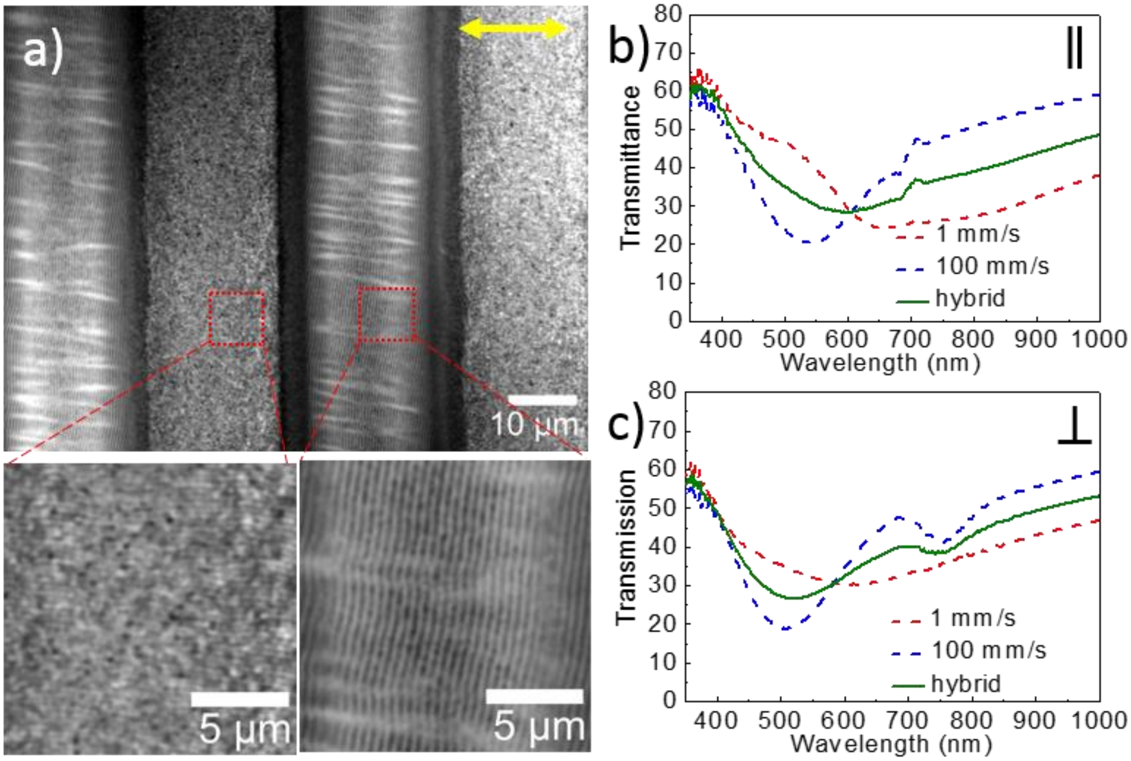

Figure III.10: Optical micrographs of a hybrid nanostructure composed of adjacent vertical scan lines, each containing a different type of nanograting. Magnified regions are shown below, the left corresponding to the EG (barely visible horizontal grating lines) and the SG (vertical grating lines). b) and c) Measured transmittance spectra of the hybrid nanostructure for both light polarizations (∥ and ⊥), compared to the corresponding spectra of areas written at single speeds, 1 and 100 mm/s.

Figure III.11 shows visible light diffraction caused by the embedded grating written at 1 mm/s (Figure III.11a) and by the surface gratings (LIPSS) written at 100 and 170 mm/s (Figure III.11b). The outlined squares are the ones discussed in this chapter for the scan speed study. Only the hybrid structure (HSt) diffracts in both viewing directions, i.e. in the direction along which the embedded grating at 1 mm/s can be seen (Figure III.11a2) and when the sample is rotated in its azimuthal plane by 90°, along which diffraction from LIPSS can be seen (Figure III.11b2). This strategy of interlacing different nanostructures enables the predictive design of new spectra based on the knowledge of the spectra of the two participating individual structures. This approach can be sophisticated by changing the relative weight of an individual structure through a deviation from a 1:1 interlacing ratio, towards 2:1 or 3:1. Likewise, more than two different nanostructures can participate in the design of a new spectrum. Such parametric study opens new ways for the fabrication of customized hybrid structures for a range of different applications.

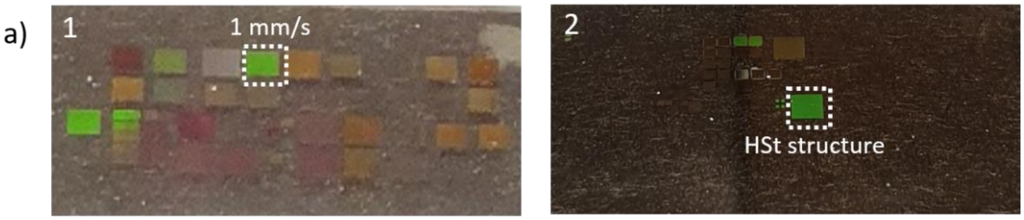

Diffraction from embedded grating

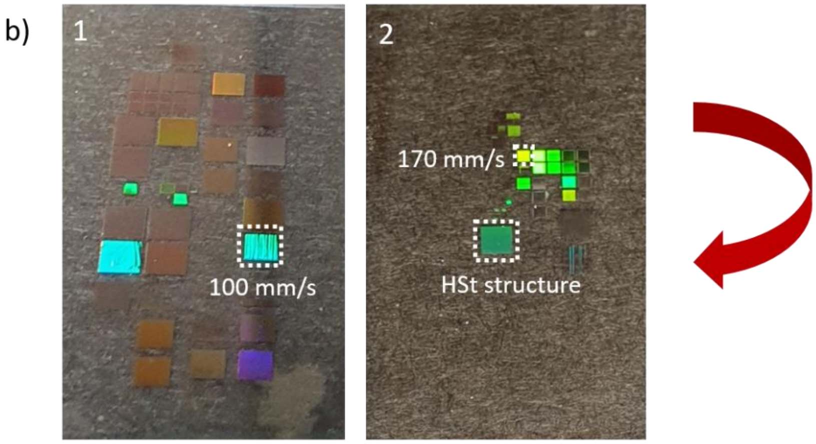

Diffraction from surface grating (LIPSS)

Figure III.11: Photographs of samples highlighting diffraction of white light by laser-written areas at different scan speeds corresponding to a) embedded gratings (EG) and hybrid gratings (HG) and b) surface gratings (SG) and hybrid gratings. The red arrow indicates that the sample has been rotated by 90º between (a) and (b).

3. Conclusions

This chapter demonstrates the fabrication of different silver nanocomposite structures using a facile fs laser scanning technique, triggering growth and self-organization of silver nanoparticles. By adjusting the scan speed, such nanocomposites can be selectively formed either at the surface or imbedded inside the film to form grating structures. Excitation of a surface mode in form of surface plasmon polaritons is possible due to the high density of small nanoparticles in the initial film and the transient effects induced by the ultrashort laser pulse. This way, laser induced periodic surface structures are formed at higher scan speeds, featuring silver nanoparticles along the grating lines. At lower speeds, nanoparticle organization is governed by the excitation of a guided mode inside the film and larger nanoparticles are grown, enabled by a higher temperature rise. Raman spectroscopy studies reveal a partial crystallization of the titania matrix in its anatase phase, which indicates a maximum temperature increase above 400°C around Ag nanoparticles, and demonstrates an increase in the nanocrystal content when decreasing the scan speed.

The induced growth and self-organization processes lead to a marked colour change of the nanostructured composite thin film, which strongly depends on the scan speed. Moreover, strong dichroism in reflection and transmission is induced by using linear polarized laser pulses. Dichroism is found to be caused by the presence of the different grating structures for high and low scan speeds, as well as by the shape anisotropy of the nanoparticles induced at moderate scan speeds. The films with dichroism show iridescent properties that can be useful for encoding of information in counterfeiting applications. In addition, it is demonstrated that films showing angle-insensitive colour perception can be also prepared by using circularly polarized laser light for processing. The flexibility of this laser-based marking technology also allows the fabrication of hybrid nanostructures composed of different adjacent nanostructure types, interlaced to cover large areas. Such generation and design of multiple nanostructures with ultrashort pulsed lasers offers high control over the optical response of nanocomposite systems, providing access to a broad range of nanostructures with a tailored optical response suitable for eminent applications in security for hidden images as illustrated in the next chapter, image multiplexing that will be illustrated in chapter V, photocatalysis, photovoltaics and smart visual effects.

CHAPTER IV

DIFFRACTIVE MULTIPLE IMAGES HIDING USING FS LASERS ON NANOCOMPOSITE FILMS

After discussing about, how we can tailor nanocomposite structures using lasers, arising due to the growth and self-organization process of nanoparticles inside the titania matrix in the previous chapter, it is important to focus upon the applicative part for such laser process technology. This chapter focuses on, the first application of multiple hidden images produced by such fs laser processes on plastic substrates, a technology developed at Laboratoire Hubert Curien in collaboration with HID Global CID.

1. Introduction

Encoded printed images that allow optical recognition of different patterns under various conditions of observation have sparked many developments for applications to entertainment, design, data storage or security. Different approaches can be found in the literature; they are suited for different kinds of materials, and require sometimes additional devices to reveal different images. Moiré methods allow revealing latent images when superposing a master screen to a printed image. [140,141,142] Colour separation schemes for reflective and diffusive viewing conditions of inks printed on metallic surfaces have been developed to display dual images.[143] Changeable Laser Image (CLI) and multiple laser image (MLI) systems display with angular selectivity interlaced images printed underneath a micro-lens array.[144] Moreover, holograms have been used since decades for security applications, providing angle-dependent or polarization-controlled full colour dual images.[145] More recently, polarization driven vectorial meta-holograms robust against incidence angles and wavelengths have been fabricated by EBL using couples of orthogonal plasmonic nanorods.[146] Another approach based on spin and wavelength encoding of metasurfaces has been proposed to encode up to 63 6-bit colour holograms resulting from combinations of 6 independent monochromatic holograms.[147] Plasmonic anisotropic nanopatterns produced by EBL have also been used to draw high resolution polarization-controlled full-colour dual images observable with white light.[148,149] EBL is however an expensive technology compared to the aforementioned ones and mainly produces small images observable by optical microscopy. On plasmonic surfaces, nanovolcanoes created individually by a tightly focused laser beam have been controlled to produce angular encryption of full-colour images.[150]

Versatile ink-free printing technologies based on laser scanning techniques have several merits. They provide a simple implementation for drawing complex patterns on non-necessarily planar surfaces, they can reach better spatial resolution than ink-based printing techniques, and are cost-effective when compared with printing technologies involving electron beam lithography. Lasers have already been used to engrave,[151] oxidize[152] or change the refractive index[153] of materials, leading to several marking applications. They can also trigger self-organization mechanisms that create ripples on surfaces, also known as LIPSS as discussed in previous chapter.[127] LIPSS have been produced by cw or pulsed lasers on all kinds of materials i.e. metal,[135] semiconductor,[154] dielectric [155] and few nanocomposites.[18] They can give rise to highly dispersive diffraction gratings for visible light provided that their period is close to visible wavelengths. This led to printing of diffractive coloured images on metallic surfaces.[156] However, while demonstrated on different polymer substrates with both nanosecond (ns) and fs laser pulses,[157,158] no LIPSS were produced on such materials with periods close to visible wavelengths and high dielectric contrast that could provide high dispersion for visible light with high diffraction yields.

This chapter shows that highly dispersive self-organized diffraction gratings can be induced on Ag:TiO_2 nanocomposite films deposited on commercial polycarbonate sheets and can be used to encode three different grey-scale images revealed in three angular directions. The chapter addresses the issue of laser-induced thermal effects that are serious limitations for plastics processing and provides conditions optimizing the nanoparticle growth and self-organization in the nanocomposite film while preventing the film spallation and the substrate damage. Employing a continuous control of laser polarization orientation, the grating orientation is modulated to provide a grey-scale variation of the diffracted intensity in given observation directions. The three image frames are interlaced to create a single encoded image whose appearance is fully homogeneous in transmission and reflection on plastic substrate. To compare the resolution of a similar encoded image on plastic, a glass substrate with such nanocomposites was also used, which can withstand higher temperatures and hence provide a better resolution with lower pixel size inscription. Images were produced to be observed by eye and the question of spatial resolution of such a writing process is addressed on soft and hard substrates. It is to be noted that the laser processing used for the applicative part that are discussed in this chapter and the following chapter were performed using a Pharos laser system at Laboratoire Hubert Curien, for which the detailed are given below in the section Laser Processing.

1.1 Thin-Film Fabrication

As the hidden images were printed on plastic substrate, the elaboration process used in the previous chapter for coating on glass substrates is modified to suit it for coating on flexible plastic. The plastic substrate is a commercial 375 µm thick polycarbonate sheet with a scratch-resistant coating. The sol consists of chemicals in similar ratios, as detailed in the previous chapter, to obtain TiO_2 amorphous sol. Prior, to any coating, the substrates are cleaned with ethanol and De-ionized water (DI) under sonication and dried with nitrogen. The substrate which was fixed on a square rigid glass (as to avoid any vibrations or deformations) was spin-coated at 1500 rpm/30s with the TiO_2 sol and baked at 110°C for 2 hours for stabilization. Further, the polymerization of TiO_2 and release of porosity is done differently (as compared to heating on glass substrates), in two steps. Primarily, the film is submitted to UV illumination (254 nm, 6 mW/cm^2) for 6 hours to decompose the complex of TTIP-AcAc followed by soaking the films in

EtOH under sonication to extract the surfactant.[71] The film porosity is further filled with Ag ions, by soaking the film in a silver nitrate solution (1.5 M). The ions are partly converted into silver atoms and small silver nanoparticles under UV light (254 nm, 6 mW/cm², 10 min), as discussed previously. The films are transparent but slightly absorbent in the visible range due to the localized surface plasmon resonance of the small Ag nanoparticles initially present in the nanocomposite film. It has to be noted that the photochromic behaviour on films deposited on plastic was not similar to that deposited on glass due to the change in the thickness. In this case, thickness plays an important role in photochromic behaviour, and it was observed a thicker film of more than 200 nm is less photochromic.

1.2 Laser Setup

The laser system comprises of a single unit integrated Pharos laser with a pulse duration of 200 fs at a fundamental wavelength of 1030 nm and at 100 kHz repetition rate, which can be tuned. Frequency doubling to get a wavelength of 515 nm is achieved with a BBO crystal. This wavelength is used to excite the localized surface plasmon resonance of Ag nanoparticles in the composite films and does not directly affect the TiO_2 matrix or the substrate at the used fluences. The pulsed energy of the laser is tuned with a half-wave plate followed by a polarizer, which are followed by another half-wave plate for controlling the laser polarization with the help of an external LABVIEW software (Figure IV.1). The laser is then focused on the sample with a 10 cm focal length lens where the scanning is being implemented with motorized translation stages (PI Micos) in two different directions. With such a system we are limited to scan speed between 0.01 to 10 mm/s, which was not the case while using the setup at CSIC as detailed in the previous chapter that uses a galvanometric scanning head to reach higher speeds. A schematic diagram of the laser system is shown in Figure IV.1. In the present case, we work with a low repletion rate of less than 50 kHz preventing the damage while working on the plastic substrates. A parametric study is performed to investigate different regimes followed by using the foremost parameters for multiple images hiding.

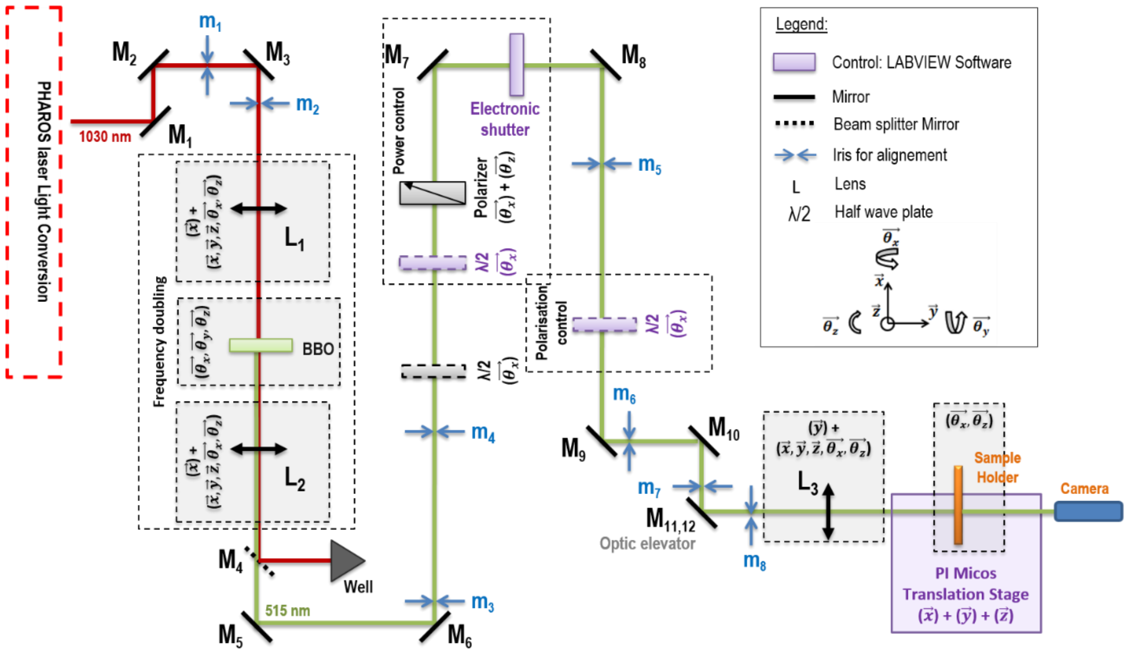

Figure IV.1: A schematic diagram showing the laser setup developed at Laboratoire Hubert Curien for low repetition rate laser writing. The inset shows the legend used in the illustrative diagram.

2. Parametric Study

Different regimes that can be found by tuning the scan speed and the laser fluence at a fixed repetition rate and spacing between laser lines are investigated in this section. As substrate damage (burning/deformation of plastic) limits the parameter range when working on plastic, the results obtained on polycarbonate substrate are reported here. On such substrates, the repetition rate could not exceed 50 kHz to identify regimes where self-organized gratings can appear without sample deformation. At higher repetition rates the thermal accumulation appeared to be too strong.

In order not to slow down too much the scan speeds in which self-organized gratings could be produced, the repetition rate was not decreased below 25 kHz. At a fluence of 124 mJ/cm^2 (Figure IV.3c), and slow scan speed of 1.8 mm/s, few Ag nanoparticles in the form of nanorods are observed on the surface where no grating is formed, but most of Ag nanoparticles are embedded in the film as attested by the irregular contrast of the SEM image of the surface that is characteristic of the presence of a high density of Ag nanoparticles (brighter contrast) just below the film surface. Due to the low contrast and the blurred outline of the nanoparticles, SEM images are not suitable to properly measure the size distribution and the nanoparticle density. We can however estimate that nanoparticle sizes between 10 and 40 nm are present in the film. Such a film does not delaminate from the substrate.

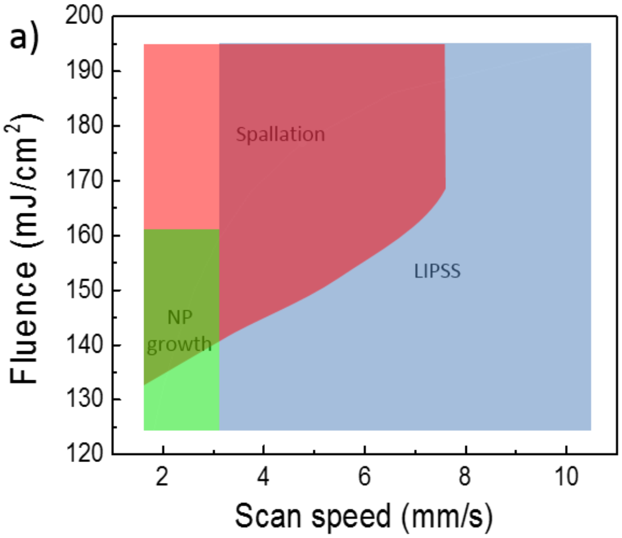

Figure IV.2: Different regimes of laser-induced changes in the film nanostructure and morphology, identified with varying scan speed and laser fluence for a fixed spacing between lines of 20 µm and repetition rate at 25 kHz.

When increasing the scan speed to 3.08 mm/s at the same fluence, Ag nanoparticles are still few on the film surface and they have a rather circular shape; a high density of Ag nanoparticles is still present below the surface with a size that does not exceed 25 nm, as estimated from SEM images. A slight periodic contrast is now observed on the SEM images corresponding to the presence of LIPSS with a low amplitude. The film does not delaminate. At a scan speed of 10.5 mm/s, the nanoparticles on the film surface are rare and with a circular shape. Embedded nanoparticles have a lower size than in the previous case and are difficult to identify by SEM. Surface gratings can be distinguished but with less contrast than at the previous speed. They have been highlighted by white double dash lines when they exist. At a higher fluence of 159 mJ/cm^2 (Figure IV.3b), spallation (shown in inset when imaging samples at a lower magnification) occurs at 1.8 mm/s and LIPSS with a better contrast as previously start emerging when increasing the scan speed. Most of the nanoparticles are embedded and difficult to identify from SEM. At the fluence of 195 mJ/cm^2 (Figure IV.3a), the spallation is present over a larger speed range and more contrasted LIPSS occur at the highest scan speed of 10.5 mm/s.

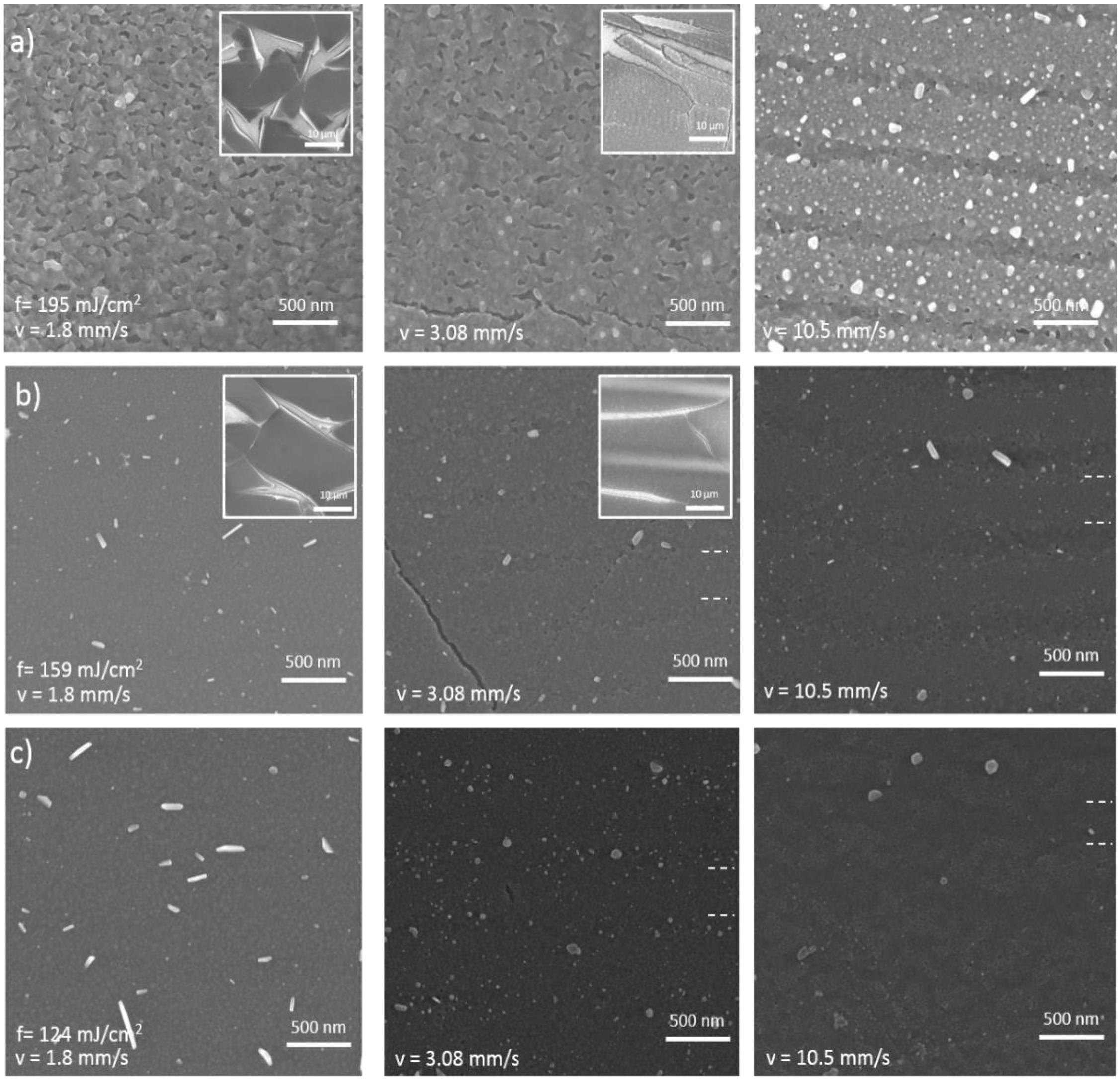

Figure IV.3: SEM images showing surface topography as illustrated in Figure II parametric range (25 kHz,) for three different laser fluences of a) 124 mJ/cm^2, b) 159 mJ/cm^2 and 195 mJ/cm^2 (SEM image in each row corresponds to the similar power as depicted) and the scan speed for 1.8, 3.08 and 10.5 mm/s, mentioned here for each column are similar for each fluence respectively.

Further, when submitted to high temperatures, TiO_2 partially crystallizes as also discussed in the previous chapter and the film mesoporosity tends to collapse creating high tensile stresses. The latter create cracks, which cause peeling of the film off the polycarbonate substrate. When working at a higher repetition rate of 50 kHz, similar regimes can be obtained in slightly different parameter ranges. Interestingly, higher diffraction efficiencies are reached at 50 kHz compared to 25 kHz, in the parameter range where LIPSS form while preserving the film integrity. This relative higher repetition rate is thus of greater interest for the targeted application and is used in the following, using a fluence of 133 mJ/cm², a speed of 8.74 mm/s, which corresponds to 300 pulses per unit area, and spacing between lines of 40 µm. On glass substrate the best results were obtained at 100 kHz and are compared further to the best results obtained on plastic.

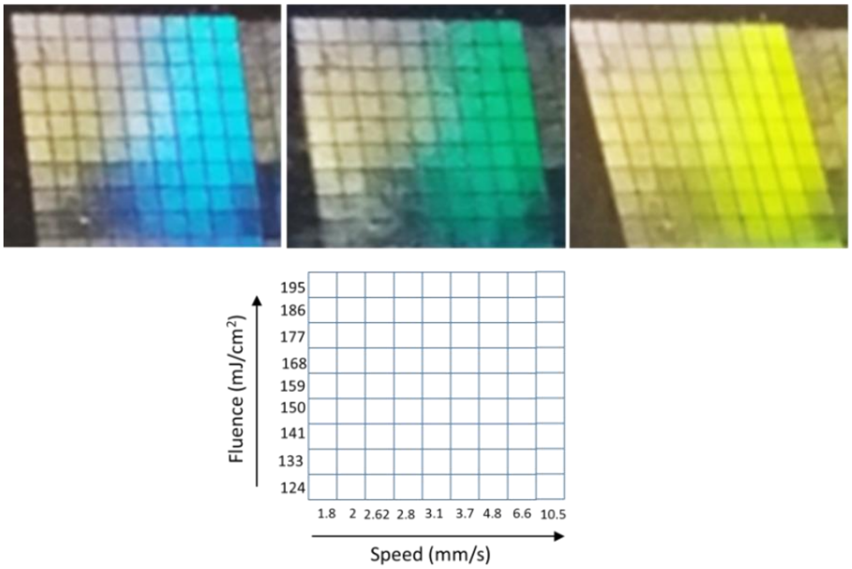

Figure IV.4: Diffraction by LIPSS patterns on plastic substrate. Photographs of a sample taken under white light and different angles of observation to qualitatively highlight the variations in the diffraction efficiency with the scan speed and laser fluence.

The presence of LIPSS on the sample surface was better identified when observing diffraction of white light on the sample. Figure IV.4 shows photographs of a sample, where squares were drawn with varying scan speeds and fluences, taken under right conditions of observation and illumination to catch optical diffraction of blue, green and yellow radiations. The diffraction efficiency qualitatively decreases when decreasing the speed and the fluence, except for the two lowest fluences where the maximum speed also leads to low diffraction. Such information together with SEM observations was used to draw the sketch of Figure IV.1.

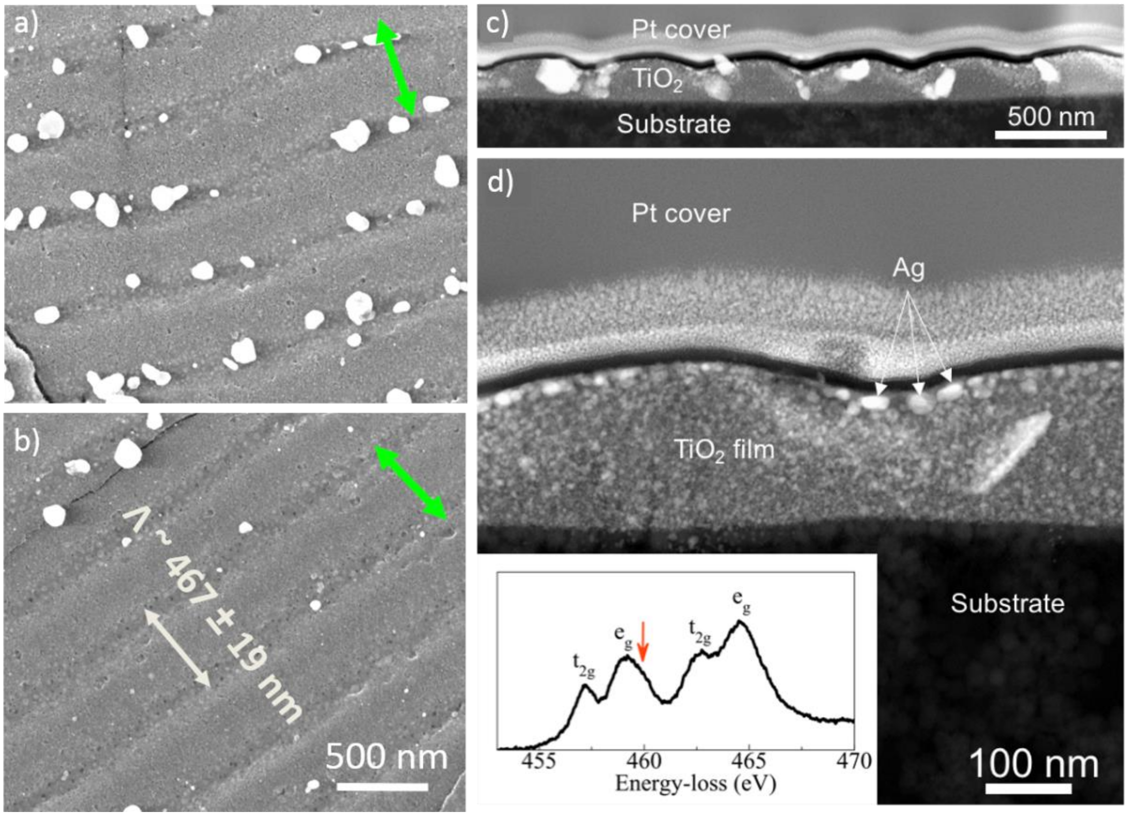

Figure IV.5: a-b) SEM images at two different locations, showing LIPSS with a period of 495 ± 15 nm and different orientations perpendicular to the laser polarization (green double sided arrows). c) HAADF-STEM cross-section view of the LIPSS. Note that the big Ag particles (yellow arrows) appearing on the film cross section were not stable under electron beam during STEM characterizations, contrary to the smaller ones d) HAADF-STEM enlarged view of the sample cross-section, with Ag nanoparticles embedded in the grooves of the LIPSS. Inset: EELS Ti $L_{2,3}$ near-edge structures obtained in the region below the LIPSS groove. The red arrow highlights the shoulder at the higher-energy side of the e_g peak of the L_3 line, which is characteristic of the anatase TiO_2 phase.[175,176] The low amplitude of this shoulder compared to anatase spectra of the literature[177] is attributed to the partial crystallization of the TiO_2 as well as the instrumental resolution (~1 eV).

The self-organized gratings induced on the Ag:TiO_2 film deposited on plastic were characterized by electron microscopy. Figure IV.5a-b shows SEM images of the sample surface at two different locations, where the laser polarization (green double-sided arrow) has been rotated. The grating period remains the same, however its orientation follows the polarization rotation, being perpendicular to the latter. While Ag is still essentially in the film, large particles up to 190 nm in size grow on the sample surface mainly along the grating grooves.

A cross-sectional view of the LIPSS (Figure IV.5c-d), observed by high angle annular dark field HAADF-STEM, shows that the small (<40 nm) Ag nanoparticles (white in Figure IV.5c, d) embedded in the film, have preferentially grown within the grooves of the LIPSS. It is to be noted that the big Ag particles appearing on the film cross section did not grow inside the film but have been shifted from the top surface to the side of the lamella during focused ion beam (FIB) preparation. Electron energy-loss spectroscopy (EELS) experiments were carried out in a FEI Titan ETEM G2 80-300 instrument, operated at 300 kV. EELS measurements recorded in the region below the grating grooves (inset of Figure IV.5d) show a partial crystallization of TiO_2 in its anatase phase. The latter most probably slightly changed the appearance of the film. Indeed, the big Ag particles appearing on the film cross section were not stable under electron beam during STEM characterizations, contrary to the smaller ones. They are thus not expected to have grown inside the film but rather seem to have been shifted from the top surface to the side of the lamella during the preparation by focused ion beam, (FIB-FEI Helios 600i FIB instrument). Such big particles, if they had been embedded in the film, would have been visible with blurred outlines and low contrast, contrary to what was observed on all SEM images (Fig. IV.5a-b). Such a local growth of Ag and anatase nanocrystals creates a periodic modulation of the film effective refractive index, which reinforces the diffraction efficiency of the surface periodic structure. HAADF-STEM images in Figure IV.5c-d also confirm the perfect integrity of the plastic substrate below the Ag:TiO_2 film after the laser irradiation.

The formation of LIPSS as also discussed in the previous chapter in detail is governed by self-enhanced interferences between the incident wave and a surface plasmon polariton propagating along the material surface, which sets their period at $\boldsymbol{\Lambda} = \frac{\boldsymbol{\lambda}}{\mathbf{Re}(\boldsymbol{\eta})}$ for a laser beam under normal incidence; λ being the laser wavelength and Re(η) the real part of the effective refractive index of the surface plasmon polariton.[18] In the present case (Figure IV.5), the grating period is 495 nm ± 15 nm, which leads to an effective refractive index close to 1; a value usually reported for surface plasmon polaritons on metal surfaces as discussed in previous chapters.[133] The composite film is non-metallic, however the n-type semiconductor TiO_2 matrix loaded with silver nanoparticles can transiently adopt a metal-like behavior and support the excitation of a surface plasmon polariton at the film/air interface. Indeed, during a few hundreds of fs at each laser pulse, hot electrons excited through the localized surface plasmon resonance of the numerous small Ag nanoparticles initially present in the film can transfer to, and accumulate in the TiO_2 conduction band,[159,160,161] hence modifying the nature of the film.

During the first laser pulses, the surface plasmon polariton is only excited through scattering at heterogeneities and is no more than a perturbation signal. While its propagation direction is not precisely defined, the surface plasmon polariton interferes with the incident wave, creating a periodic modulation of the deposited energy. The resulting formation of a grating then acts as a positive feedback loop that enhances the excitation of the plasmon polariton at the origin of the modulation. As a plasmon polariton can only be a TM wave, the positive feedback only works for grating lines that are perpendicular to the incident polarization. The positive feedback thus triggers the self-organization process for a specific orientation of the interference pattern, and the surface gratings form pulse after pulse perpendicular to the incident laser polarization. [72,152] Here, we use the control of the grating orientation to encode grey-level images that can be observed in diffraction. Such a methodology is used to print three interlaced images, whose 256 grey-levels were converted into grating orientations ranging over 15° and starting for each image at 0°, 60° and 120° respectively (Figure IV.6a).

When illuminating a grating of period Λ with a collimated beam under the incidence angle θ_i in the plane perpendicular to the grating lines, diffraction takes place in the plane of incidence under the angle θ_p defined by the grating equation:

$$sin(\theta_p) = -sin(\theta_i) + p\frac{\lambda}{\Lambda}. \qquad \text{(Eq. IV.1)}$$

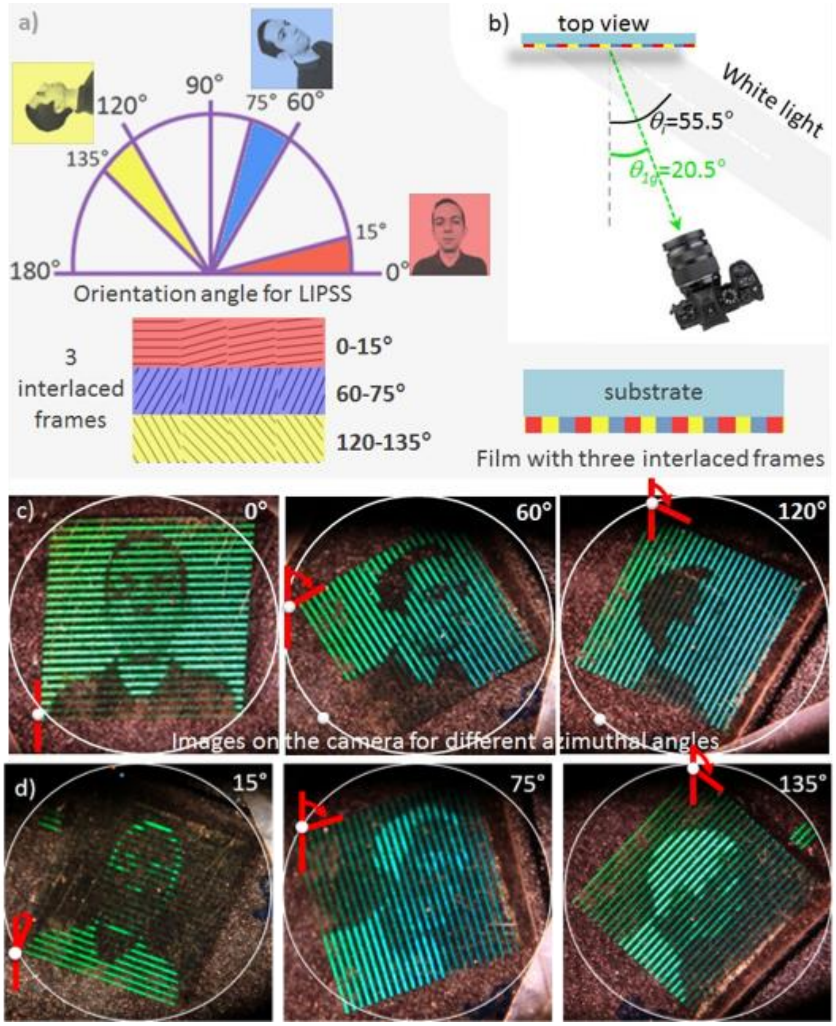

Figure IV.6: a) Angular ranges of LIPSS used to encode the 256 grey-levels of each image. The three raster images have been interlaced and printed on a 1.18 cm^2 surface. b) Sketch of the setup used for taking photographs of the sample. This top view sketch especially shows the incidence angle $\boldsymbol{\theta_i}$ of the white light collimated beam and the angle $\boldsymbol{\theta_{1g}}$ of the first diffraction order in the plane of incidence for a green radiation at 537 nm wavelength. c) Photographs of the sample printed on polycarbonate recorded for three different azimuthal angles obtained by rotating the sample in its plane. The three different images appear at 0°, 60° and 120°, respectively and their d) negative images at 15°, 75° and 135° angles.

When rotating the grating in its plane, i.e. introducing an azimuthal angle between the plane of incidence and the perpendicular to the grating lines, conical diffraction occurs and the diffracted orders do not belong anymore to the plane of incidence. So, continuously varying the grating orientation in an angular range from 0° to 15° allows tuning the intensity of diffracted light that can be captured by a camera located in the plane of incidence from a maximum value to zero. Such encoding of images, performed with laser parameters that lead to a grating period of 495 ± 15 nm (see Figure IV.5), allows to observe green (around 537 nm) images in the plane of incidence at the angle $\boldsymbol{\theta_{1g}} = \mathbf{20.5}^\circ$ of the first diffracted order, when illuminating the sample with a collimated white beam under an incidence angle $\boldsymbol{\theta_{i}} = \mathbf{55.5}^\circ$ (Figure IV.6b). Furthermore, when rotating the sample in its plane with an azimuthal angle varying from 0° to 120°, the printed image displays successively the three different pictures shown in Figure IV.6c. Figures IV.6d shows the negative images of the ones shown in Figure IV.6c that are obtained at angles 15°, 75°, and 135°, respectively, and where the colour of the diffracted images can be changed by varying the angle of observation in the incidence plane. The low grating period actually ensures a high angular dispersion, and well separated colours.

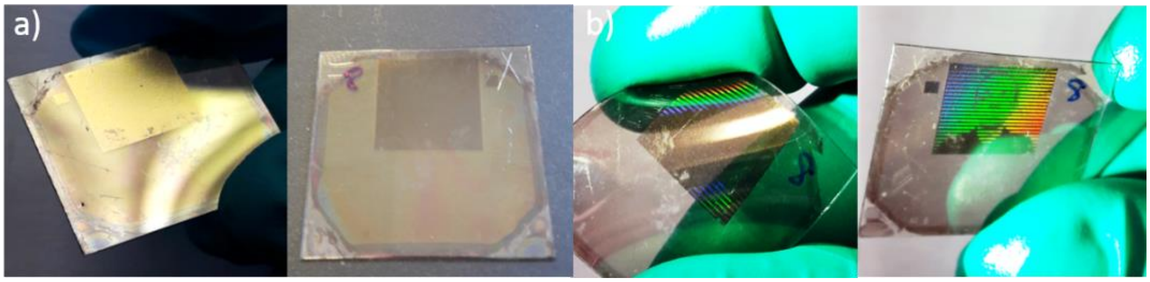

Figure IV.7: Photographs taken with a smartphone under ceiling lighting illustrating the reflectivity and the flexibility of the samples fabricated on flexible plastic substrate.

Moreover, all images being printed with the same fluence, scanning speed, spacing between laser lines, and repetition rate (only the polarization angle is tuned), the statistical properties of the laser-induced nanostructures are the same everywhere on the printed square, except the grating orientation. As a result, the sample appears fully homogeneous in reflection (Figures IV.7a) and transmission, hiding the three images. The photographs in Figure IV.7b also show the flexibility of the polycarbonate substrate, and the good adhesion of the printed nanocomposite film. The images were printed on such substrate with a pixel size of 160 µm consisting of four laser lines separated by a distance of 40 µm, as illustrated in Figure IV.8. The pixel size here on plastic was chosen to limit thermal effects that tend to damage the plastic substrate on the pixel edges.

Drawing images pixel by pixel using a laser scanning process, is made with an home-made Labview software that stops the translation stage between each pixel to let the time to the motorized rotation stage controlling the half-wave plate to reach the targeted laser polarization. During this waiting time the accumulation of laser pulses is much more important than what is expected inside the laser line and leads to a film damage on the plastic substrate, which is not really perceptible when working on a glass substrate. Each laser line is then affected by dark points at its ends that do not diffract light, as shown in Figure IV.8. This effect forces to increase the laser line length to 160 µm to get a significant diffracting length. In order to maintain square pixels, four lines 40 µm apart from each other were used for each pixel.

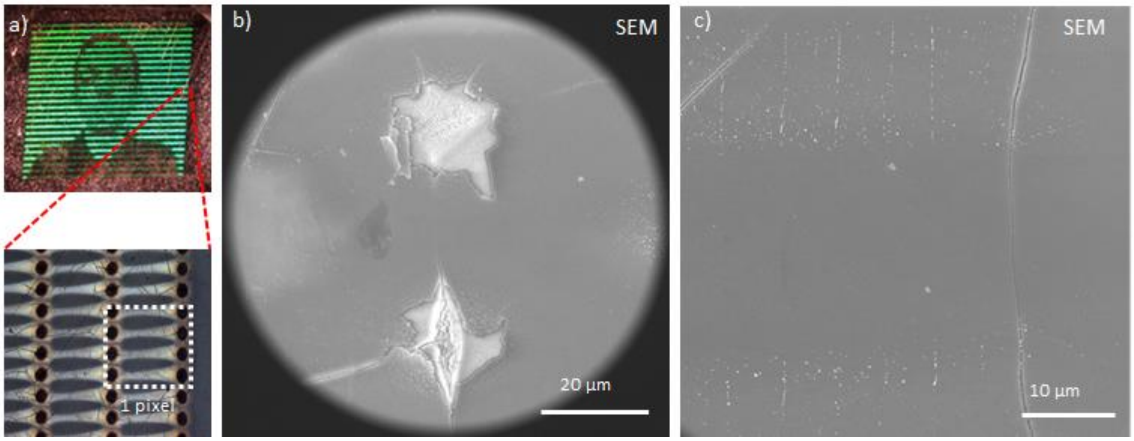

Figure IV.8: An illustration of the pixelated technology. a) Diffraction image of human portrait on plastic substrate with an optical zoomed image showing a pixel. SEM images, showing a) two dots, representing starting points of the laser lines inside the pixel, b) a zoomed image showing separation for two laser lines inside a pixel, with LIPSS.

An improvement in the image resolution could be done by modifying the Labview software and the setup itself. In order to work at the highest possible resolution, the laser drawing could be done dot by dot by controlling the number of pulses per dot rather than the scan speed, but this would require adding a pulse picker to the setup. In such a case, the resolution would be defined by the beam size on the sample surface, which could be decreased to few micrometers in order to optimize the resolution. The limit would then be the minimum size required to observe the formation of LIPSS. One has however to note that LIPSS formed along lines are usually more regular than LIPSS formed in dots. Further, the diffraction efficiency of each dot is directly correlated to the regularity of the grating. Accordingly, optimizing the writing process in terms of diffraction efficiency may be less efficient with a dot matrix printing.

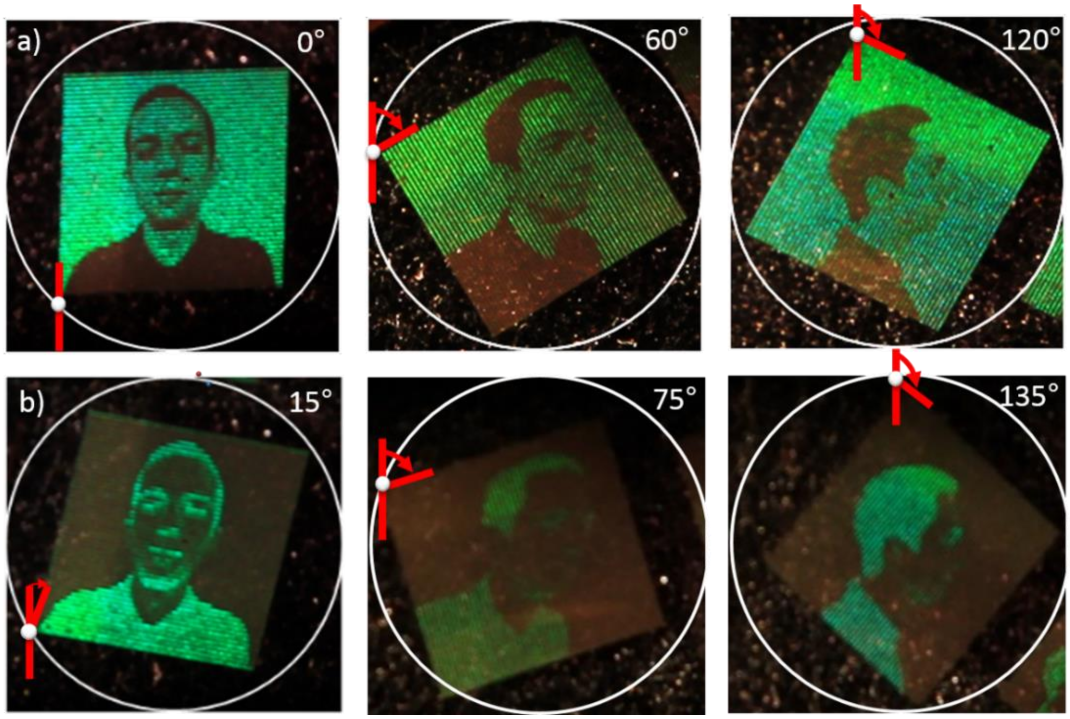

Figure IV.9: Interlaced diffractive images with same human portrait as in Figure V and a better resolution of 40 µm. Azimuthal angles a) 0°,60° and 120° displays the three positive images while their respective negative images are shown in b) at 15°, 75° and 135° angles.

Moreover, a better resolution can be achieved using same laser parameters but with different pixel size on glass substrate coated with mesoporous titania (films elaborated in Chapter III). A four time less, pixel size of 40 µm consisting of one laser line was used on nanocomposite films coated on glass substrate. Higher resolution images were printed with a higher printing resolution (Figure IV.9a-b). On both kinds of substrates, prints are stable over time for years (no change over the last two years was observed).

A second illustration of multiple image hiding on glass substrate is shown above where, Figure IV.10a shows a sketch of the setup used to image in the plane of incidence the different interlaced raster pictures printed in a single image.

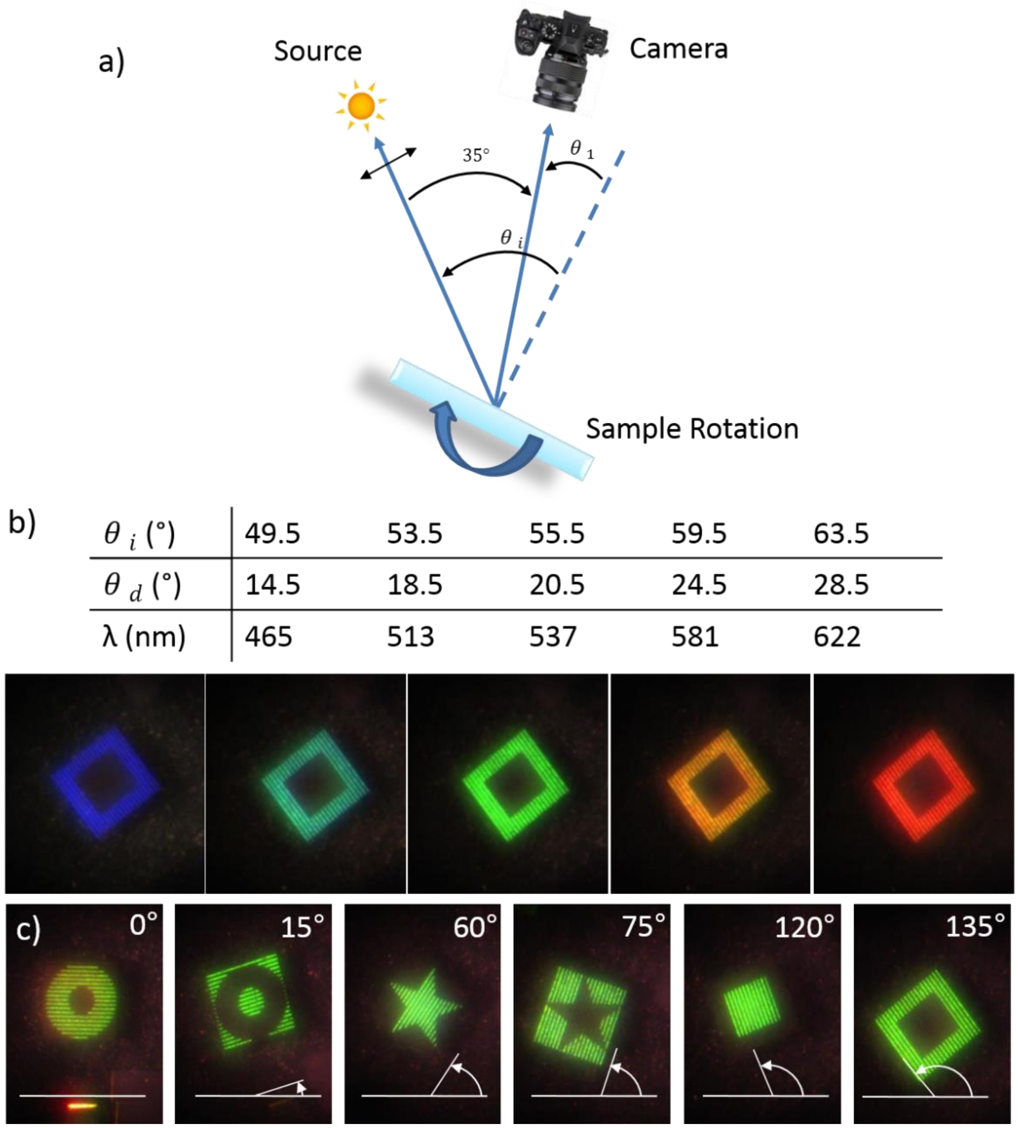

θ_i (°)	49.5	53.5	55.5	59.5	63.5
θ_d (°)	14.5	18.5	20.5	24.5	28.5
λ (nm)	465	513	537	581	622

Figure IV.10: Setup for taking pictures b) A tabulated values for θ_i, $\theta_d$and respective λ as calculated using equation 1 and 2, followed by images taken for different diffraction angles c) Multi-images illustrated at azimuthal angles of 0°, 60° and 120° revealing images of doughnut, star and a square with their respective negative images at 15°, 75° and 135° angles with angle of incidence and diffraction fixed at 55.5° and 20.5°.

Here, the angle between the light source and the camera is fixed at 35°. A rotation of the sample changes both the incidence angle θ_i and the angle θ_1 of the first diffracted order imaged on the camera. These angles are linked as follows:

$$\theta_1 = \theta_i - 35° \quad \text{(Eq. IV.2)}$$

Also knowing the period of the self-organized grating (Λ = 495 nm), one can deduce the wavelength at which the image is recorded on the camera. It is given by the grating equation according to equation IV.3:

$$\lambda = \Lambda\ (sin\ \theta_i + sin\ \theta_1) \tag{Eq. IV.3}$$

Figure IV.10b shows five images recorded at different angles of incidence with the corresponding diffraction angles and wavelengths. In Figure IV.10c, we show the three interlaced images and their negative images recorded for a fixed angle of incidence of 55.5° when rotating the sample in its plane, i.e. when varying the azimuthal angle from 0° to 135

3. Conclusions

In this chapter, a versatile ink-free printing of interlaced diffractive images on polycarbonate substrates is demonstrated, which do not withstand high temperatures using ultrashort-pulsed laser. This versatile laser scanning printing technology is enabled by the generation of self-organized surface and refractive index gratings in a nanocomposite $Ag:TiO_2$ film deposited on the plastic substrate. The choice of such a coating ensures the use of low laser fluences to trigger self-organization without damaging the substrate, and provides a high permittivity contrast for an efficient diffraction. This work demonstrates the parameter range in which such self-organized patterns can be obtained on plastic sample without any damage. The technology is suitable not only for plastics but more generally for transparent materials. The easy control of the grating orientation by the laser polarization is used to print grey-level images that can be observed by eye in specific angular directions, and that are completely hidden in reflection and transmission observation conditions. The smart printing of polarization-encoded interlaced diffraction images demonstrates the printing of three full scale hidden images. Such a technology can pave the way for industrial applications in security, packaging and design. Such results, are accompanied with an introduction to multiplexing of images with lasers in the next chapter; a second application with lasers on nanocomposite films of $Ag:TiO_2$. The technology used in the two applications are different, which makes them unique.

CHAPTER V

IMAGE MULTIPLEXING

The last chapter of the thesis deals with the second application arising from laser nanostructuring of the Ag:TiO_2 nanocomposite thin films. Such thin films are fabricated using the same methodology than the one illustrated in Chapter III, but on flexible glass substrates. The idea of this technology is to encode different information in the same pixel. Up to three images are encoded in a single one, printed in a single frame using the laser processing technology and then revealed independently when observing the sample under different observation conditions. Here the laser-induced nanostructures allows to control the film birefringence and dichroism, giving rise to different colour gamuts in modes of reflection and transmission using polarized or non-polarized white light as an illuminant. The strategy of such a technology is to identify sets of nanostructures that satisfy particular combinations of colours in the selected modes of observation that we name conditions for multiplexing. The experiments for this chapter were performed at LabHC using a Pharos laser with frequency doubling (wavelength 515 nm) while working at a pulse duration of 200 fs and at 610 kHZ repetition rate.

1. Introduction

Standard pigments or dyes either absorb or scatter light with different wavelengths. To alter the colour of such pigments, one needs to change the chemical formulation, thus making the change of the colour difficult to engineer. On the other hand, nanoparticles can be engineered to either absorb, scatter or do both by changing their shape, size or overall geometry thus providing large variation of colour change. Recently, advancements in plasmonic colours have generated interest as they are promising to have high durability, high spatial resolution, efficient vibrant nature and in some cases possess dichroic properties, that could have a large technological impact on the area of colouring transparent materials. Such plasmonic colours arise due to resonant interactions between the nanostructures and the interacting light as already discussed in Chapter I. They are compatible with mass production and require a reduced number of materials in the whole process.[9] Different techniques have been implemented to print structural plasmonic colours in the past such as EBL, polymer replication, self-assembly and post laser treatment of plasmonic surfaces.[11,162,163,164] EBL has been used first for demonstrating full colour printing by encoding the colour information in nanodisks of Ag/Au. The colours here arises due to plasmon and Fano resonances that can be tuned at will by altering the size of these nanodisks.[11] Moreover, EBL was also used to fabricate circular gap plasmon Au resonators arranged in a periodic array for printing colours. To enhance the durability of these colours, coatings were proposed to protect the metal nanostructures. In reference[165] Poly(methyl methacrylate) (PMMA) was used to coat plasmonic resonators and enhance their durability, but to the detriment of the red content in the colours. Further, aluminum (Al), a cheaper metal, has also replaced Ag/Au for mass production of plasmonic structural colours using EBL. It was demonstrated that Al nanorods antennas were produced to print polarization driven plasmonic colours arising due to the local resonances and diffractive effects which were tuned by altering the geometry of Al nanorods.[166]

EBL, which is limited to small surfaces with nanometric precision can be extended to larger surfaces by using large area self-assembly technology or replication methods. Hojlund-Neilsen et al. demonstrated mass production of plasmonic colours using Al thin film coating produced using polymer replication technique via roll to roll printing, film inserting molding, and direct injection molding of the polymers.[162] Different replication techniques include nanoimprint lithography, roll to roll nanoimprint lithography, and roll to roll extrusion coating techniques that bring fabrication of plasmonic colours from laboratory to polymer based industries.[167] Other techniques, for production of plasmonic nanostructures on large scale has raised development in approaches including self-assembly of nanostructures and nanoparticles. Such a methodology, can produce nanoparticles of varying size that can be used to produce resonances within the visible region. Such self-assembly approach was used by Wang et al. to create periodic nanostructures on centimetric scale samples.[163] Other methods to produce self-assembly of nanostructures/nanoparticles include colloidal self-assembly, direct self-assembly or dewetted nanoparticles, where narrow resonances are achieved by tuning the contact angle of metal dewetted nanocaps, which gives rise to large range of colours due to the excitation of localized surface plasmons in the particles.[168]

Another way to control plasmonic colours have been to use post laser treatments on plasmonic nanostructures or nanoparticles. Metal surfaces have been modified by lasers (fs, ns, cw) to generate surface colours. The idea of using post laser treatment on nanostructures is to reshape the structures thus generating the colour change. In past, carbon dioxide lasers have been used on Au thin films, to fabricate wide range of colours, using direct patterning of nanostructures.[169] Further, Zhu et al. showed how laser pulse energy density gives rise to photo thermal re-shaping of metasurfaces thus generating different plasmonic resonances leading to different colours.[170] As discussed above, each technology possesses some advantages and disadvantages over one another. Although, laser induced post treatments for morphological changes for colour productions are irreversible, they hold advantage for being rapid, low-cost solution, and such technologies are flexible for large surfaces.

As stated above, these plasmonic colours can be light-polarization dependent or in other words dichroic in nature. The polarization driven colours are interesting in various applications as such colours provide degree of freedom to tune plasmon resonance mode as to enhance data storage capacity in some cases and encrypt or multiplex images that can be decrypted only while using right light polarization condition. Goh et al. utilized the idea of such spectral control to fabricate independent tunable colour pixels composed of Al nanosquares dimers.[149] Here a strong field is confined in the dimers gap and a coupled dipole mode is excited with one polarization state, while when the polarization is rotated by 90°, the coupling disappears. Using this, the authors multiplexed two images onto the same area using coupled dimers for orthogonal polarization state. While, Li et al. demonstrated dual-colour nanopixels fabricated as cross-shaped plasmonic cavity apertures in Al thin film. A change in the polarization of the incident light, gives rise to dual-colour selectivity in one nanopixel due to polarization driven resonances. This allowed authors to multiplex two images with nanometric resolution by patterning the pixels specifically.[171] While recently, Heydari et al. demonstrated image encoding using polarization multiplexing of two arbitrary full coloured images into a single pixel of array. Here each array exhibits two independent resonances which can be tuned in sRGB (standard Red Green Blue) colour space.[148] While using laser tuning of plasmon colouration earlier, Zijlstra et al. used randomly distributed Au nanorods supporting surface plasmon resonance (SPR) and used pulsed laser to selectively heat and reshape them, using wavelength and laser polarization as selection parameters. The printed images are read using two-photon luminescence at different wavelengths and polarizations. Authors used this technology, to multiplex eighteen different images using three different polymer layers, three different wavelengths and two different polarizations.[172]

In this chapter we demonstrate a two and three image polarized dependent multiplexing which encodes different sets of information in the same area which can be viewed by eye using white light. We combine laser processing and plasmonic nanocomposite thin films to control multidimensional colours to print up to three multiplexed images. The multiplexed images are printed using colour pallets fabricated using a femtosecond laser on nanocomposite thin films deposited on flexible glass substrates, a methodology discussed in chapter III. The multiplexing is achieved by selecting the modes from the colour pallets printed and observed in reflection and cross-polarized transmission. An explanation is provided further on conditions that the colour pallets in the modes must fulfill to produce a two or three image multiplexing, and how such conditions are satisfied with the plasmonic colours.

2. Experimental Techniques

2.1 Thin Film Fabrication

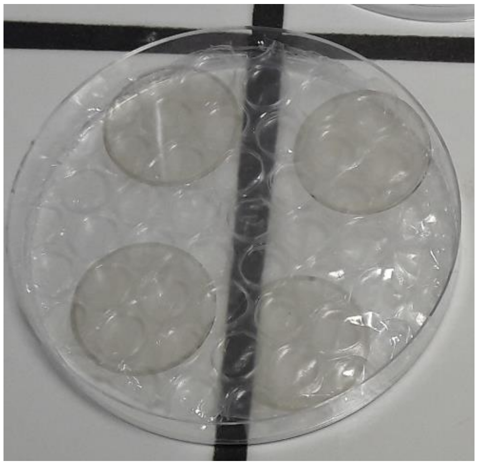

Figure V.1: Ag:TiO_2 films deposited on four circular flexible glass. The photographs were taken after the three UV-VIS cycle.

The films were fabricated using similar TiO_2 sol that was used in Chapter III. Although, due to different dimension of the substrate, the sol was spin-coated at 2000 rpm/30s on circular flexible glass coupon provided by SCHOTT (AS87, 100 µm). The films were impregnated with similar protocols as described in Chapter III, along with UV-Visible cycles to obtain Ag:TiO_2 nanocomposite bleached films.

2.2 Laser Setup

The laser system, comprises of a single unit integrated Pharos laser as detailed in the chapter IV, with a pulse duration of 200 fs at a fundamental wavelength of 1030 nm and at 610 kHz repetition rate for this study. Frequency doubling to get a wavelength of 515 nm is achieved with a BBO crystal as explained in the last chapter. This wavelength is used to excite the localized surface plasmon resonance of Ag nanoparticles in the composite films and is poorly absorbed by the TiO_2 matrix or the substrate. The low repetition rate in the last chapter was used to avoid deformation of the plastic substrate, but due to the fact that we are working on flexible glass in this study, we use similar parameters as used in Chapter III at higher repetition rates due to resistance of glass to higher temperatures.

3. Conceptual Insights

As stated above, image multiplexing is defined as encoding different images onto the same area, which is able to display different images independently in various observation conditions or modes. In this section, emphasis is given to how we solve this problem by combining laser processing with nanocomposite thin films of Ag:TiO_2.

3.1 Multidimensional Colours

Our laser-processed films exhibit dichroic properties, which means colours that depend on the conditions of observation. In this section we introduce the concept of multidimensional colours that is a set of colours that defines a specific kind of nanostructure defined by statistical properties as described in section 3.3 resulting from a given set of fabrication parameters including the sample and the laser parameters. To define the multidimensional colour, that can be called hypercolour, we first define the modes of observation that will be used to characterize the sample and we measure the colour of a single nanostructured pixel in these different modes. The modes that will be used in this thesis are reflection under non polarized white light and transmission using polarized white light. More specifically, we depict in Figure V.2 the concept of a nanostructured pixel exhibiting a 3-dimensional colour in the following selected modes of observation: reflection under non-polarized light and a given angle of incidence, transmission under normal incidence and in between two polarizers crossed with an angle β between them. By rotating the sample in its plane, we can select two different modes characterized by the azimuthal angle α of the sample.

An interesting feature of the laser-processed Ag:TiO_2 nanostructured pixels is that pixels generated with different laser parameters can exhibit the same colour in some of the modes and different colours in the other modes. This opens the possibility to find out conditions for multiplexing.

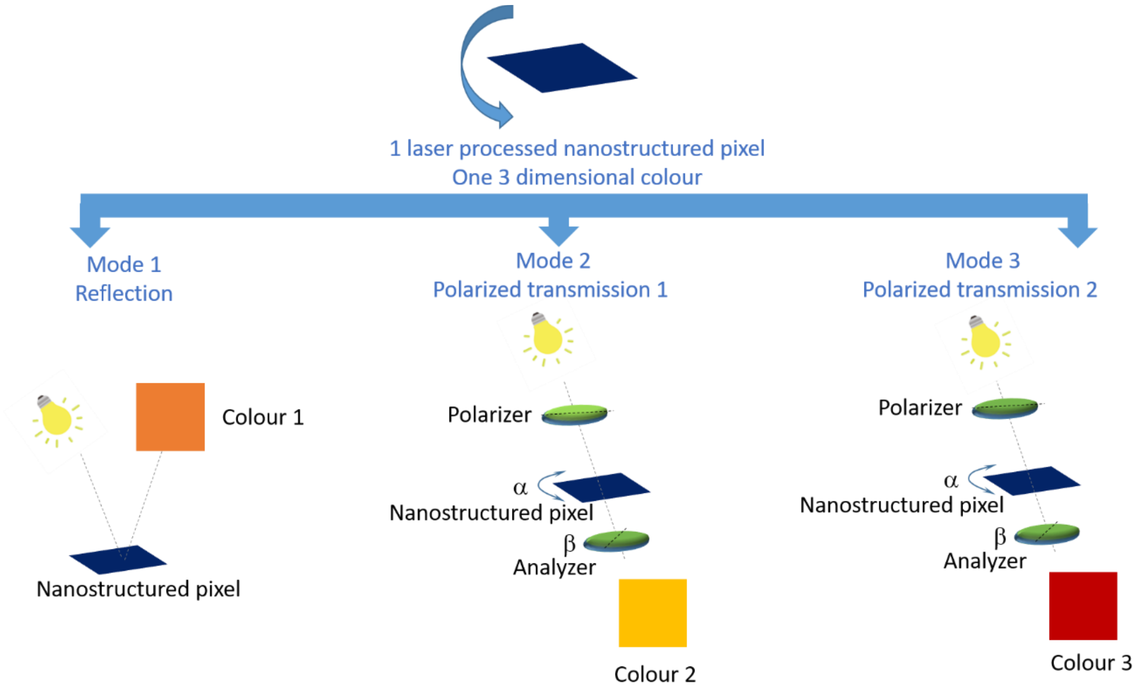

Figure V.2: A concept for multidimensional colour illustrating that a single laser nanostructured pixel can generate three different colours in three different modes of observation.

3.2 Conditions for Mutiplexing

To understand the conditions required for multiplexing let us consider two situations where we want to multiplex two or three bicolour images. In Figure V.3a, images A and B are combined in image C. Image C is then the final image printed on the sample where each pixel is characterized by a 2-dimensional colour (one colour per mode of observation) composed of a colour in mode 1, where image A must be observed, and a colour in mode 2, where image B must be observed. In order to properly print image C on the sample we need to find out 4 different nanostructures that exhibit the specific 2-dimensional colours shown in the table on the right-end side. This table is like a logical graph that shows all the possible combinations of the two colours selected in the two modes of observation. In a general manner the number of possible combinations, i.e. the number of nanostructures (NS) required to implement image multiplexing, equals the product of the number of colours in each mode of observation selected for the multiplexing.

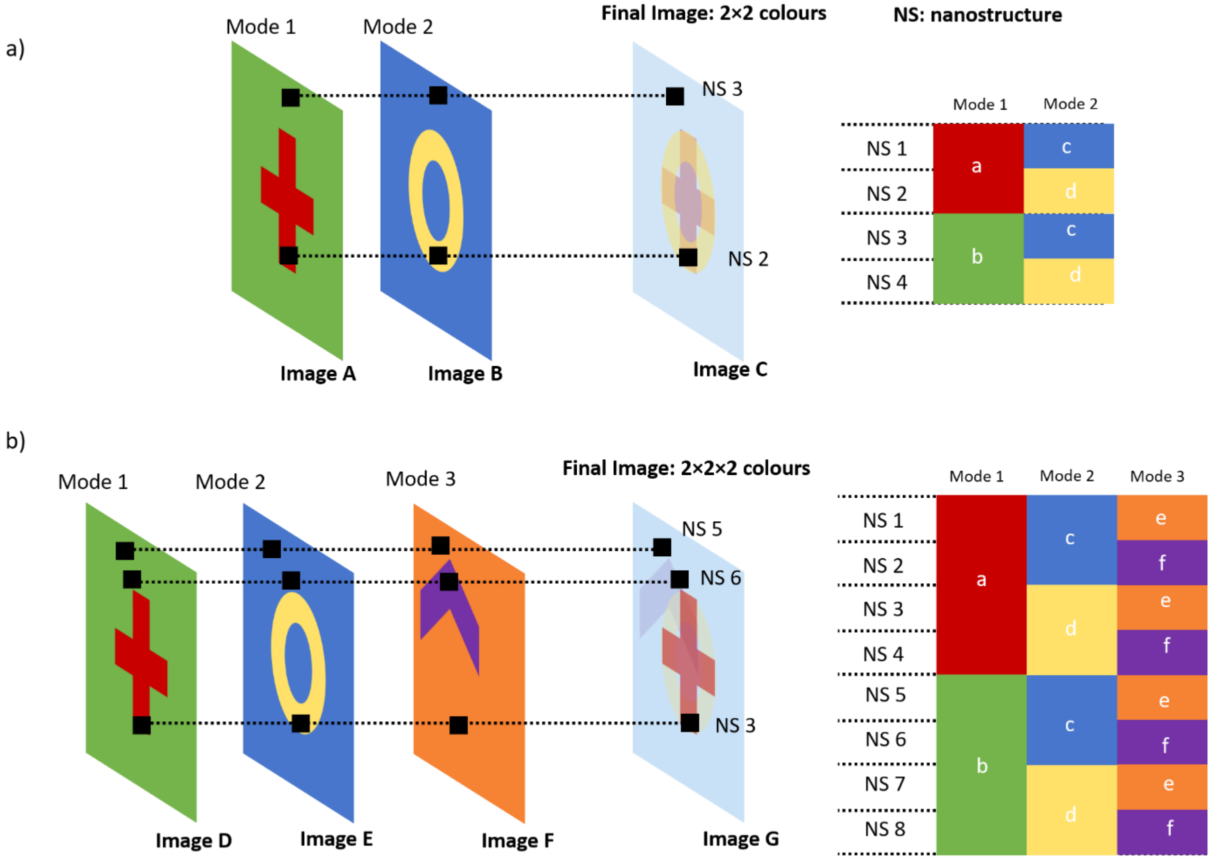

	Mode 1	Mode 2
NS 1	a	c
NS 2		d
NS 3	b	c
NS 4		d

	Mode 1	Mode 2	Mode 3
NS 1	a	c	e
NS 2			f
NS 3		d	e
NS 4			f
NS 5	b	c	e
NS 6			f
NS 7		d	e
NS 8			f

Figure V.3: Conditions to satisfy image multiplexing for a) two images and b) three images. A nanostructured pixel is depicted by a black square.

For printing a multiplexed image including the information of 3 different bicolour images, the logical graph that must be satisfied is given in Figure V.3b. It contains 2x2x2=8 different nanostructures whose 3-dimensional colours provides all together, all the possible combinations of the 2 colours selected in each of the 3 modes. In such an example, image G is nothing else than an image with 8 different kinds of pixels, where each kind of pixel exhibits a specific 3-dimensional colour that gives the colour of image D in mode 1, the colour of image E in mode 2 and the colour of image F in mode 3.

Let us generalize to more colours per mode. Each time you add a colour in a mode, you have to build the logical graph with this new colour. This leads to add a number of nanostructures equal to the product of the number of colours in the other modes. Figure V.4a shows an example where we use 5 colours in mode 1 and 2 colours in mode 2 and 3, respectively.

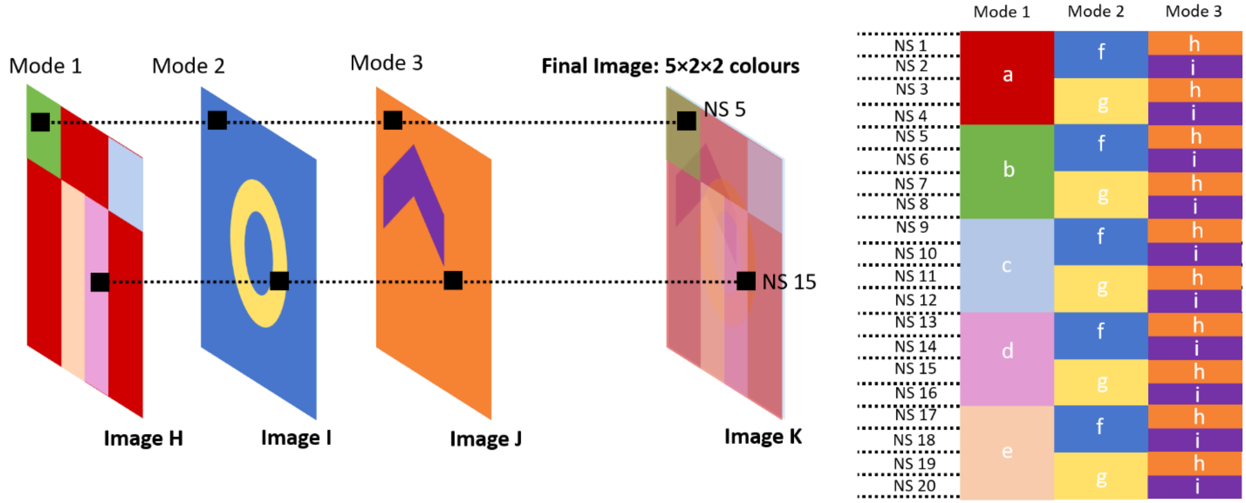

	Mode 1	Mode 2	Mode 3
NS 1	a	f	h
NS 2	a	f	i
NS 3	a	g	h
NS 4	a	g	i
NS 5	b	f	h
NS 6	b	f	i
NS 7	b	g	h
NS 8	b	g	i
NS 9	c	f	h
NS 10	c	f	i
NS 11	c	g	h
NS 12	c	g	i
NS 13	d	f	h
NS 14	d	f	i
NS 15	d	g	h
NS 16	d	g	i
NS 17	e	f	h
NS 18	e	f	i
NS 19	e	g	h
NS 20	e	g	i

Figure V.4: Conditions to satisfy image multiplexing for three images. Here we use 5 colours in mode 1, while in mode 2 and 3, 2 colours are used.

If the logic for creating the multiplexed image is quite simple, we understand that the challenge is to identify the set of nanostructures that can satisfy such a logical graph. In the following section, we explain our methodology to find out such logical graphs among the nearly infinite number of nanostructured pixels that can be produced by varying continuously the printing parameters that are: laser fluence, laser repetition rate, scan speed, laser focusing, overlapping between successive laser written lines, and laser polarization.

We worked in an empirical manner to find out what can be called orthogonal parameters for 2 modes. Orthogonal parameters are printing parameters that vary the colour in one mode but not in the other considered mode, respectively. When one finds such orthogonal parameters for given modes of observation, one can print a pixel matrix where horizontal lines exhibiting a vertical gradient of colours appear in mode 1 and vertical lines of colours exhibiting a horizontal gradient appear in modes 2. If one extends the number of colours per mode and the number of modes to the ones used in the example of Figure V.4, one can print a matrix exhibiting the patterns drawn in Figure V.5, where one can see the horizontal lines in mode 1 and vertical lines in modes 2 and 3 but with two different colour arrangements. These sketches result from a specific organization of the useful nanostructures in the matrix as shown by the number of each pixel on the sketch that refer to the nanostructure number of Figure V.4. This kind of representation is a visual guide to rapidly identify which printing parameters can be used for producing a set of hypercolours useful for multiplexing.

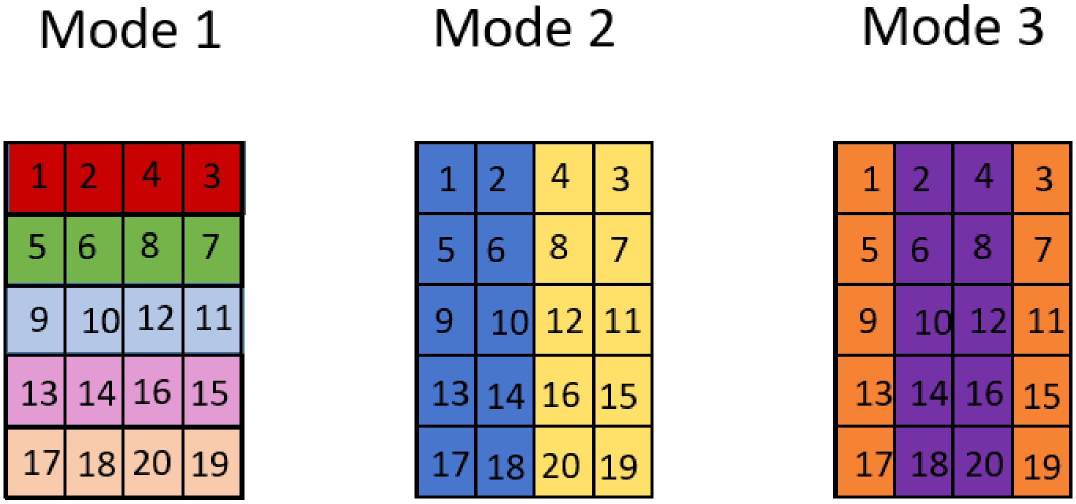

Figure V.5: A sketch for pixelated matrix printed with orthogonal laser parameters and observed in three different modes of observation. Here each squared box represents nanostructure printed with a specific laser parameter.

For this, the next section presents the optical properties of the laser-printed nanostructured pixels.

3.3 Influence of the Printing Parameters on the Optical Properties of the Nanostructures

Varying a single parameter of the printing process of Ag:TiO_2 nanocomposite thin films usually leads to change several opto-geometrical parameters of the films simultaneously, like: the nanoparticle size distribution, the average depth of nanoparticles, the presence of self-organized gratings of nanoparticles and their regularity, the film thickness and refractive index (due to densification of the initial amorphous mesoporous TiO_2 film), and the presence of a periodic surface modulation. Investigating the effect of individual printing parameters on each opto-geometrical parameter of the nanocomposite film is impossible. A precise investigation of the film volume and surface at the nanometer scale indeed requires SEM, TEM, micro-Raman or ellipsometric characterization that cannot be implemented systematically on all the pixels. We therefore made a first selection of interesting modes, printing parameters and ranges in which the latter should be varied by a visual observation of the pixel colours in various modes. For this, 1 mm² square pixels were drawn in matrices where only two parameters were varied along each axis of the matrix. Observing these matrices in different observation modes gave clues to select the combination of useful modes and printing parameters.

The printing parameters that were varied are the scan speed, laser power, interline spacing, and laser polarization. As most of the nanostructures exhibited polarization dependent colours under white light, it rapidly became obvious to use a polarized mode as one of the useful modes with the laser polarization as a parameter controlling the colour in this mode. Further, placing the sample in between two polarizers crossed at 80° gave more colour variations than using only a single polarizer. As a consequence, the polarized mode that is used in the following sections is the one described in figure V.2 where the sample is placed between two polarizers.

For a fixed laser scan speed, interline spacing (dy) and repetition rate, a pixelated matrix was printed for different laser polarization and laser fluence values. As we were restricted to speeds up to 10 mm/s (explained in last chapter) it was observed that, a change in the scan speed variation did not provide a huge change in the colour gamut, while a constant higher dy was chosen as to increase the printing time of the final image.

While a variation in the laser fluence gave various dichroic colours in reflection and not under polarized transmission, a change in the laser polarization allowed to vary colours under polarized transmission but not under reflection as illustrated in Figure V.6.

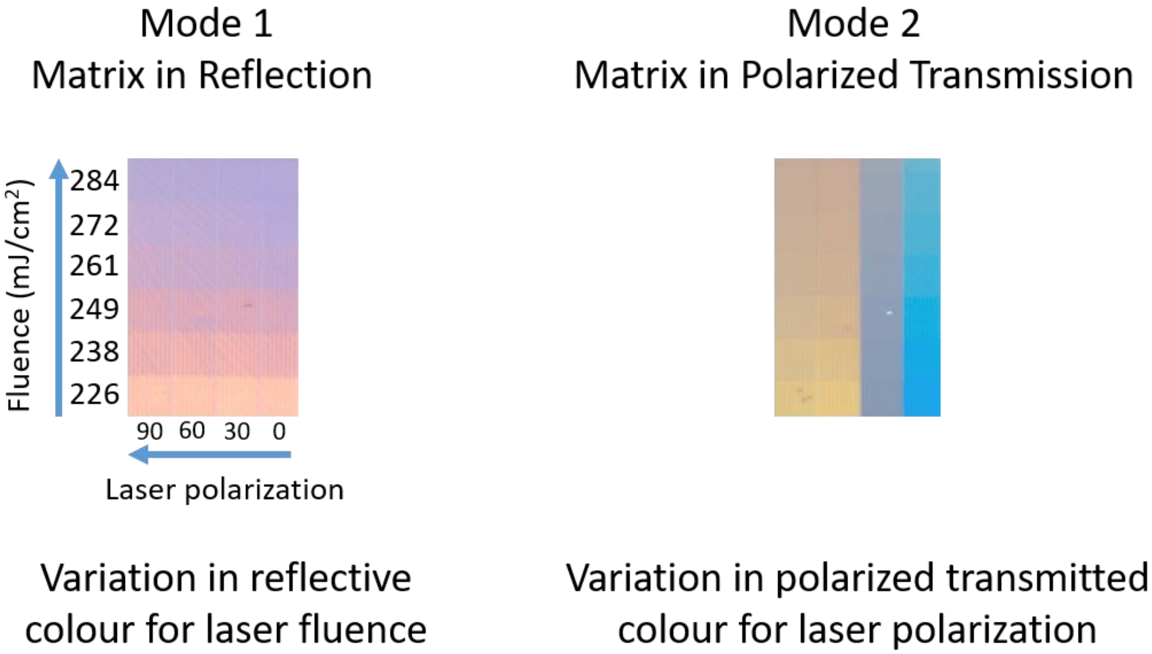

Figure V.6 : When the laser printed matrix is illuminated and observed under reflection (Mode 1), it is seen that while the fluence is increased from 226 to 284 mJ/cm^2, one can observe a variation in the reflective colour while, the colours for various laser polarizations (from 0° to 90°) remain the same. On the other hand, when the same matrix is illuminated under polarized transmission (Mode 2), the colour now strongly varies with the laser polarization angle but not with the fluence. Such orthogonal parameters give rise to modes that can be used for multiplexing since we get a vertical gradient in one mode and horizontal gradient in the other mode.

In order to print complex images, we printed square pixels 80 µm in size with an interline spacing dy of 15 µm. Furthermore, to have a good colour matching between the different powers in the polarized mode, laser fluence was varied from 215 to 354 mJ/cm^2 (Figure V.7) at a constant speed of 7 mm/s and the laser polarization was varied from 0 to 150. Although, the fluence range specifically used for image multiplexing in reflection mode varied from 226 to 284 mJ/cm^2 (2 and 3 image multiplexing) while in polarized transmission mode, the polarization range varied from 0 to 150° from which for 2 image multiplexing, the polarization values were chosen from 0 to 90° and for 3 image, polarization values were 30, 60, 120 and 150° respectively, as illustrated in the next sections. The sole aim of this study was to find orthogonal parameters, which can be used for multiplexing. It is interesting to note that the laser polarization can be varied continuously when printing a multiplexed image containing two different images to be displayed in two different modes (Modes: reflection and polarized transmission), as shown later. Further, when selecting actual laser-polarization angles, a 3-image multiplexing can be implemented where one image is displayed in the reflection mode, and the two other images are displayed in the polarized mode but for two different azimuthal angles as explained further in the next section.

3.4 Origin of Colour Variations and Dichroism

To better understand what are the opto-geometrical parameters that influence the colour change, three nanostructures from the ones used previously were observed by SEM and HAADF TEM from the top view and the cross-section (preparation of the FIB lamella by David Troadec at IEMN). The cross-section was cut along the white dashed lines as shown in Figure V.7c. These electron microscopy characterizations were conducted on nanostructures with three different laser fluences for laser polarization 0° (horizontal polarization depicted by double side arrow in yellow) and 90° for one parameter as to check the effect of laser polarization of the nanostructure anisotropy (Figure V.8a). It was observed that when working on the lower fluence value of 249 mJ/cm^2 (Figure V.7c), the Ag nanoparticles grew very slightly with the mesoporosity of TiO_2 being still present even though the film thickness is smaller than on the initial film (200-250 nm). An increase in the laser fluence to 307 mJ/cm^2, tends to increase the nanoparticle size (white bright particles) and decrease their density, especially on the top part of the film. The bottom part contains mainly a higher density of smaller particles as for the lower fluence (Figure V.7b). The maximum fluence of 354 mJ/cm2 (Figure V.7a) tends to start organizing the nanoparticle in the form of a grating. The latter is embedded inside the TiO_2 matrix, as illustrated in Chapter III also while the matrix seems to be collapsed at this fluence due to a temperature increase (film thickness of 154 nm). It is to be noted that the parameters for obtaining self-organization processes when compared to results obtained in Chapter III, vary in terms of speed and fluence, due to changes in the setup and few parameters like beam diameter of around 20 µm as compared to beam diameter of around 33 µm in the laser setup used in chapter III . In this chapter, the aim is not to study the self-organization processes of the nanoparticles inside the

TiO_2 matrix, but rather to characterize the nanostructures that are useful for multiplexing.

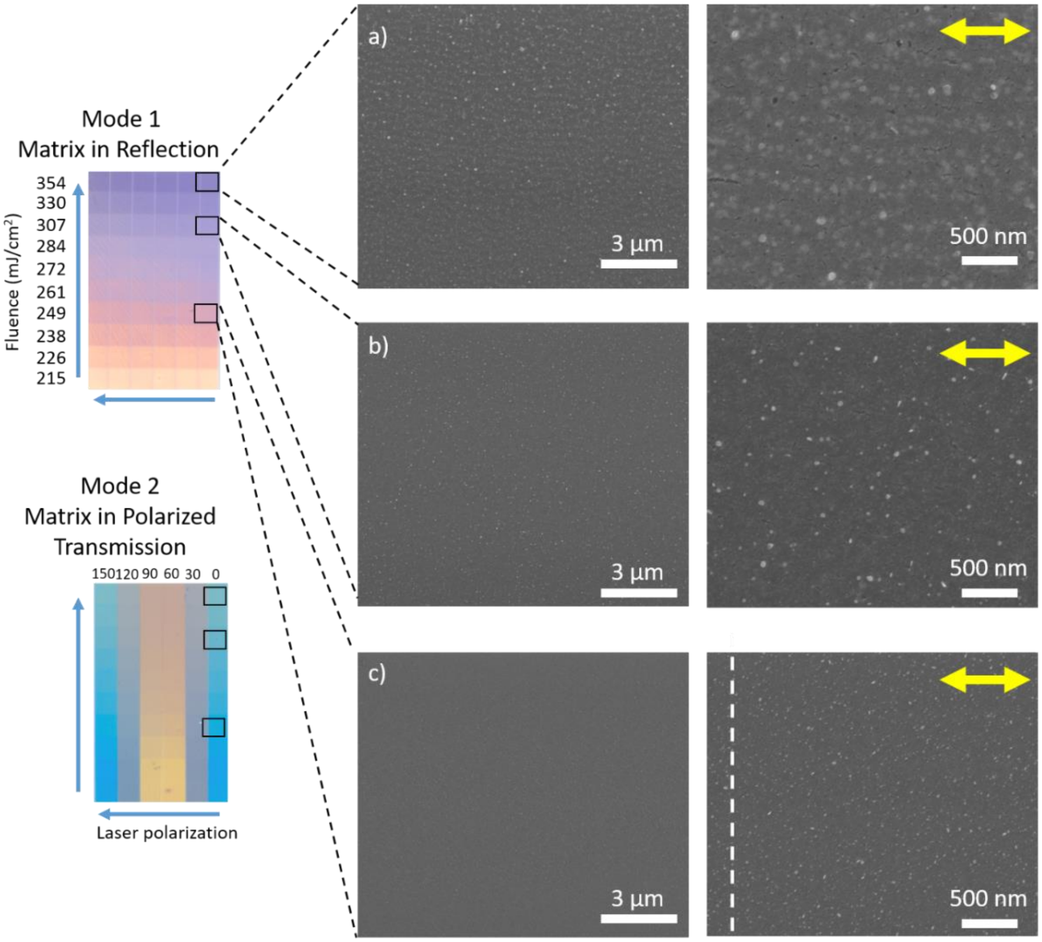

Figure V.7: Control of the dichroic properties of the nanostructures using fs laser on Ag:TiO_2 nanocomposites. The matrix were printed with varying laser fluence and laser polarization. The image shows the matrix in reflection and under polarized transmission. SEM images for three fluences of a) 354, b) 307, and c) 249 mJ/cm^2 are shown here for laser polarization 0°. The white dashed line shows the way FIB cross-section was made and the yellow double sided arrow depicts the laser polarization.

From such characterizations, one can infer that the dichroism occurring at lower fluences is not due to the self-organization process, but most probably due to shape anisotropy of the nanoparticles, even though it is not obvious for such small particles. Higher magnification HAADF STEM micrographs of sample top views are show in Figure V.8. As was depicted in chapter III, the laser polarization can influence the shape and elongation of Ag nanoparticles along its direction. The anisotropy becomes prominent for laser fluence 307 mJ/cm^2 (Figure V.8b), where the nanoparticles seems elongated along the polarization direction (yellow double sided arrow) and a hint of shape anisotropy is dominant from the images. The change in the laser polarization by

90°, with an increase in laser fluence to 354 mJ/cm^2, creates the shape anisotropy and elongation in the similar direction (Figure V.8a). At this fluence, the nanoparticle organization is parallel to the laser polarization. This was explained in Chapter III, where self-organization and anisotropy of nanoparticles were discussed in detail. However, at the lower fluence, it is still hard to conclude about any anisotropy because of the very dense and small nanoparticles.

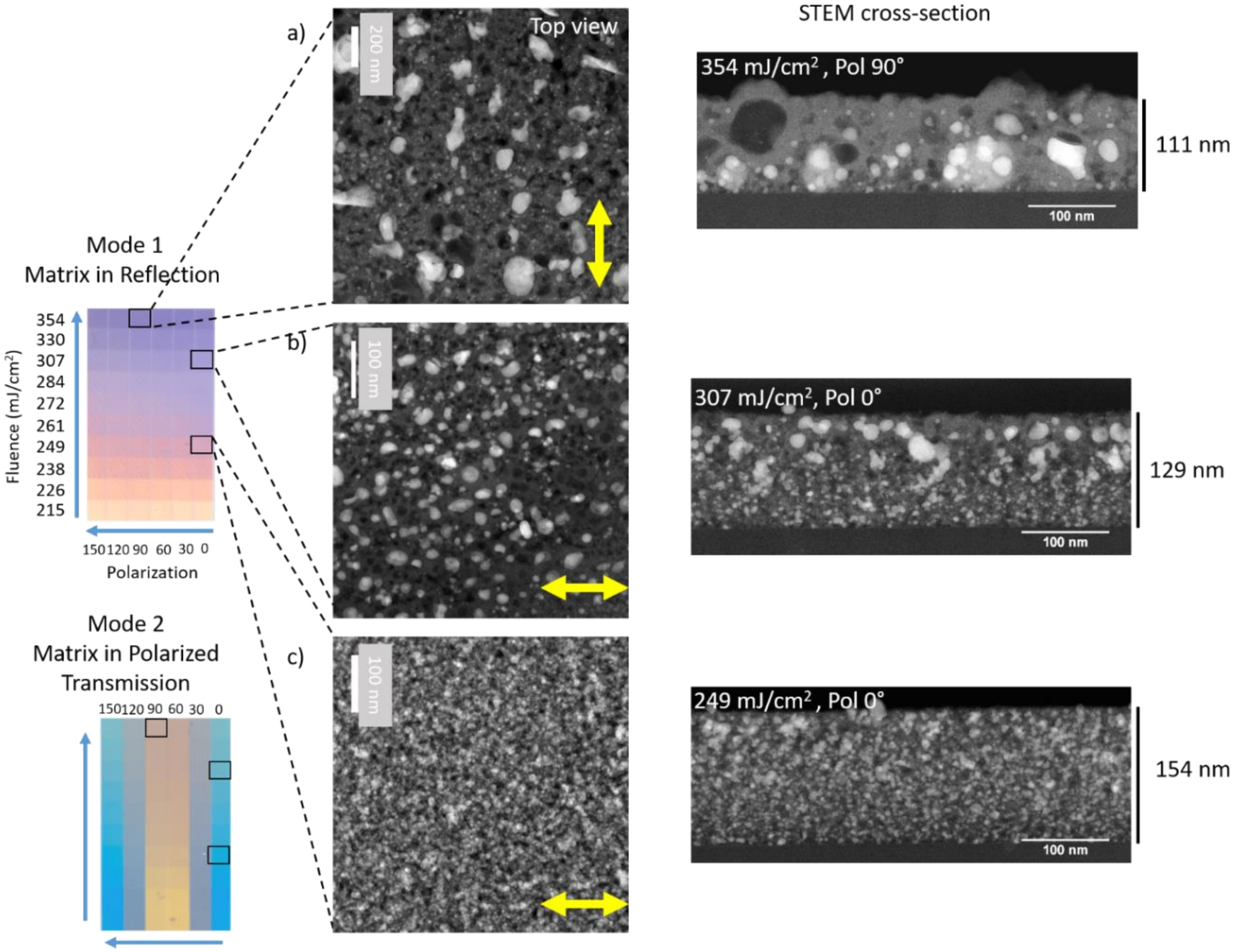

Figure V.8: STEM images for three fluence of a) 354, b) 307, and c) 249 mJ/cm^2 shown for different laser polarization indicated with a double side yellow arrow as compared to Figure V.7. The images indicate a shape anisotropy and elongation of silver nanoparticles along with the direction of laser polarization, especially for 307 and 354 mJ/cm^2. The STEM shows how the matrix collapses as the fluence is increased and the density of nanoparticles is decreased. While, lower fluence values of 249 mJ/cm^2, shows higher density of silver nanoparticles with smaller size.

4. Image Multiplexing

4.1 One Image (Not Multiplexing Yet)

Before starting to discuss image multiplexing, it is important to elaborate how a single image can be printed using such multidimensional colours on the nanocomposite film using lasers.

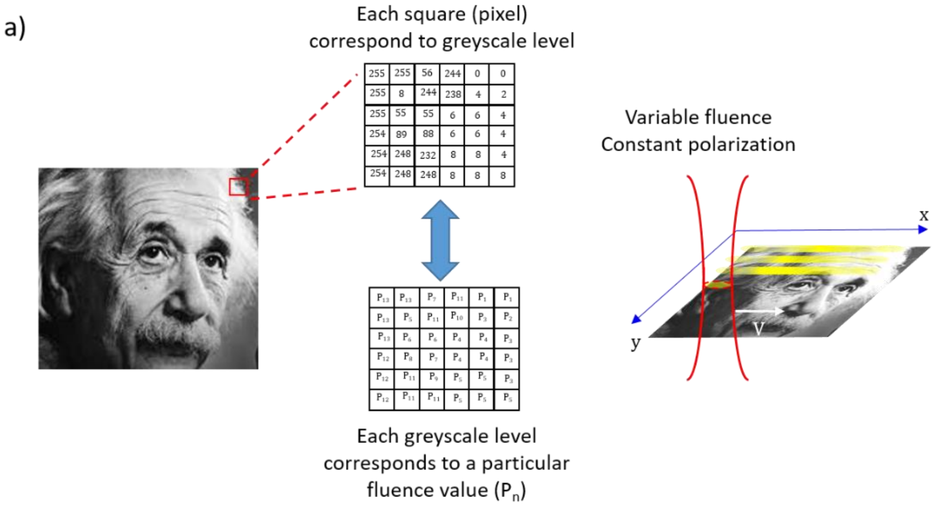

255	255	56	244	0	0
255	8	244	238	4	2
255	55	55	6	6	4
254	89	88	6	6	4
254	248	232	8	8	4
254	248	248	8	8	8

P_{13}	P_{13}	P_7	P_{11}	P_1	P_1
P_{13}	P_5	P_{11}	P_{10}	P_3	P_2
P_{13}	P_6	P_6	P_4	P_4	P_3
P_{12}	P_8	P_7	P_4	P_4	P_3
P_{12}	P_{11}	P_9	P_5	P_5	P_3
P_{12}	P_{11}	P_{11}	P_5	P_5	P_5

b) Printed Image

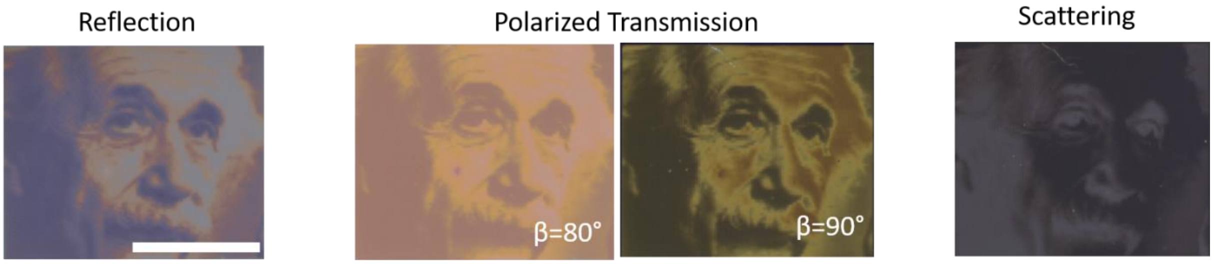

Figure V.9: Illustration for coloured image printing using fs laser on nanocomposite film while defining a) laser fluence as linear function of the 256 greyscale levels. b) Image printed with 256 greyscale levels as observed in reflection mode of illumination, polarized transmission for different β values and scattering mode. The scale bar in the image corresponds to 4 mm.

As we need to print a single image that can be observed under different modes of observation, with only various colours but always with the same image, a single printing parameter is varied. Here, a coloured image is converted into a greyscale image by defining the laser fluence as a linear function of the 256 greyscale levels. All the other printing parameters are kept constant. One can also print an image by defining the laser polarization angle as a linear function of the

256 greyscale levels for a constant laser fluence. Figure V.9 illustrates coloured printing of a single image using fs laser on nanocomposites. The image was optimized for the reflection mode and gave the better colour rendering in this mode. But the same image can be observed in all the other modes (polarized transmission for different values of β and scattering), with only different colour gamuts. One can note that the image in the scattering mode appears to the human brain as a negative image, which can be a way to authenticate the picture.

Here, the image is printed pixel by pixel, where a single pixel is 80 µm in size, with dy corresponding to 15 µm and a scan speed of 7 mm/s. The fluence range is from 215 to 307 mJ/cm^2 with a laser polarization parallel to the laser writing direction (horizontal on the image).

4.2 Two-Image Multiplexing

The idea here is to multiplex two greyscale images that will appear independently in two different modes of observation. Note that even though the final images displayed in each mode will be coloured, we just convert in these experiments the greyscale image into the gradient of colours that can be obtained by varying one parameter of the laser printing process. The first step is to find out two parameters that appear as orthogonal in well suited modes. According to what was shown in section 3.3 the laser fluence and the laser polarization can be used to print a multiplex image that will display the fluence encoded image in the reflection mode and the polarization encoded image in the polarized transmission mode. In order to satisfy the conditions for two image multiplexing, the fluence range is limited from 226 to 284 mJ/cm^2 and the laser polarization angle is varied between 0° and 90° to encode the second image.

In the example shown in Figure V.10, the initial pictures have 256 grey levels and the multiplexed image is printed using a linear variation of the fluence and laser polarization according to the initial grey levels of the images, with steps of 58/256 mJ/cm^2 and 90/256° respectively. We then obtain 256x256 different kinds of nanostructures whose features slightly vary from one to the other.

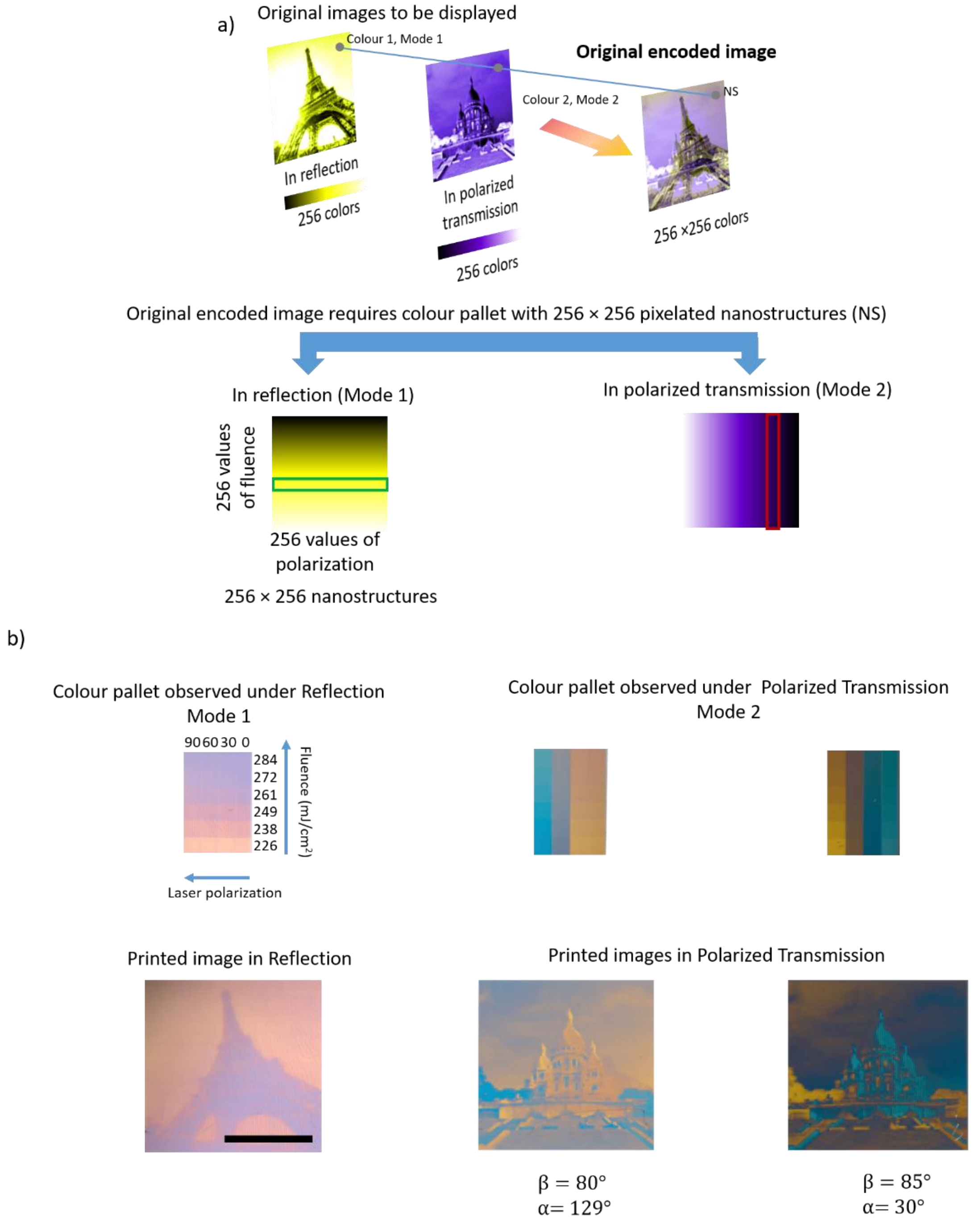

Figure V.10: a) Requirements for producing two image multiplexing using 256 × 256 nanostructures. The encoded image should be such that different nanostructures gives similar colour in polarized transmission and colour pallet in reflection and vice versa. b) Illustrates the colour pallet observed under different modes of reflection and polarized transmission for specific laser fluence and polarization with the corresponding printed image in modes of reflection and polarized transmission. The scale bar on the image corresponds to 4 mm.

It is interesting to note that rotating continuously the sample in its plane in between the two fixed polarizers changes the colour gamut and the image contrast, since different colours appear in different places of the second image. We can add that this colour gamut can also be changed by changing the angle between the two polarizers. With such an encoding, the same picture of the "Sacré Coeur" (Cathedral in Paris) will appear regardless the angles α and β chosen in the polarized transmission mode, only the colours of the image will change with the angles. The colour distributions that can be obtained in the polarized transmission mode are very dependent on the initial composition (Ag content, mesopore size, quantity of crystallized TiO_2 nanocrystals), thickness of the nanocomposite film and the substrate nature. Producing the same gamut for specific combination of angles is therefore very tricky without any a priori knowledge about the sample. This flexibility to get specific colour gamuts makes such a printing very secured for authentication application for instance. As the laser processing completely changes several parameters of the initial films, it prevents from measuring a posteriori the initial state of the sample.

To the best of our knowledge, it is the first demonstration of two-image multiplexing where the two images are displayed in reflection and transmission under white light. Up to now, only the polarization was used to switch between two-colour images either in reflection or in transmission only as also discussed in the introduction of this chapter. In the next section, we focus on how we implement the technology to print a three image multiplexing using a similar combination of fs laser and the nanocomposite thin films.

4.3 Three-Image Multiplexing

Here again, the original idea is to display three different images under white light illumination (rather than monochromatic light as shown in several articles) in three different modes of observation. As explained earlier, the conditions fulfilled to construct the logical graph are much more binding with three modes. Starting from the result shown for 2-image multiplexing, we can wonder if two different azimuthal angles could be used to display two different images in the polarized transmission mode, as illustrated in the literature where only the polarization angle was varied to change the displayed image.

As explained in Figure V.4, the conditions required to fulfil the construction of the logical graph for 3-image multiplexing with a multicolour image in mode 1 (reflection) and two different bicolour images in modes 2 and 3 (polarized transmission for two azimuthal angles), are to find out modes in which the 2D matrix of squares exhibits a vertical gradient of colours in mode 1, as shown in the previous section, and two different combinations of bicolour vertical lines in the other modes. These combinations, depicted in Figure V.5, are actually present in the matrix drawn in Figure V.6 for 2-image multiplexing, provided that we select particular values of the azimuthal angle α. The results are shown in Figure V.11 if we consider the polarization angles 30°, 60°, 120° and 150°. Knowing that such a result exists, one can wonder if it can be predicted.

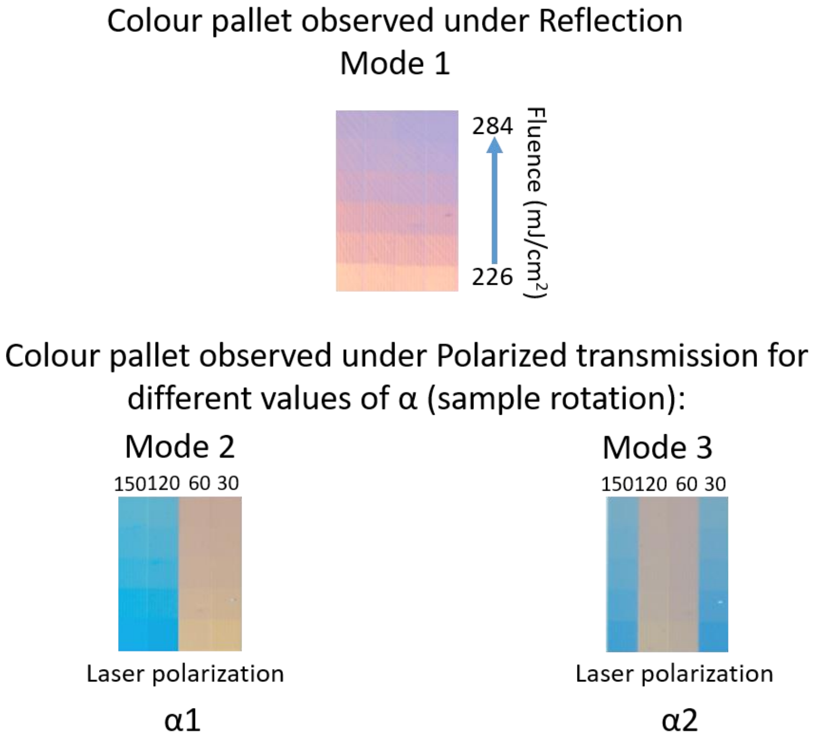

Figure V.11: Colour pallet matrix printed with different laser fluence from 226 to 284 mJ/cm^2 and laser polarization 30, 60, 120, 150° respectively and observed in Reflection in Mode 1 and polarized transmission for different values of sample rotation or α in Mode 2 and 3 respectively, depicting a solution for 3-image multiplexing.

For this, let us consider the sample as a birefringent thin film with neutral axes along and perpendicular to the orientation of the laser polarization used to print the squares. Let us name x and y the two neutral axes. Such a sample can be characterized by two different complex refractive indices or by two different components of the complex transmittance of the film written $t_x\, e^{i\varphi_x(\lambda)}$ and $t_y\, e^{i\varphi_y(\lambda)}$, respectively along x and y. The expression for the intensity transmitted under normal incidence through the dichroic sample placed between two polarizers whose axes are at α and α+β from x, as shown in Figure V.12a, is thus given by:

$$I(\alpha,\beta,\lambda\,) = \left|E_0 cos(\alpha) t_x(\lambda) e^{i\varphi_x(\lambda)} cos(\alpha+\beta) + E_0 sin(\alpha) t_y(\lambda) e^{i\varphi_y(\lambda)} sin(\alpha+\beta)\right|^2$$

(Eq. V.1)

where E_0 is the amplitude of the incident electric field. After some calculations detailed in Annexure 1, the expression for this intensity at angle α and any wavelength, can be written as a function of three values of this intensity taken (or measured) at three specific values of α. For the sake of simplicity, we choose values: 0, $\frac{\pi}{4}$ and $\frac{\pi}{2}$, leading to the expression of intensity as:

$$\begin{aligned} I(\alpha,\beta,\lambda) = {} & \mathrm{I}(0,\beta,\lambda)\left[\frac{cos^2(\alpha)cos^2(\alpha+\beta)}{cos^2(\beta)} - \frac{cos^2\left(\frac{\pi}{4}+\beta\right) sin(2\alpha) sin(2\alpha+2\beta)}{2cos^2(\beta)\cos(2\beta)}\right] \\ & + I\left(\frac{\pi}{4},\beta,\lambda\right)\frac{sin(2\alpha)sin(2\alpha+2\beta)}{\cos(2\beta)} \\ & + I\left(\frac{\pi}{2},\beta,\lambda\right)\left[\frac{sin^2(\alpha)sin^2(\alpha+\beta)}{cos^2(\beta)} - \frac{sin^2\left(\frac{\pi}{4}+\beta\right) sin(2\alpha) sin(2\alpha+2\beta)}{2cos^2(\beta)\cos(2\beta)}\right] \end{aligned}$$

(Eq. V.2)

The transmittance spectra of the system composed of the sample and the polarizers can be deduced for each value of α and β, from the equation V.2 after normalizing by the incident intensity. Such spectra can then be used to calculate the (CIE) XYZ values (Formula given in Annexure 2) to show the colour variation through the Chromaticity diagram for different values of α, β being fixed (Figure V.12b).

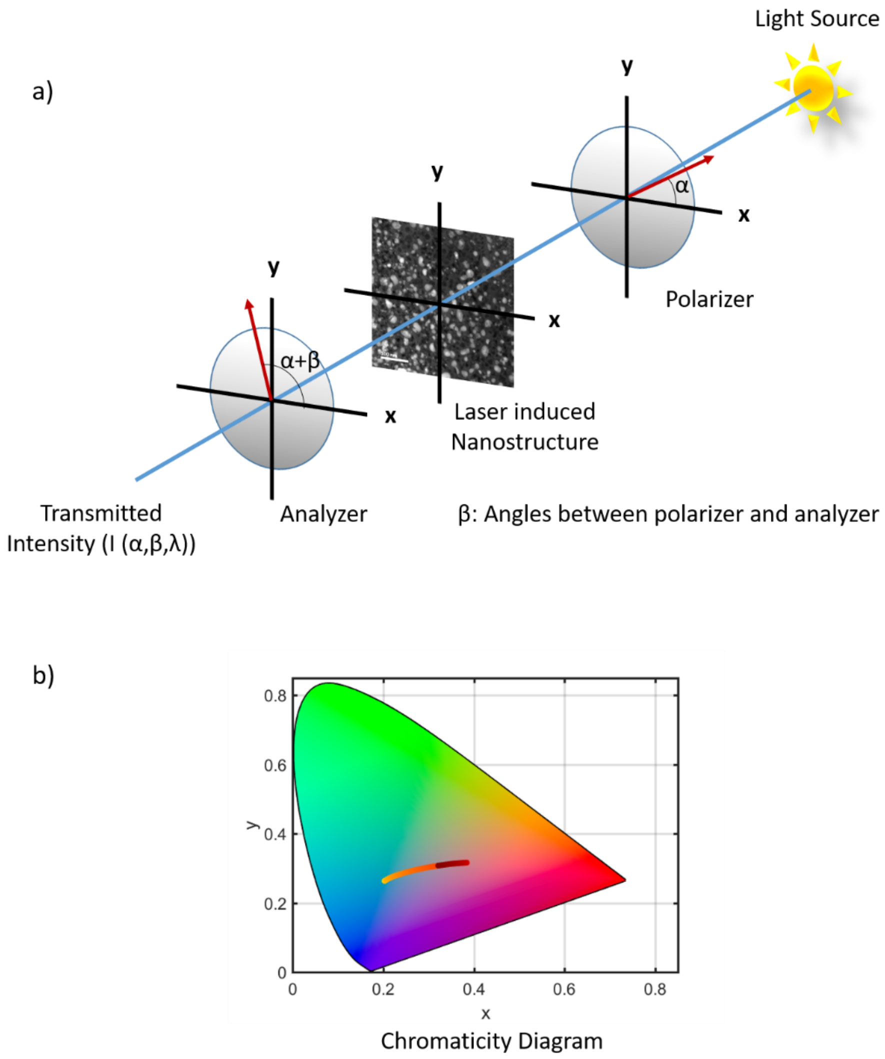

Figure V.12: a) Setup use to measure the polarized transmittance spectra. α is the angle between laser induced nanostructure oriented along the laser polarization and the polarizer axis. β is the angle between the two polarizers. The nanostructure here acts as a dichroic sample. b) The spectra data is converted to determine the CIE XYZ values which in turn displays the colour variation in the form of chromaticity diagram.

When rotating the laser polarization angle by θ during laser printing, the sample anisotropy is maintained but its neutral axis are rotated by the same angle. This means that a sample printed with the angle of polarization θ behaves as a sample printed with θ=0 provided that it is rotated between the two polarizers by an angle α=- θ (see Figure V.13a). According to Equation V.2, if we measure the transmittance of a sample printed for θ=0 between 2 polarizers for the three values of α=0, $\frac{\pi}{4}$ and $\frac{\pi}{2}$, the transmittance spectrum of such a sample can be deduced for any value of α, and we can use such a simulated transmittance spectrum to describe the one of a sample printed with laser polarization angle θ, by just shifting the value of α by θ. So let us imagine a sample with 4 squares printed with laser polarization angles 30, 60, 120 and 150° and let us draw their change of colour when rotating the sample in between the two polarizers. This gives the curves of Figures V.13b.

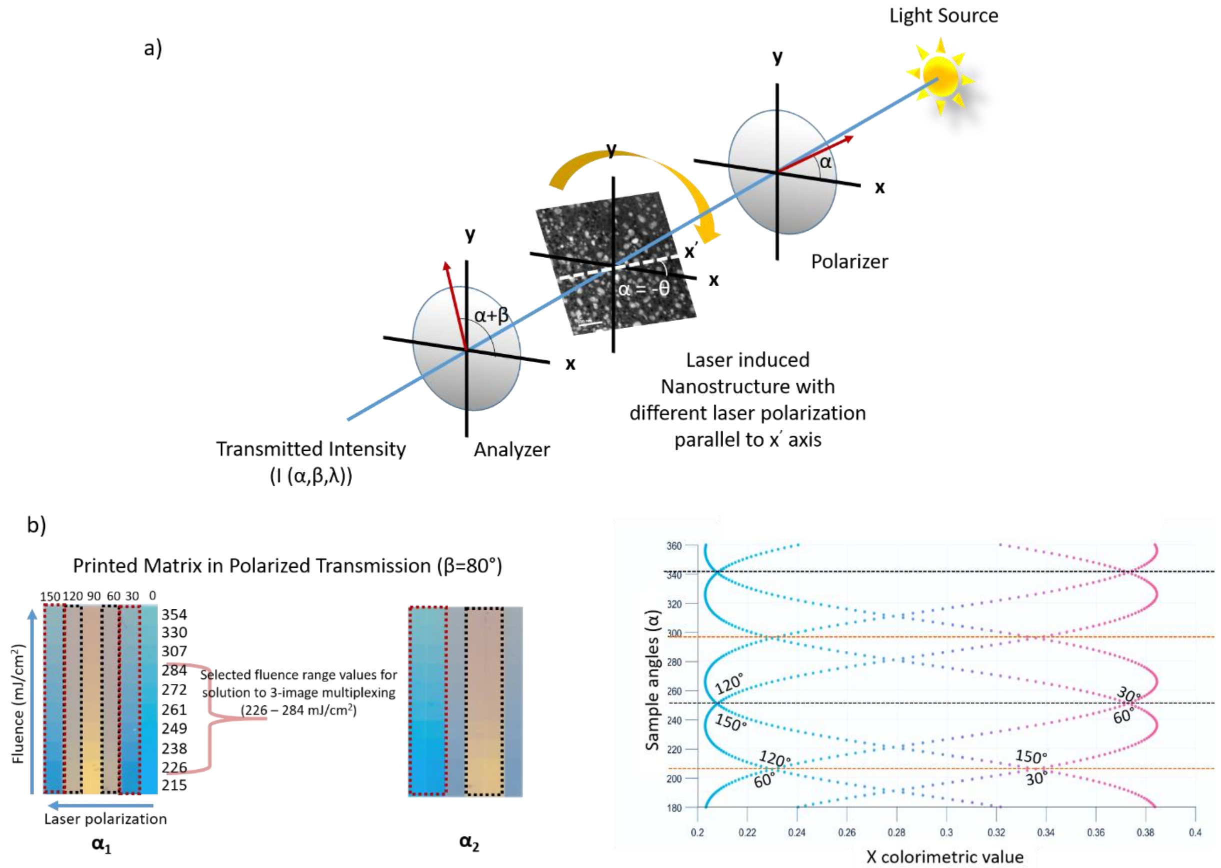

Figure V.13. a) Illustration showing setting up of neutral axis, when the sample is printed with laser polarization θ paralle to x′. The sample has to be rotated at α=- θ between two polarizers as to make the sample behave as if it is printed with polarization θ= 0° b) illustrates the colour variation with the rotation of angle α for a single nanostructure printed with a fluence of 249 mJ/cm^2, laser polarizations along the x axis, scan speed of 7 mm/s and a dy 15 μm. The curves intersects two different values of α. The first value for α_1 for which colours for 30° and 150° will be similar (red dashed rectangle) and colours of 60° - 120° will be similar (black dashed rectangle) and similar colour combination is achieved for α_2 for 30° - 60° and 120° - 150° respectively.

Interestingly, these curves intersect two by two for two different values of α. There is a first value of α where the colour of squares 60° matches the one of square 120° indicated by black dashed rectangle and the colour of square 30° matches the colour of square 150° indicated by red dashed rectangle in the Figure V.13b. For another value of α, the pairs of colours are for 30° - 60° and 120° - 150°. This is exactly what we need to add a third image in the multiplexing, as shown with the matrix images of Figure V.11 in observation modes where α has the right values to get the same sequence of colours as the ones described earlier and deduced from the logical graphs in section 3.2. Using the parameters shown in Figure V.11, a multiplexed image containing the information of three images can be encoded.

For each pixel of the encoded image, the laser fluence encodes the grey level of image 1 that is displayed in reflection (Figure V.14). Grey levels can be used in this mode with a linear variation of the fluence in the same range as the one used for 2-image multiplexing. Then the polarization is used to encode simultaneously images 2 and 3, which will be displayed in the polarized transmission mode for two different values of α. The methodology is the same as the one used for encoding a multiplexed image for 2 bicolour images . To satisfy these conditions, one needs a colour yellow and blue in image 2 and 3, 30° for yellow-blue, 60° for yellow-yellow, 120° for blue-yellow and 150° for blue-blue as observed in matrix in the Figure V.15.

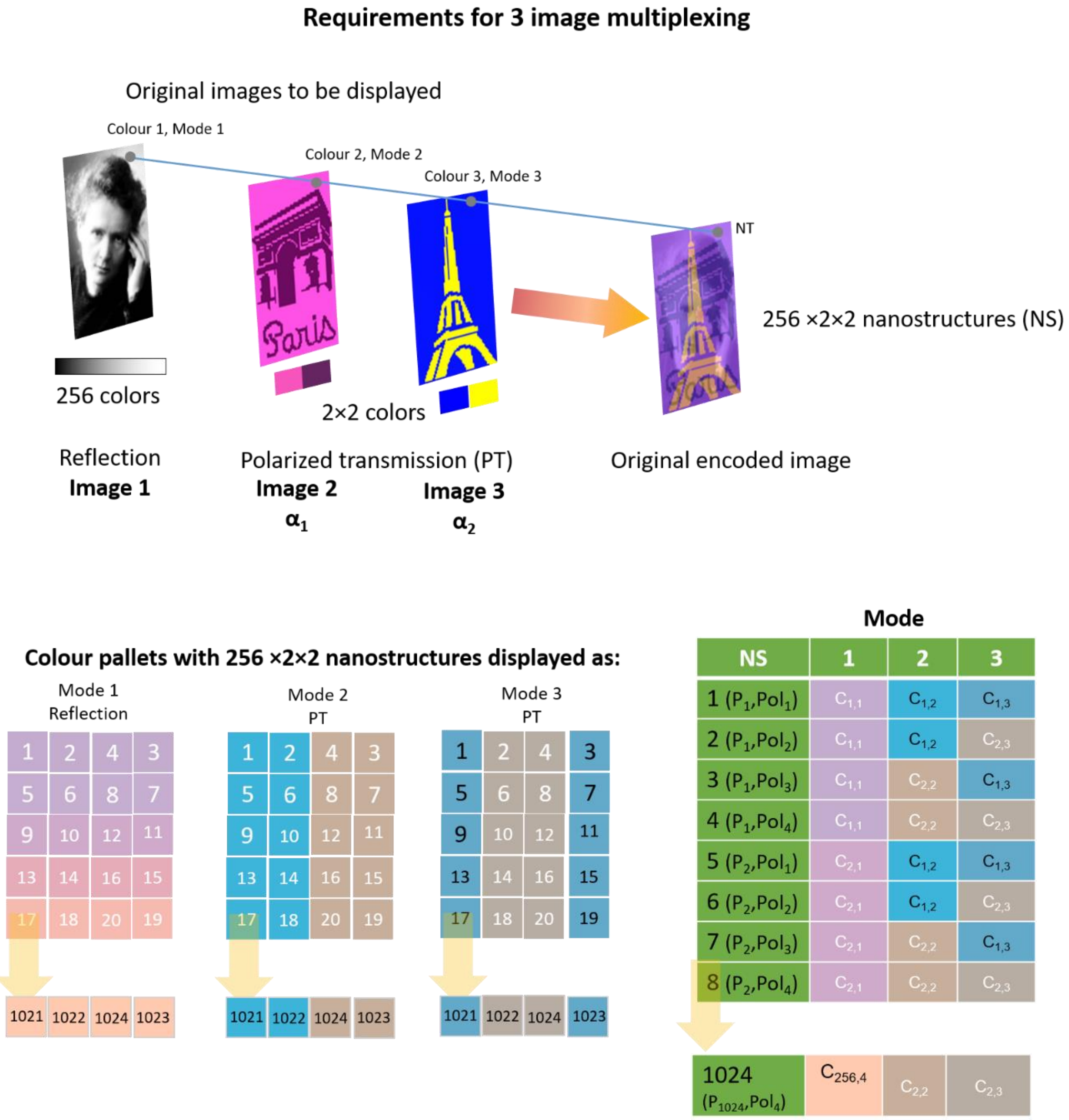

NS	1	2	3
1 (P_1,Pol_1)	$C_{1,1}$	$C_{1,2}$	$C_{1,3}$
2 (P_1,Pol_2)	$C_{1,1}$	$C_{1,2}$	$C_{2,3}$
3 (P_1,Pol_3)	$C_{1,1}$	$C_{2,2}$	$C_{1,3}$
4 (P_1,Pol_4)	$C_{1,1}$	$C_{2,2}$	$C_{2,3}$
5 (P_2,Pol_1)	$C_{2,1}$	$C_{1,2}$	$C_{1,3}$
6 (P_2,Pol_2)	$C_{2,1}$	$C_{1,2}$	$C_{2,3}$
7 (P_2,Pol_3)	$C_{2,1}$	$C_{2,2}$	$C_{1,3}$
8 (P_2,Pol_4)	$C_{2,1}$	$C_{2,2}$	$C_{2,3}$
1024 (P_{1024},Pol_4)	$C_{256,4}$	$C_{2,2}$	$C_{2,3}$

Figure V.14: a) Requirements for producing three image multiplexing that requires a production of colour pallet with 256 × 2 × 2 nanostructures to be able to display pallets in Mode 1 for reflection and mode 2 and 3 for polarized transmission for different samples angles α and angle β.

Figure V.15 illustrates a three image multiplexing printed on flexible glass using laser fluences from 226 to 284 mJ/cm^2 and laser polarization values of 30,60,120 and 150°, where the image in reflection (Mode 1) was chosen for laser fluence as a linear combination for the greyscale values of the image, while for Mode 2 under polarized transmission, a bi-colour image was chosen for two specific laser polarization each. Figure V.15a illustrates the image of Marie Curie, in reflection along with the matrix printed using laser, while Figure V.15b illustrates the modes in polarized transmission depicting Eiffel Tower for Mode 2 and for sample angle α_1 and Arc de Triomphe for Mode 3 again in polarized transmission for sample angle α_2.

This results is the first 3-image multiplexing demonstrated on printed images observed under white light combining reflection and transmission modes and that uses laser processing to print the multiplexed image in a single passage in a single film, which is so thin that is can be considered as a metasurface.

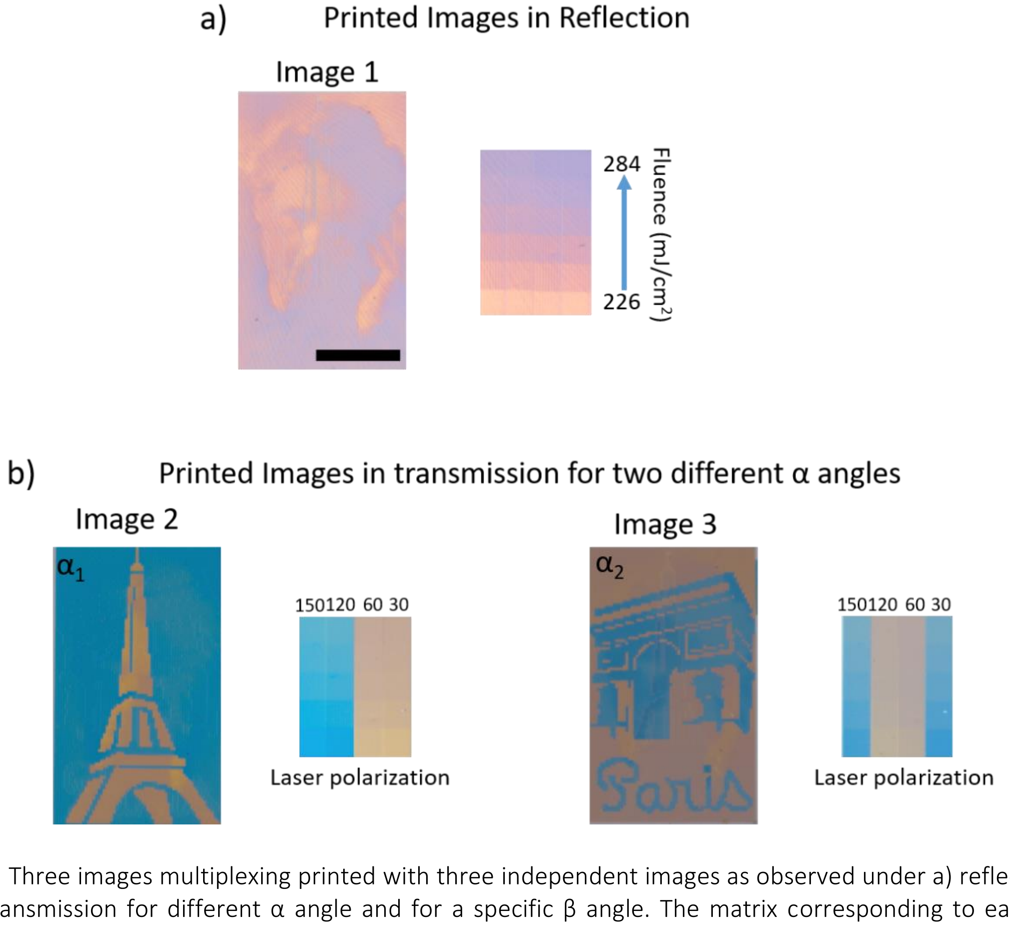

Figure V.15: Three images multiplexing printed with three independent images as observed under a) reflection and polarized transmission for different α angle and for a specific β angle. The matrix corresponding to each image corresponds to the variation in the laser fluence and the different laser polarization chosen for printing the encoded image. The scale bar corresponds to 4 mm for the image.

This brings us to the end of this thesis, and this chapter which demonstrates smart printing of multidimensional colours using laser technology and nanocomposite thin films of Ag:TiO_2, while such a technology can be useful to print multiple encoded images onto the same area.

5. Conclusions

This chapter demonstrates a distinctive technology to produce three-image multiplexing on flexible substrate coated with nanocomposite films using ultrashort pulsed laser. The nanocomposite thin films containing anisotropic metallic nanoparticles can be used to print an encoded image that contains the information of three independent images, which are revealed in non-polarized reflection and in polarized transmission using two different polarization angles. The proposed method can be applied to different nanoparticle shapes and implemented with different technologies. The demonstration is illustrated here by laser process, which allows printing centimeter scale images observable by eye. The versatile technology can encode any kind of images over large areas that can be printed on any sort of transparent substrate. This approach also enables to print images with different combinations of observation modes giving rise to multiplexing and artistic images as well. A fs laser grows and shapes metallic nanoparticles at the same time tuning the size distribution and the spatial distribution of these nanoparticles in the film. The laser process results in the generation of micrometer size plasmonic nanostructured areas where the film birefringence and dichroism can be controlled at will, to produce unprecedented colour gamuts that satisfy conditions for three- and two-image multiplexing in different selected modes of observation. Each nanostructured area is characterized by a set of colours corresponding to the colours exhibited in each selected mode. The conditions that the colour gamuts in the two and three modes must fulfil to produce two and three-fold image multiplexing were further explained and illustrated how such conditions can be satisfied with multidimensional colours. The physical parameters leading to such dichroic plasmonic colours were accompanied with the optical characterization using SEM and STEM microscopy. Such a technology can pave way for encoding information over a large area that can be used for anti-counterfeiting, security and data storage over flexible transparent substrates for the industrial applications.

CHAPTER VI

GENERAL CONCLUSIONS AND PERSPECTIVES

The first part of the thesis starting from chapter second, discusses about a facile and rapid synthesis sol-gel route used to produce mesoporous semi-crystalized TiO_2 optical thin films starting from low temperature using hydrolytic route. A comparison between seeded and unseeded films gives an overview of the film behavior with respect to the thermal annealing. Further, first values of activation energies in mesoporous TiO_2 thin films are reported, and it is inferred that the presence of crystal seeds (weakly complexed with organic compounds and homogeneously dispersed in the amorphous TiO_2 phase), as well as the high atomic diffusion provided by the porous structure, significantly lower the activation energy and lead to a more stable anatase phase above 700°C. Such films with tunable crystal content and porosity can be used for the applications to photocatalysis, photovoltaics and other applications where tuning porosity and crystallinity is essential.

The second part of the thesis starting from the third chapter, demonstrates the fabrication of different nanocomposite structures using a facile and controlled fs laser scanning technique, triggering growth and self-organization of Ag nanoparticles inside porous (amorphous) TiO_2 matrix giving rise to plasmonic dichroic colours. Adjusting the laser scan speed (number of effective pulse), such nanocomposites can be selectively formed either at the surface or imbedded inside the film to form grating structures. Excitation of a surface mode in form of surface plasmon polaritons is possible due to the high density of small nanoparticles in the initial film and the transient effects induced by the ultrashort laser pulse. This way, LIPSS are formed at higher scan speed, whereas at lower speeds nanoparticle organization is governed by the excitation of a guided mode inside the film; thus yielding different nanostructures with tunable dichroic colours at different laser scan speeds. Dichroism is found to be caused by the presence of the different grating structures for high and low scan speeds, as well as by the shape anisotropy of the nanoparticles induced at intermediate scan speeds.

The fourth chapter deals with the first application of such laser processing including multiple hidden images imprinting on flexible plastic substrates. Here, the issue of laser-induced thermal effects are countered, that are serious limitations for plastics processing and provides conditions optimizing the nanoparticle growth and self-organization in the nanocomposite film while preventing the film spallation and the substrate damage. Employing a continuous control of laser polarization orientation, the grating orientation (LIPSS) is modulated to provide a grey-scale variation of the diffracted intensity in given observation directions. The three image frames are interlaced to create a single encoded image whose appearance is fully homogeneous in transmission and reflection. While such imprinting on the nanocomposite deposited on glass gives a higher resolution, due to high thermal stability of the substrates.

Moving further, the thesis discusses the second application about multiplexing images on such nanocomposites deposited on flexible glass substrate. A combination of fs laser process and nanocomposite thin films of Ag:TiO_2 results in the generation of micrometer size plasmonic nanostructured areas, where the film birefringence and dichroism can be controlled at will, to produce colour matrix that satisfy conditions for two and three image multiplexing in different selected modes of observation under white light: reflection under non-polarized light and transmission between polarizers for different polarization angles. These nanostructures are a result of growth, shape anisotropy of the nanoparticles and self-organization processes. Further, the expression of the intensity transmitted by a dichroic and birefringent sample placed between two polarizers is formulated and it is shown to describe quite well the spectral behavior of the sample birefringence and dichroism. This expression is used to predict solutions for multiplexing in the polarized transmission mode between two polarizers. This facile technology paves way to find a solution to encode up to three images onto the same area with other technologies and materials.

Although the thesis gives an overall view on optical thin films produced using facile acid assisted sol-gel processes and using fs laser processes to fabricate nanostructures giving rise to dichroic plasmonic colours for applications to hidden diffractive images on plastic and image multiplexing, following investigations can be the future prospective for the current work:

- Crystallized thin films: Such fine-tuned optical thin films with varying crystallite and porosity content offer promising perspectives of applications in photocatalysis specially when doped with noble metals on different substrates according to varying crystallinity and porosity
- The broad range of nanostructures fabricated using such fs system can be fabricated using ns laser system with faster writing processes that can give rise to more than three image multiplexing. Other modes of observation, including scattering, diffraction can be tested
- Such image multiplexing can pave way for security for encoding information using system comprising of an industrialized laser and easy to fabricate nanocomposite thin films

ANNEXURE 1

From chapter V, section 4.3, the intensity transmitted from a dichroic nanostructured sample placed between two polarizers under normal incidence, is given by:

$$I(\alpha,\beta,\lambda) = \left|E_0 cos(\alpha) t_x(\lambda) e^{i\varphi_x(\lambda)} cos(\alpha+\beta) + E_0 sin(\alpha) t_y(\lambda) e^{i\varphi_y(\lambda)} sin(\alpha+\beta)\right|^2$$

(Eq. A1.1)

Or,

$$I(\alpha,\beta,\lambda) = {E_0}^2[cos^2(\alpha)cos^2(\alpha+\beta)t_x^2(\lambda) + sin^2(\alpha)sin^2(\alpha+\beta)t_y^2(\lambda) + \frac{1}{2}sin(2\alpha)sin(2\alpha+2\beta)t_x(\lambda)t_y(\lambda)\cos(\varphi_x-\varphi_y)]$$

(Eq. A1.2)

Now, putting the values $\alpha = 0, \frac{\pi}{4}, and \frac{\pi}{2}$ individually in the Eq. A1.2 we get,

$$I(0,\beta,\lambda) = {E_0}^2 cos^2(\beta) t_x^2(\lambda) \quad \text{(Eq. A1.3)}$$

$$I\left(\frac{\pi}{4},\beta,\lambda\right) = \frac{{E_0}^2}{2}[cos^2\left(\frac{\pi}{4}+\beta\right)t_x^2(\lambda) + sin^2\left(\frac{\pi}{4}+\beta\right)t_y^2(\lambda) + cos(2\beta)t_x(\lambda)t_y(\lambda)\cos(\varphi_x-\varphi_y)]$$

(Eq. A1.4)

$$I\left(\frac{\pi}{2},\beta,\lambda\right) = {E_0}^2 cos^2(\beta) t_y^2(\lambda) \quad \text{(Eq. A1.5)}$$

Using (Eq.A1.3) and (Eq.A1.5) we get, respectively :

$${E_0}^2 t_x^2(\lambda) = \frac{I(0,\beta,\lambda)}{cos^2(\beta)} \quad \text{(Eq. A1.6)}$$

$${E_0}^2 t_y^2(\lambda) = \frac{I\left(\frac{\pi}{2},\beta,\lambda\right)}{cos^2(\beta)} \quad \text{(Eq. A1.7)}$$

And from (Eq. A1.6), (Eq. A1.7) and (Eq. A1.4) we deduce :

$$E_0{}^2 t_x(\lambda) t_y(\lambda) \cos(\varphi_x - \varphi_y)$$

$$= I\left(\frac{\pi}{4}, \beta, \lambda\right) \frac{2}{cos(2\beta)} - I(0, \beta, \lambda) \frac{cos^2\left(\frac{\pi}{4} + \beta\right)}{cos(2\beta) cos^2(\beta)}$$

$$- I\left(\frac{\pi}{2}, \beta, \lambda\right) \frac{sin^2\left(\frac{\pi}{4} + \beta\right)}{cos(2\beta) cos^2(\beta)}$$

(Eq. A1.8)

Now using (Eq.A1.6), (Eq.A1.7), and (Eq.A1.8) in (Eq. A1.2), we get,

$$I(\alpha, \beta, \lambda) = I(0, \beta, \lambda)\left[\frac{cos^2(\alpha) cos^2(\alpha + \beta)}{cos^2(\beta)} - \frac{cos^2\left(\frac{\pi}{4} + \beta\right) sin(2\alpha) sin(2\alpha + 2\beta)}{2cos^2(\beta) cos(2\beta)}\right]$$

$$+ I\left(\frac{\pi}{4}, \beta, \lambda\right) \frac{sin(2\alpha) sin(2\alpha + 2\beta)}{cos(2\beta)}$$

$$+ I\left(\frac{\pi}{2}, \beta, \lambda\right)\left[\frac{sin^2(\alpha) sin^2(\alpha + \beta)}{cos^2(\beta)} - \frac{sin^2\left(\frac{\pi}{4} + \beta\right) sin(2\alpha) sin(2\alpha + 2\beta)}{2cos^2(\beta) cos(2\beta)}\right]$$

(Eq. A1.9)

ANNEXURE 2

For a given reflectance or transmittance spectrum f_λ at a certain illuminance g_λ (example D65 illuminant), the CIE colour matching function is given by $\bar{x}_\lambda,\ \bar{y}_\lambda, \text{and } \bar{z}_\lambda$.

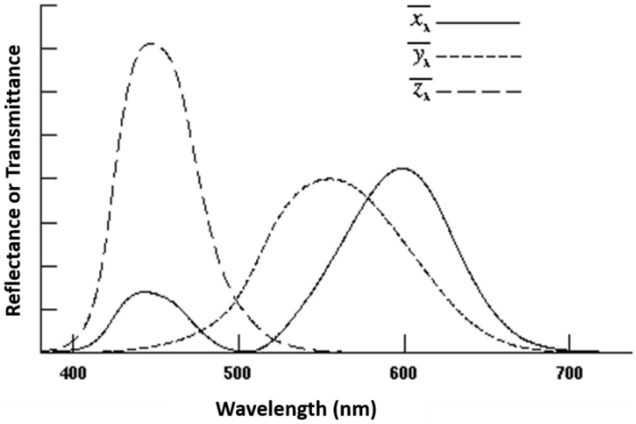

Figure A2.1: CIE colour matching functions $\bar{x}_\lambda,\ \bar{y}_\lambda, and\ \bar{z}_\lambda$.

The CIE *X, Y, Z* coordinates are thus, calculated as:[173,174]

$$X = \frac{k}{N}\int\ g_\lambda f_\lambda \bar{x}_\lambda d\lambda \qquad \text{(Eq. A2.1)}$$

$$\mathrm{Y} = \frac{k}{N}\int\ g_\lambda f_\lambda \bar{y}_\lambda \mathrm{d}\lambda \qquad \text{(Eq. A2.2)}$$

$$X = \frac{k}{N}\int\ g_\lambda f_\lambda \bar{z}_\lambda \mathrm{d}\lambda \qquad \text{(Eq. A2.3)}$$

where *k* is the scaling factor (100), $\bar{x}_\lambda,\ \bar{y}_\lambda, and\ \bar{z}_\lambda$ are the chromatic response of observer, and $N = \int\ g_\lambda \bar{y}_\lambda d\lambda$

REFERENCES

(1) Roduner, E. Size Matters: Why Nanomaterials Are Different. *Chem. Soc. Rev.* **2006**, *35* (7), 583–592.

(2) Dong, L.; Craig, M. M.; Khang, D.; Chen, C. Applications of Nanomaterials in Biology and Medicine. *J. Nanotechnol.* **2012**, *2012*, 2012–2014.

(3) *Nanoscale Science and Technology*; Kelsall, R. W., Hamley, I. W., Geoghehan, M., Eds.; John Wiley & Sons, Ltd, 2005.

(4) Suib, S. L. A Review of Recent Developments of Mesoporous Materials. *Chem. Rec.* **2017**, *17*, 1–16.

(5) Linares, N.; Silvestre-Albero, A. M.; Serrano, E.; Silvestre-Albero, J.; García-Martínez, J. Mesoporous Materials for Clean Energy Technologies. *Chem. Soc. Rev.* **2014**, *43*, 7681–7717.

(6) Li, W.; Liu, J.; Zhao, D. Mesoporous Materials for Energy Conversion and Storage Devices. *Nat. Rev. Mater.* **2016**, *1* (6).

(7) Murray, B. W. A.; Barnes, W. L. Plasmonic Materials **. *Adv. Mater.* **2007**, *19*, 3771–3782.

(8) Mock, J. J.; Barbic, M.; Smith, D. R.; Schultz, D. A.; Schultz, S. Shape Effects in Plasmon Resonance of Individual Colloidal Silver Nanoparticles. *J. Chem. Phys.* **2002**, *116* (15), 6755–6759.

(9) Kristensen, A.; Yang, J. K. W.; Bozhevolnyi, S. I.; Link, S.; Nordlander, P.; Halas, N. J.; Mortensen, N. A. Plasmonic Colour Generation. *Nat. Rev. Mater.* **2016**, *2* (1), 1–15.

(10) Barber, D. J.; Freestone, I. C. An Investigation of the Origin of the Color of the Lycurgus Cup By Analytical Transmission Electron-Microscopy. *Archaeometry* **1990**, *1* (32), 33–45.

(11) Kumar, K.; Duan, H.; Hegde, R. S.; Koh, S. C. W.; Wei, J. N.; Yang, J. K. W. Printing Colour at the Optical Diffraction Limit. *Nat. Nanotechnol.* **2012**, *7* (9), 557–561.

(12) Mayer, K. M.; Hafner, J. H. Localized Surface Plasmon Resonance Sensors. *Chem. Rev.* **2011**, *111*, 3828–3857.

(13) Lee, J. H.; Cho, H. Y.; Choi, H. K.; Lee, J. Y.; Choi, J. W. Application of Gold Nanoparticle to Plasmonic Biosensors. *Int. J. Mol. Sci.* **2018**, *19* (7).

(14) Kaempfe, M.; Rainer, T.; Berg, K.; Seifert, G.; Graener, H. Ultrashort Laser Pulse Induced Deformation of Silver Nanoparticles in Glass. *Appl. Phys. Lett.* **1999**, *74* (9), 1200–1202.

(15) Seifert, G.; Stalmashonak, A.; Hofmeister, H.; Haug, J.; Dubiel, M. Laser-Induced, Polarization Dependent Shape Transformation of Au/Ag Nanoparticles in Glass. *Nanoscale Res. Lett.* **2009**, *4* (11), 1380–1383.

(16) Loeschner, K.; Seifert, G.; Heilmann, A. Self-Organized, Gratinglike Nanostructures in Polymer Films with Embedded Metal Nanoparticles Induced by Femtosecond Laser Irradiation. *J. Appl. Phys.* **2010**, *108* (7), 073114.

(17) Destouches, N.; Martínez-garcía, J.; Hébert, M.; Crespo-monteiro, N.; Vitrant, G.; Liu, Z.; Trémeau, A.; Vocanson, F.; Pigeon, F.; Reynaud, S.; et al. Dichroic Colored Luster of Laser-Induced Silver Nanoparticle Gratings Buried in Dense Inorganic Films. *J. Opt. Soc. Am. B* **2014**, *31* (11), 1–7.

(18) Liu, Z.; Siegel, J.; Garcia-Lechuga, M.; Epicier, T.; Lefkir, Y.; Reynaud, S.; Bugnet, M.; Vocanson, F.; Solis, J.; Vitrant, G.; et al. Three-Dimensional Self-Organization in Nanocomposite Layered Systems by Ultrafast Laser Pulses. *ACS Nano* **2017**, *11* (5), 5031–5040.

(19) Fujishima, A.; Honda, K. Electrochemical Photolysis of Water at a Semiconductor Electrode. *Nature* **1972**, *238*, 37–38.

(20) Grätzel, M. Mesoporous Oxide Junctions and Nanostructured Solar Cells. *Curr. Opin. Colloid Interface Sci.* **1999**, *4* (4), 314–321.

(21) Elgh, B.; Yuan, N.; Cho, H. S.; Magerl, D.; Philipp, M.; Roth, S. V.; Yoon, K. B.; Müller-Buschbaum, P.; Terasaki, O.; Palmqvist, A. E. C. Controlling Morphology, Mesoporosity, Crystallinity, and Photocatalytic Activity of Ordered Mesoporous TiO_2 Films Prepared at Low Temperature. *APL Mater.* **2014**, *2* (11), 1–13.

(22) Farrokhpay, S.; Morris, G. E.; Fornasiero, D.; Self, P. Titania Pigment Particles Dispersion in Water-Based Paint Films. *J. Coatings Technol. Res.* **2006**, *3* (4), 275–283.

(23) Guan, X.; Hu, H.; Oxenløwe, L. K.; Frandsen, L. H. Compact Titanium Dioxide Waveguides with High Nonlinearity at Telecommunication Wavelengths. *Opt. Express* **2018**, *26* (2), 1055.

(24) Tang, H.; Prasad, K.; Sanjinés, R.; Lévy, F. TiO_2 Anatase Thin Films as Gas Sensors. *Sensors Actuators B* **1995**, No. 26–27, 71–75.

(25) Dambournet, D.; Belharouak, I.; Amine, K. Tailored Preparation Methods of TiO_2 Anatase, Rutile, Brookite: Mechanism of Formation and Electrochemical Properties. *Chem. Mater.* **2010**, *22* (3), 1173–1179.

(26) Li, J. G.; Ishigaki, T. Brookite → Rutile Phase Transformation of TiO_2 Studied with Monodispersed Particles. *Acta Mater.* **2004**, *52* (17), 5143–5150.

(27) Hanaor, D. A. H.; Sorrell, C. C. Review of the Anatase to Rutile Phase Transformation. *J. Mater. Sci.* **2011**, *46* (4), 855–874.

(28) Dieter Mergel, D. M.; Martin Jerman, and M. J. Density and Refractive Index of Thin Evaporated Films. *Chinese Opt. Lett.* **2010**, *8* (S1), 67–72.

(29) Bendavid, A.; Martin, P. J. Review of Thin Film Materials Deposition by the Filtered Cathodic Vacuum Arc Process at CSIRO. *J. Aust. Ceram. Soc.* **2014**, *50* (1), 86–101.

(30) Evans, C. C.; Liu, C.; Suntivich, J. Low-Loss Titanium Dioxide Waveguides and Resonators Using a Dielectric Lift-off Fabrication Process. *Opt. Express* **2015**, *23* (9), 11160–11169.

(31) Jayasinghe, R. C.; Perera, A. G. U.; Zhu, H.; Zhao, Y. Optical Properties of Nanostructured TiO_2 Thin Films and Their Application as Antireflection Coatings on Infrared Detectors. *Opt. Lett.* **2012**, *37* (20), 4302.

(32) Bai, J.; Zhou, B. Titanium Dioxide Nanomaterials for Sensor Applications. *Chem. Rev.* **2014**, *114* (19), 10095–10130.

(33) Kresge, C. T.; Leonowicz, M. E.; Roth, W. J.; Vartuli, J. C.; Beck, J. S. Ordered Mesoporous Molecular Sieves Synthesized by a Liquid-Crystal Template Mechanism. *Lett. to Nat.* **1992**, *359*, 710–712.

(34) Antonelli, D. M.; Ying, J. Y. Synthesis of Hexagonally Packed Mesoporous TiO_2 by a Modified Sol-Gel Method. *Angew. Chem. Int. Ed* **1995**, *34*, 2014–2017.

(35) Li, W.; Wu, Z.; Wang, J.; Elzatahry, A. A.; Zhao, D. A Perspective on Mesoporous TiO_2 Materials. *Chem. Mater.* **2014**, *26* (1), 287–298.

(36) Machado, A. E. H.; Borges, K. A.; Tatiana, A. S.; Santos, L. M.; Borges, M. F.; Machado, W. A.; França, M. D.; Oliveira, S. M.; Trovó, A. G.; Patrocínio, A. O. T.; et al. Applications of Mesoporous Ordered Semiconductor Materials — Case Study of TiO_2. In *Intech*; 2015; pp 87–118.

(37) Zhang, R.; Elzatahry, A. A.; Al-Deyab, S. S.; Zhao, D. Mesoporous Titania: From Synthesis to Application. *Nano Today* **2012**, *7* (4), 344–366.

(38) Grosso, D.; Soler-Illia, G. J. A. A.; Babonneau, F.; Sanchez, C.; Albouy, P.-A.; Brunet-Bruneau, A.; Balkenende, A. R. Highly Organized Mesoporous Titania Thin Films Showing Mono-Oriented 2D Hexagonal Channels. *Adv. Mater.* **2001**, *13* (14), 1085–1090.

(39) Hwang, Y. K.; Kwon, Y.-U.; Lee, K.-C. Nanoparticle Routes to Mesoporous Titania Thin Films. *Chem. Commun.* **2001**, No. 18, 1738–1739.

(40) Yun, H.; Miyazawa, K.; Zhou, H.; Honma, I.; Kuwabara, M. Synthesis of Mesoporous Thin TiO_2 Films with Hexagonal Pore Structures Using Triblock Copolymer Templates. *Adv. Mater.* **2001**, *13* (18), 1377–1380.

(41) Raut, H. K.; Ganesh, V. A.; Nair, A. S.; Ramakrishna, S. Anti-Reflective Coatings: A Critical, in-Depth Review. *Energy Environ. Sci.* **2011**, *4* (10), 3779–3804.

(42) Ossila. Spin Coating: Complete Guide to Theory and Techniques https://www.ossila.com/pages/spin-coating#spin-coating-general-theory.

(43) Faustini, M.; Louis, B.; Albouy, P. A.; Kuemmel, M.; Grosso, D. Preparation of Sol - Gel Films by Dip-Coating in Extreme Conditions. *J. Phys. Chem. C* **2010**, *114* (17), 7637–7645.

(44) Hou, K.; Tian, B.; Li, F.; Bian, Z.; Zhao, D.; Huang, C. Highly Crystallized Mesoporous TiO_2 Films and Their Applications in Dye Sensitized Solar Cells. *J. Mater. Chem.* **2005**, *15* (24), 2414.

(45) Zhou, W.; Fu, H. Mesoporous TiO_2: Preparation, Doping, and as a Composite for Photocatalysis. *ChemCatChem* **2013**, *5* (4), 885–894.

(46) Li, C.; Colella, N. S.; Watkins, J. J. Low-Temperature Fabrication of Mesoporous Titanium Dioxide Thin Films with Tunable Refractive Indices for One-Dimensional Photonic Crystals and Sensors on Rigid and Flexible Substrates. *ACS Appl. Mater. Interfaces* **2015**, *7* (24), 13180–13188.

(47) Ortiz, G. F.; Berenguer-Murcia, Á.; Cabello, M.; Cazorla-Amorós, D.; Tirado, J. L. Ordered Mesoporous

Titanium Oxide for Thin Film Microbatteries with Enhanced Lithium Storage. *Electrochim. Acta* **2015**, *166*, 293–301.

(48) Miller, L. W.; Tejedor, M. I.; Nelson, B. P.; Anderson, M. A. Mesoporous Metal Oxide Semiconductor-Clad Waveguides. *J. Phys. Chem. B* **1999**, *103* (40), 8490–8492.

(49) Crespo-Monteiro, N.; Destouches, N.; Bois, L.; Chassagneux, F.; Reynaud, S.; Fournel, T. Reversible and Irreversible Laser Microinscription on Silver-Containing Mesoporous Titania Films. *Adv. Mater.* **2010**, *22*, 3166–3170.

(50) Hernández-Granados, A.; Corpus-Mendoza, A. N.; Moreno-Romero, P. M.; Rodríguez-Castañeda, C. A.; Pascoe-Sussoni, J. E.; Castelo-González, O. A.; Menchaca-Campos, E. C.; Escorcia-García, J.; Hu, H. Optically Uniform Thin Films of Mesoporous TiO_2 for Perovskite Solar Cell Applications. *Opt. Mater. (Amst).* **2019**, *88* (August 2018), 695–703.

(51) Scarpelli, F.; Mastropietro, T. F.; Poerio, T.; Godbert, N. Mesoporous TiO_2 Thin Films: State of the Art. In *Titanium Dioxide - Material for a Sustainable Environment*; 2018.

(52) Hossain, M. K.; Kitahama, Y.; Huang, G. G.; Han, X.; Ozaki, Y. Surface-Enhanced Raman Scattering: Realization of Localized Surface Plasmon Resonance Using Unique Substrates and Methods. *Anal. Bioanal. Chem.* **2009**, *394* (7), 1747–1760.

(53) Juan, M. L.; Righini, M.; Quidant, R. Plasmon Nano-Optical Tweezers. *Nat. Photonics* **2011**, *5* (6), 349–356.

(54) Prabowo, B. A.; Purwidyantri, A.; Liu, K. C. Surface Plasmon Resonance Optical Sensor: A Review on Light Source Technology. *Biosensors* **2018**, *8*.

(55) Mie, G. Contributions on the Optics of Turbid Media, Particularly Colloidal Metal Solutions. *Ann. Phys.* **1908**, *25*, 377–445.

(56) Milton, G. W. Bounds on the Complex Permittivity of a Two-Component Composite Material. *J. Appl. Phys.* **1981**, *52* (8), 5286–5293.

(57) Draine, B. T.; Flatau, P. J. Discrete-Dipole Approximation For Scattering Calculations. *J. Opt. Soc. Am. A* **1994**, *11* (4), 1491.

(58) Bohren, C. F.-A.; Huffman, D. R. *Absorption and Scattering of Light by Small Particles*; Wiley-VCH, 1998.

(59) Rivera, V. A. G.; Ferri, F. A.; Marega Jr., E. Localized Surface Plasmon Resonances: Noble Metal Nanoparticle Interaction with Rare-Earth Ions. In *Plasmonic-Principle and Applications*; Young Kim, K., Ed.; Intech Open, 2012.

(60) Coronado, E. A.; Encina, E. R.; Stefani, F. D. Optical Properties of Metallic Nanoparticles: Manipulating Light, Heat and Forces at the Nanoscale. *Nanoscale* **2011**, *3* (10), 4042–4059.

(61) Sugiura, T.; Okada, T.; Inouye, Y.; Nakamura, O.; Kawata, S. Gold-Bead Scanning near-Field Optical Microscope with Laser-Force Position Control. *Opt. Lett.* **1997**, *22* (22), 1663.

(62) Guo, L.; Jackman, J. A.; Yang, H. H.; Chen, P.; Cho, N. J.; Kim, D. H. Strategies for Enhancing the Sensitivity of Plasmonic Nanosensors. *Nano Today* **2015**, *10* (2), 213–239.

(63) Bouas-Laurent, H.; Durr, H. ORGANIC PHOTOCHROMISM. *Pure Appl. Chem.* **2001**, *73* (4), 639–665.

(64) Sze, S. .; NG, K. K. *Physics of Semiconductor Devices*, third.; Wiley Interscience, 1981.

(65) Kawahara, K.; Suzuki, K.; Ohko, Y.; Tatsuma, T. Electron Transport in Silver-Semiconductor Nanocomposite Films Exhibiting Multicolor Photochromism. *Phys. Chem. Chem. Phys.* **2005**, *7* (22), 3851.

(66) Naoi, K.; Ohko, Y.; Tatsuma, T. TiO_2 Films Loaded with Silver Nanoparticles: Control of Multicolor Photochromic Behavior. *J. Am. Chem. Soc.* **2004**, *126* (11), 3664–3668.

(67) Ohko, Y.; Tatsuma, T.; Fujii, T.; Naoi, K.; Niwa, C.; Kubota, Y.; Fujishima, A. Multicolour Photochromism of TiO_2 Films Loaded with Silver Nanoparticles. *Nat. Mater.* **2003**, *2* (1), 29–31.

(68) Matsubara, K.; Tatsuma, T. Morphological Changes and Multicolor Photochromism of Ag Nanoparticles Deposited on Single-Crystalline TiO_2 Surfaces. *Adv. Mater.* **2007**, *19* (19), 2802–2806.

(69) Bois, L.; Chassagneux, F.; Battiez, Y.; Bessueille, F.; Mollet, L.; Parola, S.; Destouches, N.; Toulhoat, N.; Moncoffre, N. Chemical Growth and Photochromism of Silver Nanoparticles into a Mesoporous Titania Template. *Langmuir* **2010**, *26* (2), 1199–1206.

(70) Nadar, L.; Destouches, N.; Crespo-Monteiro, N.; Sayah, R.; Vocanson, F.; Reynaud, S.; Lefkir, Y.; Capoen, B. Multicolor Photochromism of Silver-Containing Mesoporous Films of Amorphous or Anatase TiO_2. *J. Nanoparticle Res.* **2013**, *15* (11), 2048.

(71) Tricot, F.; Vocanson, F.; Chaussy, D.; Beneventi, D.; Reynaud, S.; Lefkir, Y.; Destouches, N. Photochromic Ag:TiO_2 Thin Films on PET Substrate. *RSC Adv.* **2014**, *4* (106), 61305–61312.

(72) Destouches, N.; Crespo-monteiro, N.; Vitrant, G.; Lefkir, Y.; Reynaud, S.; Epicier, T.; Liu, Y.; Vocanson, F.; Pigeon, F. Self-Organized Growth of Metallic Nanoparticles in a Thin Film under Homogeneous and Continuous- Wave Light Excitation. *Mater. Chem. C* **2014**, *2* (31), 6256–6263.

(73) Liu, Z.; Destouches, N.; Vitrant, G.; Lefkir, Y.; Epicier, T.; Vocanson, F.; Bhakti, S.; Fang, Y.; Bandyopadhyay, B.; Ahmed, M. Understanding the Growth Mechanisms of Ag Nanoparticles Controlled by Plasmon-Induced Charge Transfers in Ag-TiO_2 Films. *J. Phys. Chem. C* **2015**.

(74) Liu, Z. Self-Organization of Metallic Nanoparticles in Waveguides by Laser: Mechanisms Modelling and New Approaches, Université Jean Monnet Saint-Etienne, 2016.

(75) Liu, Z.; Vitrant, G.; Lefkir, Y.; Bakhti, S.; Destouches, N. Laser Induced Mechanisms Controlling the Size Distribution of Metallic Nanoparticles. *Phys. Chem. Chem. Phys.* **2016**, *18* (35), 24600–24609.

(76) Baraldi, G.; Bhakti, S.; Liu, Z.; Reynaud, S.; Lefkir, Y.; Vocanson, F.; Destouches, N. Polarization-Driven Self-Organization of Silver Nanoparticles in 1D and 2D Subwavelength Gratings for Plasmonic Photocatalysis. *Nanotechnology* **2017**, *28*, 035302:10.

(77) Diels, J.-C.; Rudolph, W. *Ultrashort Laser Pulse Phenomena Fundamentals, Techniques, and Applications on*

a *Femtosecond Time Scale*, Second.; Elsevier: UK, 2005.

(78) Baffou, G.; Rigneault, H. Femtosecond-Pulsed Optical Heating of Gold Nanoparticles. *Phys. Rev. B - Condens. Matter Mater. Phys.* **2011**, *84* (3), 1–13.

(79) Kohn, P.; Pathak, S.; Stefik, M.; Ducati, C.; Wiesner, U.; Steiner, U.; Guldin, S. Low Temperature Crystallisation of Mesoporous TiO_2. *Nanoscale* **2013**, *5* (21), 10518–10524.

(80) Zhang, H.; Banfield, J. F. Kinetics of Crystallization and Crystal Growth of Nanocrystalline Anatase in Nanometer-Sized Amorphous Titania. *Chem. Mater.* **2002**, *14* (10), 4145–4154.

(81) Tricot, F.; Vocanson, F.; Chaussy, D.; Beneventi, D.; Party, M.; Destouches, N. Flexible Photochromic Ag:TiO_2 Thin Films Fabricated by Ink-Jet and Flexography Printing Processes. *RSC Adv.* **2015**, *5* (103), 84560–84564.

(82) Tricot, F. Films Reinscriptibles Sur Support Souples, L'Universite jean Monent De Saint-Etienne, 2016.

(83) Schneider, J.; Matsuoka, M.; Takeuchi, M.; Zhang, J.; Horiuchi, Y.; Anpo, M.; Bahnemann, D. W. Understanding TiO_2 Photocatalysis: Mechanisms and Materials. *Chem. Rev.* **2014**, *114* (19), 9919–9986.

(84) Schulze, P. S. C.; Bett, A. J.; Winkler, K.; Hinsch, A.; Lee, S.; Mastroianni, S.; Mundt, L. E.; Mundus, M.; Würfel, U.; Glunz, S. W.; et al. Novel Low-Temperature Process for Perovskite Solar Cells with a Mesoporous TiO_2 Scaffold. *ACS Appl. Mater. Interfaces* **2017**, *9* (36), 30567–30574.

(85) Cedillo-González, E. I.; Riccò, R.; Montorsi, M.; Montorsi, M.; Falcaro, P.; Siligardi, C. Self-Cleaning Glass Prepared from a Commercial TiO_2 Nano-Dispersion and Its Photocatalytic Performance under Common Anthropogenic and Atmospheric Factors. *Build. Environ.* **2014**, *71*, 7–14.

(86) Dette, C.; Pérez-Osorio, M. A.; Kley, C. S.; Punke, P.; Patrick, C. E.; Jacobson, P.; Giustino, F.; Jung, S. J.; Kern, K. TiO_2 Anatase with a Bandgap in the Visible Region. *Nano Lett.* **2014**, *14* (11), 6533–6538.

(87) Vinogradov, V. V.; Agafonov, A. V.; Vinogradov, A. V. A New Approach to Apply Crystalline Titania Hydrosols onto a Polyester Cloth. *Mendeleev Commun.* **2013**, *23* (5), 286–288.

(88) Zhang, D.; Qi, L.; Ma, J.; Cheng, H. Formation of Crystalline Nanosized Titania in Reverse Micelles at Room Temperature. *J. Mater. Chem.* **2002**, *12* (12), 3677–3680.

(89) Qi, K.; Xin, J. H. Room-Temperature Synthesis of Single-Phase Anatase TiO_2 by Aging and Its Self-Cleaning Properties. *ACS Appl. Mater. Interfaces* **2010**, *2* (12), 3479–3485.

(90) Liu, X.; Fechler, N.; Antonietti, M. Salt Melt Synthesis of Ceramics, Semiconductors and Carbon Nanostructures. *Chem. Soc. Rev.* **2013**, *42* (21), 8237–8265.

(91) Gopal, M.; Moberly Chan, W. J.; De Jonghe, L. C. Room Temperature Synthesis of Crystalline Metal Oxides. *J. Mater. Sci.* **1997**, *32*, 6001–6008.

(92) Zhang, X.; Yao, J.; Ali, M.; Wei, J.; Wang, H.; Yeo, L. Y.; Friend, J. R.; MacFarlane, D. R. UV/Ozone-Assisted Low Temperature Preparation of Mesoporous TiO_2 with Tunable Phase Composition and Enhanced Solar Light Photocatalytic Activity. *J. Mater. Chem. A* **2014**, *2* (44), 18791–18795.

(93) Angelome, P. C.; Andrini, L.; Calvo, M. E.; Requejo, F. G.; Sara, B. A.; Soler-Illia, G. J. A. A. Mesoporous Anatase TiO_2 Films: Use of Ti K XANES for the Quantification of the Nanocrystalline Character and Substrate Effects

in the Photocatalysis Behavior. *J. Phys. Chem. C* **2007**, *111*, 10886–10893.

(94) Crespo-Monteiro, N.; Destouches, N.; Nadar, L.; Reynaud, S.; Vocanson, F.; Michalon, J. Y. Irradiance Influence on the Multicolor Photochromism of Mesoporous TiO_2 Films Loaded with Silver Nanoparticles. *Appl. Phys. Lett.* **2011**, *99*, 173106.

(95) Nadar, L.; Sayah, R.; Vocanson, F.; Crespo-Monteiro, N.; Boukenter, A.; Sao Joao, S.; Destouches, N. Influence of Reduction Processes on the Colour and Photochromism of Amorphous Mesoporous TiO_2 Thin Films Loaded with a Silver Salt. *Photochem. Photobiol. Sci* **2011**, *10* (11), 1810–1816.

(96) Vašková, H. A Powerful Tool for Material Identification : Raman Spectroscopy. *Int. J. Math. Model. Methods Appl. Sci.* **2011**, *5* (7), 1205–1212.

(97) Vinogradov, A. V.; Vinogradov, V. V. Low-Temperature Sol–Gel Synthesis of Crystalline Materials. *RSC Adv.* **2014**, *4* (86), 45903–45919.

(98) Nemanich, R. J.; Solin, S. A.; Martin, R. M. Light Scattering Study of Boron Nitride Microcrystals. *Phys. Rev. B* **1981**, *23* (12), 6348–6356.

(99) Shen, H.; Pollak, F. H. Raman Study of Polish-Induced Surface Strain in 100 GaAs and InP. *Appl. Phys. Lett.* **1984**, *45* (6), 692–694.

(100) Li Bassi, A.; Cattaneo, D.; Russo, V.; Bottani, C. E.; Barborini, E.; Mazza, T.; Piseri, P.; Milani, P.; Ernst, F. O.; Wegner, K.; et al. Raman Spectroscopy Characterization of Titania Nanoparticles Produced by Flame Pyrolysis: The Influence of Size and Stoichiometry. *J. Appl. Phys.* **2005**, *98* (7), 074305.

(101) Arora, A. K.; Rajalakshmi, M.; Ravindran, T. R. Phonon Confinement in Nanostructured Materials. *Encycl. Nanosci. Nanotechnol.* **2004**, *8*, 499–512.

(102) Zhang, W. F.; He, Y. L.; Zhang, M. S.; Yin, Z.; Chen, Q. Raman Scattering Study on Anatase TiO_2 Nanocrystals. *J. Phys. D. Appl. Phys.* **2000**, *33* (8), 912–916.

(103) Ohsaka, T. Temperature Dependence of the Raman Spectrum in Anatase TiO_2. *J. Phys. Soc. Japan* **1980**, *48* (5), 1661–1668.

(104) Gottstein, G. *Physical Foundations of Materials Science*, 1st ed.; Springer-Verlag Berlin Heidelberg GmbH, 2004.

(105) Gleiter, H. Nanostructured Materials: Basic Concepts and Microstructure. *Acta mater.* **2000**, *48*, 1–29.

(106) Bottein, T.; Dalstein, O.; Putero, M.; Cattoni, A.; Faustini, M.; Abbarchi, M.; Grosso, D. Environment-Controlled Sol-Gel Soft-NIL Processing for Optimized Titania, Alumina, Silica and Yttria-Zirconia Imprinting at Sub-Micron Dimensions. *Nanoscale* **2018**, *10* (3), 1420–1431.

(107) Bargougui, R.; Oueslati, A.; Schmerber, G.; Ulhaq-Bouillet, C.; Colis, S.; Hlel, F.; Ammar, S.; Dinia, A. Structural, Optical and Electrical Properties of Zn-Doped SnO_2 Nanoparticles Synthesized by the Co-Precipitation

Technique. *J. Mater. Sci. Mater. Electron.* **2014**, *25* (5), 2066–2071.

(108) Tauc, J., Grigorovici, R., & Vancu, A. Optical Properties and Electronic Structure of Amorphous Germanium. *Phys. Status Solidi* **1966**, *15* (2), 627–637.

(109) Srikant, V.; Clarke, D. R. On the Optical Band Gap of Zinc Oxide. *J. Appl. Phys.* **1998**, *83* (10), 5447–5451.

(110) Hassanien, A. S.; Akl, A. A. Effect of Se Addition on Optical and Electrical Properties of Chalcogenide CdSSe Thin Films. *Superlattices Microstruct.* **2016**, *89*, 153–169.

(111) Welte, A.; Waldauf, C.; Brabec, C.; Wellmann, P. J. Application of Optical Absorbance for the Investigation of Electronic and Structural Properties of Sol-Gel Processed TiO_2 Films. *Thin Solid Films* **2008**, *516* (20), 7256–7259.

(112) Mathews, N. R.; Morales, E. R.; Cortés-Jacome, M. A.; Toledo Antonio, J. A. TiO_2 Thin Films - Influence of Annealing Temperature on Structural, Optical and Photocatalytic Properties. *Sol. Energy* **2009**, *83* (9), 1499–1508.

(113) Taherniya, A.; Raoufi, D. The Annealing Temperature Dependence of Anatase TiO_2 Thin Films Prepared by the Electron-Beam Evaporation Method. *Semicond. Sci. Technol.* **2016**, *31* (12), 125012.

(114) Lin, C. P.; Chen, H.; Nakaruk, A.; Koshy, P.; Sorrell, C. C. Effect of Annealing Temperature on the Photocatalytic Activity of TiO_2 Thin Films. *Energy Procedia* **2013**, *34*, 627–636.

(115) Boissiere, C.; Grosso, D.; Lepoutre, S.; Nicole, L.; Bruneau, A.; Sanchez, C. Porosity and Mechanical Properties of Mesoporous Thin Films Assessed by Environmental Ellopsometric Porosimetry. *Langmuir* **2005**, *21* (26), 12362–12371.

(116) Palpant, P. *Non-Linear Opt. Prop. Matter*; Springer Netherlands, 2006.

(117) Rycenga, M.; Cobley, C. M.; Zeng, J.; Li, W.; Moran, C. H.; Zhang, Q.; Qin, D.; Xia, Y. Controlling the Synthesis and Assembly of Silver Nanostructures for Plasmonic Applications. *Chem. Rev.* **2011**, *111*, 3669–3712.

(118) Beliatis, M. J.; Henley, S. J.; Silva, S. R. P. Engineering the Plasmon Resonance of Large Area Bimetallic Nanoparticle Films by Laser Nanostructuring for Chemical Sensors. *Opt. Lett.* **2011**, *36* (8), 1362–1364.

(119) Park, C.; Yoon, J.; Thomas, E. L. Enabling Nanotechnology with Self Assembled Block Copolymer Patterns. *Polymer (Guildf).* **2003**, *44*, 6725–6760.

(120) Hyde, S. *The Language of Shape: The Role of Curvature in Condensed Mater: Physics, Chemsitry and Biology*; 1997.

(121) Fort, E.; Ricolleau, C.; Sau-Pueyo, J. Dichroic Thin Films of Silver Nanoparticle Chain Arrays on Facetted Alumina Templates. *Nano Lett.* **2003**, *3* (1), 65–67.

(122) Sanchez-Valencia, J. R.; Toudert, J.; Borras, A.; Barranco, A.; Lahoz, R.; de la Fuente, G. F.; Frutos, F.; Gonzalez-Elipe, A. R. Selective Dichroic Patterning by Nanosecond Laser Treatment of Ag Nanostripes. *Adv. Mater.* **2011**, *23* (7), 848–853.

(123) Nicolas Filippin, A.; Borras, A.; Rico, V. J.; Frutos, F.; González-Elipe, A. R. Laser Induced Enhancement of Dichroism in Supported Silver Nanoparticles Deposited by Evaporation at Glancing Angles. *Nanotechnology*

2013, *24* (4), 045301.

(124) Elechiguerra, J. L.; Larios-Lopez, L.; Liu, C.; Garcia-Gutierrez, D.; Camacho-Bragado, A.; Jose Yacaman, M. Corrosion at the Nanoscale: The Case of Silver Nanowires and Nanoparticles. *Chem. Mater.* **2005**, *17*, 6042–6052.

(125) Stalmashonak, A.; Matyssek, C.; Kiriyenko, O.; Hergert, W.; Graener, H.; Seifert, G. Preparing Large-Aspect-Ratio Prolate Metal Nanoparticles in Glass by Simultaneous Femtosecond Multicolor Irradiation. *Opt. Lett.* **2010**, *35* (10), 1671.

(126) Baraldi, G.; Gonzalo, J.; Solis, J.; Siegel, J. Reorganizing and Shaping of Embedded Near-Coalescence Silver Nanoparticles with off-Resonance Femtosecond Laser Pulses. *Nanotechnology* **2013**, *24*, 255301.

(127) Bonse, J.; Krüger, J.; Höhm, S.; Rosenfeld, A. Femtosecond Laser-Induced Periodic Surface Structures. *J. Laser Appl.* **2012**, *24* (4), 042006.

(128) Fuentes-Edfuf, Y.; Garcia-Lechuga, M.; Puerto, D.; Florian, C.; Garcia-Leis, A.; Sanchez-Cortes, S.; Solis, J.; Siegel, J. Coherent Scatter-Controlled Phase-Change Grating Structures in Silicon Using Femtosecond Laser Pulses. *Sci. Rep.* **2017**, *7* (1), 4594.

(129) Gnilitskyi, I.; Derrien, T. J.-Y.; Levy, Y.; Bulgakova, N. M.; Mocek, T.; Orazi, L. High-Speed Manufacturing of Highly Regular Femtosecond Laser-Induced Periodic Surface Structures: Physical Origin of Regularity. *Sci. Rep.* **2017**, *7* (1), 8485.

(130) Rudenko, A.; Colombier, J.-P.; Höhm, S.; Rosenfeld, A.; Krüger, J.; Bonse, J.; Itina, T. E. Spontaneous Periodic Ordering on the Surface and in the Bulk of Dielectrics Irradiated by Ultrafast Laser: A Shared Electromagnetic Origin. *Sci. Rep.* **2017**, *7* (1).

(131) Stalmashonak, A.; Seifert, G.; Graener, H. Optical Three-Dimensional Shape Analysis of Metallic Nanoparticles after Laser-Induced Deformation. *Opt. Lett.* **2007**, *32* (21), 3215–3217.

(132) Huang, M.; Cheng, Y.; Zhao, F.; Xu, Z. The Significant Role of Plasmonic Effects in Femtosecond Laser-Induced Grating Fabrication on the Nanoscale. *Ann. Phys.* **2013**, *525* (1–2), 74–86.

(133) Garrelie, F.; Colombier, J.-P.; Pigeon, F.; Tonchev, S.; Faure, N.; Bounhalli, M.; Reynaud, S.; Parriaux, O. Evidence of Surface Plasmon Resonance in Ultrafast Laser-Induced Ripples. *Opt. Express* **2011**, *19* (10), 9035.

(134) Siegman, A. E.; Fauchet, P. M. Stimulated Wood ’ s Anomalies on Laser-Illuminated. *IEEE J. Quantum Electron.* **1986**, *22* (8), 1384–1403.

(135) Vorobyev, A. Y.; Guo, C. Colorizing Metals with Femtosecond Laser Pulses. *Appl. Phys. Lett.* **2008**, *92* (041914), 1–4.

(136) Ocaña, M.; Garcia-Ramos, J. V.; Serna, C. J. Low-Temperature Nucleation of Rutile Observed by Raman Spectroscopy during Crystallization of TiO_2. *J. Am. Ceram. Soc.* **1992**, *75* (7), 2010–2012.

(137) Kholmanov, I. N.; Barborini, E.; Vinati, S.; Piseri, P.; Podesta, A.; Ducati, C.; Lenardi, C.; Milani, P. The Influence of the Precursor Clusters on the Structural and Morphological Evolution of Nanostructured TiO_2 under Thermal Annealing. *Nanotechnology* **2003**, *14*, 1168–1173.

(138) Doster, J.; Baraldi, G.; Gonzalo, J.; Solis, J.; Hernandez-Rueda, J.; Siegel, J. Tailoring the Surface Plasmon Resonance of Embedded Silver Nanoparticles by Combining Nano- and Femtosecond Laser Pulses. *Appl. Phys. Lett.* **2014**, *104* (15), 0–4.

(139) Stalmashonak, A.; Akin Unal, A.; Seifert, G.; Graener, H. Optimization of Dichroism in Laser-Induced Transformation of Silver Nanoparticles in Glass. In *SPIE*; 2008; Vol. 7033, pp 70331Z – 8.

(140) Walger, T.; Hersch, R. D. Hiding Information in Multiple Level-Line Moirés. In *ACM Symposium*; 2015; Vol. 24, pp 21–24.

(141) Amidror, I.; Chosson, S.; Hersch, R. D. Moiré Methods for the Protection of Documents and Products: A Short Survey. *J. Phys. Conf. Ser.* **2007**, *77* (1), 10.

(142) Chosson, S. M.; Hersch, R. D. Beating Shapes Relying on Moiré Level Lines. *ACM Trans. Graph* **2014**, *34* (1), 1–11.

(143) Pjanic, P.; Hersch, R. D. Color Imaging and Pattern Hiding on a Metallic Substrate. *ACM Trans. Graph.* **2015**, *34* (4), 130:1-130:10.

(144) Li, M.; Meuret, Y.; Geelen, R.; Jung, J.; Vervaeke, M.; Thienpont, H.; Duerr, F. Optical Modeling of Changeable Laser Image Functionality with Analysis of the Viewing Performance. *Appl. Opt.* **2015**, *54* (20), 6162–6171.

(145) Chen, W. T.; Yang, K. Y.; Wang, C. M.; Huang, Y. W.; Sun, G.; Chiang, I. Da; Liao, C. Y.; Hsu, W. L.; Lin, H. T.; Sun, S.; et al. High-Efficiency Broadband Meta-Hologram with Polarization-Controlled Dual Images. *Nano Lett.* **2014**, *14* (1), 225–230.

(146) Deng, Z. L.; Deng, J.; Zhuang, X.; Wang, S.; Li, K.; Wang, Y.; Chi, Y.; Ye, X.; Xu, J.; Wang, G. P.; et al. Diatomic Metasurface for Vectorial Holography. *Nano Lett.* **2018**, *18* (5), 2885–2892..

(147) Jin, L.; Dong, Z.; Mei, S.; Yu Feng, Y.; Wei, Z.; Pan, Z.; Daqiqeh Rezaei, S.; Li, X.; Kuznetsov, A. I.; Kivshar, Y. S.; et al. Noninterleaved Metasurface for (26 -1) Spin- and Wavelength-Encoded Holograms. *Nano Lett.* **2018**, *18* (12), 8016–8024.

(148) Heydari, E.; Sperling, J. R.; Neale, S. L.; Clark, A. W. Plasmonic Color Filters as Dual-State Nanopixels for High-Density Microimage Encoding. *Adv. Funct. Mater.* **2017**, *27* (35), 1–6.

(149) Goh, X. M.; Zheng, Y.; Tan, S. J.; Zhang, L.; Kumar, K.; Qiu, C. W.; Yang, J. K. W. Three-Dimensional Plasmonic Stereoscopic Prints in Full Colour. *Nat. Commun.* **2014**, *5*, 5361.

(150) Hu, D.; Lu, Y.; Cao, Y.; Zhang, Y.; Xu, Y.; Li, W.; Gao, F.; Cai, B.; Guan, B. O.; Qiu, C. W.; et al. Laser-Splashed Three-Dimensional Plasmonic Nanovolcanoes for Steganography in Angular Anisotropy. *ACS Nano* **2018**, *12* (9), 9233–9239.

(151) Guay, J.; Lesina, A. C.; Cote, G.; Charron, M.; Poitras, D.; Ramunno, L.; Berini, P.; Weck, A. Laser-Induced Plasmonic Colours on Metals. *Nat. Commun.* **2017**, *8*, 16095.

(152) Öktem, B.; Pavlov, I.; Ilday, S.; Kalaycioğlu, H.; Rybak, A.; Yavaş, S.; Erdoğan, M.; Ilday, F. Ö. Nonlinear Laser Lithography for Indefinitely Large-Area Nanostructuring with Femtosecond Pulses. *Nat. Photonics* **2013**, *7* (11), 897–901.

(153) Hernandez-Rueda, J.; Siegel, J.; Garcia-Lechuga, M.; Solis, J. Femtosecond Laser-Induced Refractive Index Changes at the Surface of Dielectrics: Quantification Based on Newton Ring Analysis. *J. Opt. Soc. Am. B* **2014**, *31* (7), 1676.

(154) Höhm, S.; Herzlieb, M.; Rosenfeld, A.; Krüger, J.; Bonse, J. Femtosecond Laser-Induced Periodic Surface Structures on Silicon upon Polarization Controlled Two-Color Double-Pulse Irradiation. *Opt. Express* **2015**, *23* (1), 61–71.

(155) Bonse, J.; Höhm, S.; Kirner, S. V.; Rosenfeld, A.; Krüger, J. Laser-Induced Periodic Surface Structures – a Scientific Evergreen. *IEEE J. Sel. Top. Quantum Electron.* **2017**, *23* (3), 9000615.

(156) Dusser, B.; Sagan, Z.; Soder, H.; Faure, N.; Colombier, J. P.; Jourlin, M.; Audouard, E. Controlled Nanostructrures Formation by Ultra Fast Laser Pulses for Color Marking. *Opt. Express* **2010**, *18* (3), 2913.

(157) Rebollar, E.; Vázquez de Aldana, J. R.; Martín-Fabiani, I.; Hernández, M.; Rueda, D. R.; Ezquerra, T. A.; Domingo, C.; Moreno, P.; Castillejo, M. Assessment of Femtosecond Laser Induced Periodic Surface Structures on Polymer Films. *Phys. Chem. Chem. Phys.* **2013**, *15*, 11287–11298.

(158) Heitz, J.; Reisinger, B.; Fahrner, M.; Romanin, C.; Siegel, J.; Svorcik, V. Laser-Induced Periodic Surface Structures (LIPSS) on Polymer Surfaces. In *International Conference on Transparent Optical Networks*; 2012; pp 1–4.

(159) Clavero, C. Plasmon-Induced Hot-Electron Generation at Nanoparticle/Metal-Oxide Interfaces for Photovoltaic and Photocatalytic Devices. *Nat. Photonics* **2014**, *8* (2), 95–103.

(160) Tian, Y.; Tatsuma, T. Mechanisms and Applications of Plasmon-Induced Charge Separation at TiO_2 Films Loaded with Gold Nanoparticles. *J. Am. Chem. Soc.* **2005**, *127* (20), 7632–7637.

(161) Furube, A.; Du, L.; Hara, K.; Katoh, R.; Tachiya, M. Ultrafast Plasmon-Induced Electron Transfer from Gold Nanodots into TiO_2 Nanoparticles. *J. Am. Chem. Soc.* **2007**, *129* (48), 14852–14853.

(162) Højlund-nielsen, E.; Clausen, J.; Mäkela, T.; Thamdrup, L. H.; Zalkovskij, M.; Nielsen, T.; Pira, N. L.; Ahopelto, J.; Mortensen, N. A.; Kristensen, A. Plasmonic Colors : Toward Mass Production of Metasurfaces. *Adv Mater Technol* **2016**.

(163) Wang, L.; Ng, R. J. H.; Safari Dinachali, S.; Jalali, M.; Yu, Y.; Yang, J. K. W. Large Area Plasmonic Color Palettes with Expanded Gamut Using Colloidal Self-Assembly. *ACS Photonics* **2016**, *3* (4), 627–633.

(164) Zhu, X.; Vannahme, C.; Højlund-nielsen, E.; Mortensen, N. A.; Kristensen, A. Plasmonic Colour Laser Printing. *Nat. Nanotechnol.* **2016**, *11* (December 2015), 325–330.

(165) Roberts, A. S.; Pors, A.; Albrektsen, O.; Bozhevolnyi, S. I. Subwavelength Plasmonic Color Printing Protected for Ambient Use. *Nano Lett.* **2014**, *14* (2), 783–787.

(166) Olson, J.; Manjavacas, A.; Liu, L.; Chang, W.-S.; Foerster, B.; King, N. S.; Knight, M. W.; Nordlander, P.; Halas, N. J.; Link, S. Vivid, Full-Color Aluminum Plasmonic Pixels. *Proc. Natl. Acad. Sci.* **2014**, *111* (40), 14348–14353.

(167) Clausen, J. S.; Højlund-Nielsen, E.; Christiansen, A. B.; Yazdi, S.; Grajower, M.; Taha, H.; Levy, U.; Kristensen, A.; Mortensen, N. A. Plasmonic Metasurfaces for Coloration of Plastic Consumer Products. *Nano Lett.* **2014**, *14* (8), 4499–4504.

(168) Yu, R.; Mazumder, P.; Borrelli, N. F.; Carrilero, A.; Ghosh, D. S.; Maniyara, R. A.; Baker, D.; García De Abajo, F. J.; Pruneri, V. Structural Coloring of Glass Using Dewetted Nanoparticles and Ultrathin Films of Metals. *ACS Photonics* **2016**, *3* (7), 1194–1201.

(169) Ooms, M. D.; Jeyaram, Y.; Sinton, D. Disposable Plasmonics: Rapid and Inexpensive Large Area Patterning of Plasmonic Structures with CO_2 Laser Annealing. *Langmuir* **2015**, *31*, 5252–5258.

(170) Zhu, X.; Vannahme, C.; Højlund-nielsen, E.; Mortensen, N. A.; Kristensen, A. Plasmonic Colour Laser Printing. **2016**, *11* (December 2015), 325–330.

(171) Li, Z.; Clark, A. W.; Cooper, J. M. Dual Color Plasmonic Pixels Create a Polarization Controlled Nano Color Palette. *ACS Nano* **2015**.

(172) Zijlstra, P.; Chon, J. W. M.; Gu, M. Five-Dimensional Optical Recording Mediated by Surface Plasmons in Gold Nanorods. *Nature* **2009**, *459* (7245), 410–413.

(173) Garcia, J. M. Color Characterization of a New Laser Printing System, Université Jean Monnet, 2016.

(174) Walker, J. Colour Rendering of Spectra https://www.fourmilab.ch/documents/specrend/.

(175) Radtke, G.; Botton, G. A. Scanning Transmission Electron Microscopy (STEM). In *Springer Tracts in Modern Physics*; Springer, New York, NY, 2011; pp 205–254.

(176) Cheynet, M.; Pokrant, S.; Irsen, S.; Krüger, P. New Fine Structures Resolved at the ELNES Ti-$L_{2,3}$ Edge Spectra of Anatase and Rutile: Comparison between Experiment and Calculation. *Ultramicroscopy* **2010**, *110* (8), 1046–1053.

(177) Gloter, A.; Ewels, C.; Umek, P.; Arcon, D.; Colliex, C. Electronic Structure of Titania-Based Nanotubes Investigated by EELS Spectroscopy. *Phys. Rev. B* **2009**, *80*, 035413 (1-6).

PUBLICATIONS

In Refereed Journals based on Thesis work

I. **Sharma, N**.; Destouches, N.; Florian, C.; Serna, R.; Siegel, J. Tailoring Metal-Dielectric Nanocomposite Materials with Ultrashort Laser Pulses for Dichroic Color Control. *Nanoscale* **2019**,11, 18779-18789

II. **Sharma, N**.; Vangheluwe, M.; Vocanson, F.; Cazier, A.; Bugnet, M.; Reynaud, S.; Vermeulin, A.; Destouches, N. Laser-Driven Plasmonic Gratings for Hiding Multiple Images. *Mater. Horizons* **2019**, *6* (5), 978–983

III. **Sharma, N**.; Ma, H.; Bottein, T.; Bugnet, M.; Vocanson, F.; Grosso, D.; Itina, T. E.; Ouerdane, Y.; Destouches, N. Crystal Growth in Mesoporous TiO_2 Optical Thin Films. *J. Phys. Chem. C* **2019**, *123* (10), 6070–6079

Other Publications

I. Andreeva, Y.; **Sharma, N**.; Rudenko, A.; Mikhailova, J.; Sergeev, M.; Veiko, V. P.; Vocanson, F.; Lefkir, Y.; Destouches, N.; Itina, T. E. Insights into Ultrashort Laser-Driven Au:TiO_2 Nanocomposite Formation. *J. Phys. Chem. C* **2020**, *124* (18), 10209–10219

International/National Conferences

I. N. Dalloz, C. Hubert, **N. Sharma**, M. Hébert, F. Vocanson, S. Ayala, N. Destouches, "Tailoring the appearance of Ag:TiO_2 nanocomposite films : application to image multiplexing", Workshop du GDR APPAMAT, 21 Oct 2019, Paris

II. **N. Sharma**, M. Vangheluwe, A. Vermeulin, N. Destouches, “Laser induced nanostructuring of plasmonic composite films for color image multiplexing”, NANOP Functional Nanophotonics, 4-6 Sept, 2019, Munich (invited)

III. **N. Sharma**, M. Vangheluwe, M. Bugnet, A. Vermeulin, N. Destouches, “Laser induced nanostructuring of plasmonic composite films for color image multiplexing”, META, 23-26 July, 2019, Lisbon, France (invited)

IV. Y. Andreeva, **N. Sharma**, N. Destouches, F. Vocanson, T. Itina, "Laser induced growth and degradation of gold nanoparticles in titanium dioxide porous film. Fundamentals of Laser Assisted Micro and Nano-Technologies", FLAMN-2019, 30 Jun-4 July 2019, Saint-Petersburg, Russia

V. **N. Sharma**, M. Vangheluwe, A. Vermeulin, N. Destouches, “Multidimensionality of plasmonic colors. Application to image multiplexing”, NANOTECH FRANCE, 26-28 Jun, 2019, Paris (invited)

VI. **N. Sharma**, M. Vangheluwe, A. Vermeulin, N. Destouches, “Laser controlled plasmonic nanocomposite films for color image multiplexing”, EMRS 2019, 27-31 May, 2019, Nice, France (invited)

VII. H. Ma, S. Bakhti, Z. Liu, **N. Sharma**, Y. Andreeva, A. Rudenko, F. Vocanson, D. S. Slaughter, N. Destouches, T.Itina, "On the mechanisms of metal nanoparticle formation in CW laser-irradiated thin porous films" EMRS Spring meeting, Nice, 27-31 May 2019 (oral)

VIII. Y. Andreeva, M. Sergeev, H. Ma, **N. Sharma**, N. Destouches, T. Itina, V. Veiko, "Experimental and numerical study of laser-induced metal nanoparticle formation in thin porous films", MNNSI, 8-12 November, 2018, Suzdal, Russia (oral)

IX. **N. Sharma**, M. Vangheluwe, F. Vocanson, Y. Lefkir, A. Vermeulin, N. Destouches, "Laser-induced fabrication of encoded diffractive images on plastic substrates with plasmonic films", MNO 2018, 5-7 November 2018, Villeurbanne, France (oral)

X. N. Destouches, Z. Liu, S. Bakhti, **N. Sharma**, H. Ma, J. Siegel, T. Itina, F. Vocanson, D. Slaughter, "Growth and self-organization of metallic nanoparticles by laser: mechanisms and applications", MNO 2018, 5-7 November 2018, Villeurbanne, France (oral)

XI. **N. Sharma**, H. Ma, F. Vocanson, M. Vangheluwe, M. Bugnet, C. Hubert, S. Reynaud, A. Vermeulin, T. E. Itina, N. Destouches. A low-temperature synthesis of crystallized TiO_2 mesoporous thin films and application to laser-induced printing, AEM, UK-Surrey, 2018

XII. N. Destouches, **N. Sharma**, O. Sidorov, N. Dalloz, C. Hubert, F. Vocanson, M. Hébert, J. Siegel, M. Vangheluwe, A. Vermeulin, "Image multiplexing with laser-controlled plasmonic colors", **META** 2018, June 24- July 1, 2018, Round-trip Marseille Cruise (invited)

XIII. **N. Sharma**, H. Ma, Z. Liu, F. Vocanson, Y. Lefkir, N. Dalloz, M. Hébert, T. E. Itina, N. Destouches. Self-organization of gold and silver nanoparticles inside TiO_2 thin films: Understanding the temperature rise and growth mechanism upon laser irradiation, GOLD 2018, France-Paris

XIV. N. Destouches, Z. Liu, **N. Sharma**, Y. Lefkir, F. Vocanson, M. Hébert, J. Solis, J. Siegel "Self-Organized Growth of Metallic Nanoparticles upon cw and fs Laser Writing: Mechanisms and Application", **HPLA**, March 26-29, 2018, Santa Fe, USA (invited)

XV. **N. Sharma**, Z. Liu, M. Vangheluwe, F. Vocanson, Y. Lefkir, G. Vitrant, N. Detouches. Understanding the self-organization mechanism of metallic nanoparticles inside TiO_2 thin film by femtosecond (fs) and continues-wave (cw) laser exposure, Fraunhofer Summer School, Germany-Dresden, 2017